# MIXED-LINKER ZIF MATERIALS AND ZIF/POLYMER HOLLOW FIBER MEMBRANES FOR HYDROCARBON SEPARATIONS

A Thesis
Presented to
The Academic Faculty

by

Kiwon Eum

In Partial Fulfillment
of the Requirements for the Degree
Doctor of Philosophy in Chemical Engineering
in the School of Chemical & Biomolecular Engineering

Georgia Institute of Technology
August 2016

# MIXED-LINKER ZIF MATERIALS AND ZIF/POLYMER HOLLOW FIBER MEMBRANES FOR HYDROCARBON SEPARATIONS

Approved by:


Dr. Sankar Nair, Advisor
School of Chemical & Biomolecular Engineering
*Georgia Institute of Technology*

Dr. Christopher W. Jones, Co-Advisor
School of Chemical & Biomolecular Engineering
*Georgia Institute of Technology*

Dr. Ryan P. Lively
School of Chemical & Biomolecular Engineering
*Georgia Institute of Technology*

Dr. Peter J. Hesketh
School of Mechanical Engineering
*Georgia Institute of Technology*

Dr. Krista S. Walton
School of Chemical & Biomolecular Engineering
*Georgia Institute of Technology*


Date Approved: July 18th , 2016

*To my lovely family: Mom, Dad, Wife and my sister,*
*Yeonsuk, Seungsub, Hyelin and Jungwon*

# ACKNOWLEDGEMENTS

I would like to send my sincerest appreciation to my advisors Dr. Sankar Nair, and Dr. Christopher W. Jones for their all guidance and support throughout my Ph.D studies. Their enthusiasm and insightful knowledge kept me motivated to keep striving towards completion of the degree. Also their guidance at each point of my PhD works made this accomplishment possible. I will never be able to express my deepest appreciation to them for what I have learned in the past four years.

I would also like to thank my committee members, Dr. Peter J. Hesketh, Dr. Ryan P. Lively, and Dr. Krista S. Walton, for their valuable time and contributions to my studies. It was my pleasure to have these great professors in my thesis committee.

I owe my sincere appreciate to the faculty members at the Department of Chemical & Biomolecular Engineering, Georgia Tech. I would like to thank Fereshteh Rashidi and Chen Ma for providing data for this dissertation. I also thank to my Georgia Tech Korean Friends for their encouragements and support.

I want to express my deepest gratitude to my parents, Seungsub Eum, and YeunSook Lee, for their endless Love and support to my academic endeavors. They showed me the passion for education and always encouraged me throughout my scholarly pursuit. I owe a special thanks to my younger sister (Jungwon Eum), parents in-law (Insook Hyun and Doochul Kim) and brother (Junyeob Kim) for their constant support, and pray.

Last, but not least, I am grateful to my loving wife Hyelin Kim for providing emotional support and encouragement throughout my academic endeavors. Without her, I would not have completed my degree. I truly Love you.

# TABLE OF CONTENTS

Page

# LIST OF TABLES

# LIST OF FIGURES

# SUMMARY

Metal-organic frameworks (MOFs) are a promising class of nanoporous materials consisting of organic linkers coordinated to metal clusters in crystalline structures. A subclass of MOFs, known as zeolitic imidazolate frameworks (ZIFs), form structural topologies equivalent to zeolites, and have many advantageous properties including good thermal and chemical stability, high microporosity, and high surface area.[1,2] They are attractive for use in hydrocarbon gas separations that currently rely upon energy-intensive processes.[1,3-5] In particular, membranes made from ZIFs may be useful for hydrocarbon gas separations.[6,7] However, scalable and high-performance membranes for hydrocarbon separations are currently not available. In this work, I aim to demonstrate a 'mixed-linker' strategy to develop ZIF materials for $C_3$ or $C_4$ hydrocarbon separations[8], and furthermore to develop a scalable and low-cost ZIF membrane fabrication methodology that can enable the use of ZIF materials in large-scale membrane separation processes.

Chapter 1 presents an overview of the state of the art in ZIF synthesis, ZIF membrane fabrication, and understanding of transport in ZIF membranes. The key scientific and technological issues of relevance to this work are introduced. In Chapter 2, we discuss the mixed-linker approach to synthesize ZIF with tunable properties, with particular focus on the synthesis of ZIF 8-90 mixed-linker crystals. we then demonstrate that ZIF-8-90 mixed-linker materials allow tuning of adsorption and diffusion properties of certain hydrocarbons. Volumetric uptake methods are used to study intracrystalline adsorption and diffusion phenomena of different gases in mixed-linker ZIF materials, facilitated by the ability to control the crystal size of the ZIFs. Particle size distributions are measured

using dynamic light scattering or optical microscopy, and crystal composition analysis was performed using $^1$H-NMR spectroscopy and micro-Raman spectroscopy. Specifically, it is shown that: (1) the hydrocarbon adsorption properties of ZIF 8-90 mixed-linker ZIFs change significantly with composition, and (2) the diffusion properties and selectivities show very large changes with mixed-linker composition. This first demonstration clearly shows the potential of this approach for use in a variety of molecular separations.

In Chapter 3, we turn to the development of scalable fabrication methodologies for ZIF membranes. We discuss a technique called Interfacial Microfluidic Membrane Processing (IMMP) that overcomes many limitations of current membrane fabrication processes.[9] We investigate the use of IMMP to fabricate high-performance ZIF-8 membranes on polymeric hollow fibers, and consider specific aspects of the membrane fabrication process in more detail. We investigate the roles of controlled solvent exchange, control of capillary stresses, temperature profiles, and the hollow fiber support morphology, on the morphology and permeation properties of the resulting membranes. We then use this mechanistic understanding to engineer a higher-performance ZIF-8 membrane in Torlon® hollow fibers. Detailed characterization of the membrane and support fiber morphology is presented. Permporometry analysis confirms the lack of microscale defects in the optimized ZIF-8 membranes. Detailed binary and ternary mixture permeation measurements reveal that the optimized ZIF-8 membranes have excellent separation factors (e.g., $C_3H_6/C_3H_8 > 50$, $H_2/C_3H_8 > 2000$) and permeances (e.g., $C_3H_6 >$ 50 GPU) in the temperature range of 30-120°C.

In Chapter 4, we discuss the fabrication and characterization of ZIF-8 hollow fiber membranes of unprecedented high quality by further rational optimization of the IMMP

technique, and obtain $C_3H_6/C_3H_8$ separation factors of over 180 at room temperature. Detailed binary mixture ($C_3H_6/C_3H_8$) permeation measurements reveals that the membrane maintains a $C_3H_6/C_3H_8$ separation factor over 85 at 120 °C. We also demonstrate for the first time, the high-pressure operability of these membranes for separating $C_3H_6/C_3H_8$ feed mixtures with no evidence of significant defects up to 9.5 bar feed pressure. The ZIF-8 membranes show $C_3H_6/C_3H_8$ separation factors of 90 at 9.5 bar, and obtain 4.5 times higher throughput compared to atmospheric pressure differentials. Finally, we confirm the long term stability of the ZIF-8 hollow fiber membranes by continuously operating the membrane for a month without losing permeances or selectivity. This work clearly shows the potential of MOF materials and the IMMP method as a platform for developing membrane systems to address a variety of molecular separations.

In Chapter 5, we extend the application of IMMP to fabricate ZIF membranes other than ZIF-8, with a view to develop a more general membrane fabrication platform for a wider variety of molecular separations. Here, for the first time, we fabricate ZIF-8 and ZIF-90 membranes on the inner surface of macroporous carbon hollow fibers *via* IMMP. Due to the higher chemical stability of carbon materials (relative to polymers) in organic solvents, this approach allows the use of different organic solvents required for fabrication of other ZIF/MOF membranes. It also opens the possibility of using ZIF membranes in liquid-phase separations. Our approach can be applied more generally to other MOF materials, but we demonstrate our key findings here with the examples of ZIF-8 and ZIF-90 membrane synthesis. We also report detailed single gas separation measurements, as well as n-$C_4H_{10}$/*i*-$C_4H_{10}$ mixed gas permeation performance.

# CHAPTER 1.

# INTRODUCTION

## 1.1. Membrane Separations

Industrial separation processes heavily rely on energy-intensive technology. Separation technologies crosscut all manufacturing industries and account for 22% of all in-plant industrial energy use (approximately 4,500 TBtu/yr) in the United States.[10,11] Compared to the high energy consumption resulting from thermodynamically driven separation methods (such as distillation, crystallization, absorption, and adsorption), transport-driven processes based upon membranes can substantially reduce the energy and capital costs of separating molecules.

### 1.1.1. Polymeric Membranes

Among the different classes of membrane materials —such as polymers, zeolite molecular sieves, and metal organic frameworks—each class has its own strengths and weaknesses. The gas separation membrane market currently favors polymeric membranes owing to their low cost and high processability.[12] These membranes can be manufactured in different morphologies, such as asymmetric hollow fiber membranes (ca. 50–3000 μm in diameter).[13] The dense selective layer offers both the possibility of being integral with the fiber and the possibility of being a separate layer coated onto the porous support fiber.[14] However, polymeric membranes have significant limitations. These include low thermal and chemical stabilities, such as swelling and plastization, and more fundamentally, an intrinsic trade-off between permeability and selectivity (Figure 1.).[15]

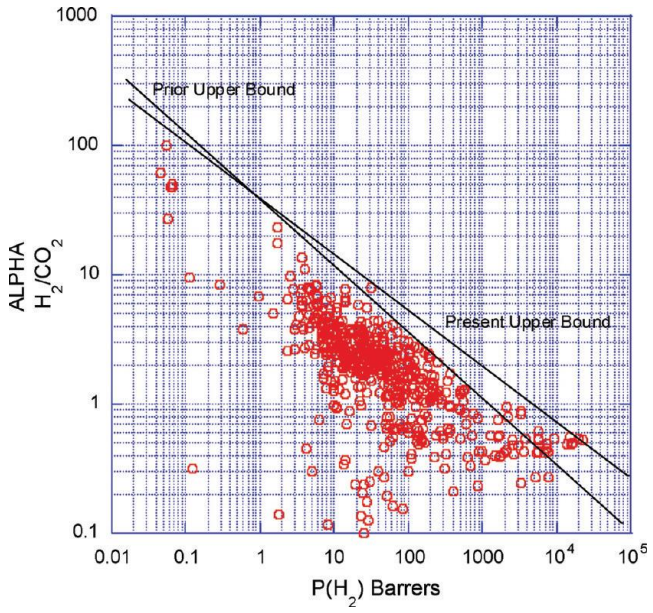


**Figure 1.** Upper bound of polymer membrane performance for $H_2/CO_2$ separation.[15]

### 1.1.2. Metal-Organic Framework (MOF) Membranes

MOFs are a relatively novel class of nanoporous materials, comprised of organic linkers coordinated to metal ions in crystalline structures.[16](Figure 2) MOFs can tune their pore sizes, shapes, and the affinity of the pores towards different gases simply by changing the combination of organic linkers and metal complexes. MOFs also have high porosities, permanent pores, low densities (0.2–1 g/cm3), record surface areas (>10000 $m^2/g$), and reasonable thermal and mechanical stabilities.[6] These advantages allow MOFs as a good candidate for membrane materials by exploiting differences in molecular adsorption, diffusivity, or both. The vast range of MOF structures and the relative simplicity of their synthesis (in relation to other nanoporous materials like zeolites) create the possibility of rational design, synthesis, and modification of MOF structures for specific separations.[17] MOFs also shows unique structure properties such as flexibility and gate opening enabling the possibility of simultaneous high permeability and attractive selectivity.[18]

Furthermore, the synthesis conditions are more benign than those for other nanoporous materials such as zeolites. For example, the synthesis of most MOF materials does not require high-temperature pressure conditions; they can be synthesized using self-assembly. Further, organic structure-directing agents ('templates') are not necessary unlike the case of zeolites. This eliminates the need of a subsequent high- temperature calcination step.

A subclass of MOFs, known as zeolitic imidazolate frameworks (ZIFs), form structural topologies equivalent to zeolites (Figure 3.).[2] ZIFs have many advantageous properties including good thermal and chemical stability, high microporosity, and high surface area.[1] A considerable body of work has appeared on ZIF membranes, particularly ZIF-8, and their promising performance for hydrogen/propane and propylene/propane separations.[2,19,20]

However, it is well accepted that single-linker ZIF materials can only allow 'step' changes in pore size by variation of the imidazolate linker. Since diffusion-based molecular separations are extremely sensitive to small (< 0.1 Å) changes in the effective pore size, thus, only a small range of separations are reasonably possible with the available set of single-linker ZIFs. For example, ZIF-8 is only useful for separating hydrogen from hydrocarbons and propylene from propane.[21] Recently, mixed linker MOFs approaches were investigated to "continuously tune the pore size[22] according to the size of components to be separated. It cannot be achieved by other materials such as zeolite that has "discrete" pore size range indicating only limited separations are possible.

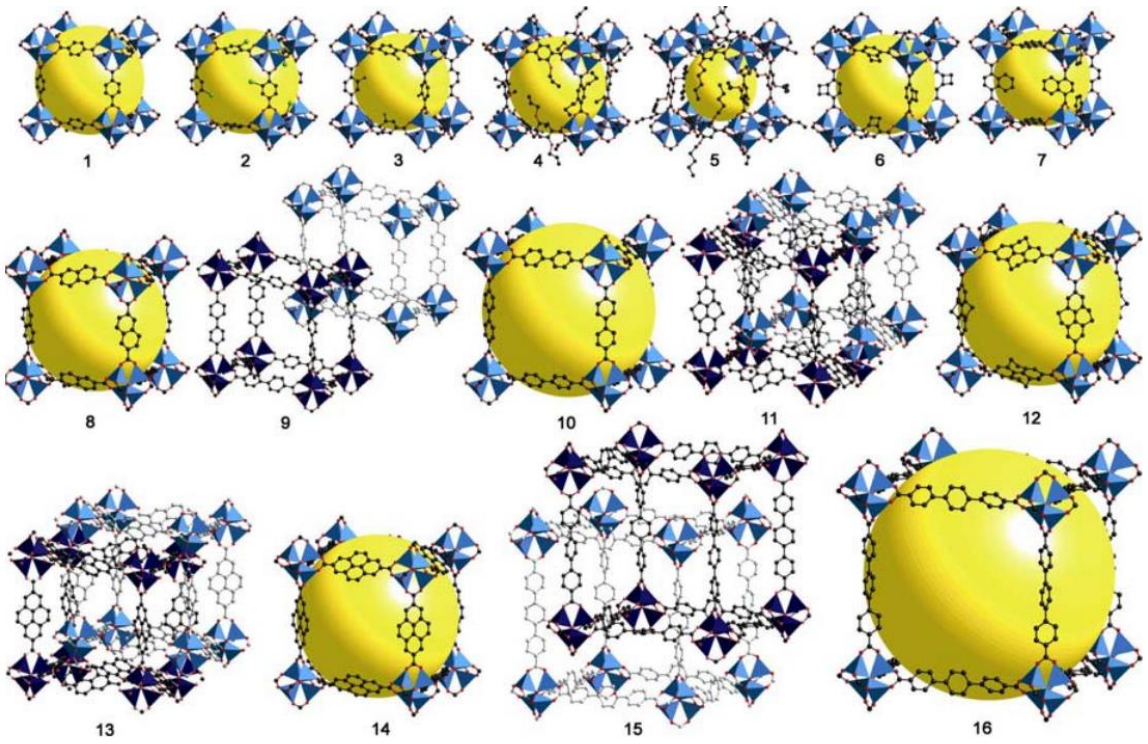


**Figure 2.** A large series of isoreticular metal–organic frameworks (IRMOFs) has been produced in which each member shares the same cubic topology. Each compound is synthesized by employing the corresponding organic link in the solvothermal conditions established for formation of the octahedral secondary building unit (SBU). The links differ both in functionality of the pendant groups (IRMOF-1 to -7) and in length (IRMOF-8 to -16). While expansion of the links increases the internal voidspace (representedby yellow spheres), it also allows the formation of catenatedphases (IRMOF-9, -11, -13 and-15) [23]

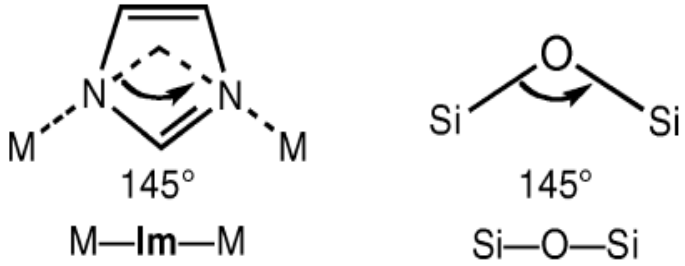


**Figure 3.** M-Im-M and Si-O-Si bond angle of 145°[24]

### 1.1.3. Current Challenges in MOF Membranes

Most MOF membrane fabrication techniques face issues of processability and defects[5]. As an alternative to polycrystalline MOF membranes, 'mixed-matrix' membranes (MMMs) can combine some of the benefits of polymeric and nanoporous materials. Specifically, MMMs can combine the attractive molecular sieving and adsorption properties of MOFs with the good processing properties of polymers, by mixing (nano)particles of MOFs with a traditional polymer followed by casting into a composite/hybrid membrane[25]. However, the MMM performance is ultimately limited by the polymer properties, and can offer only incremental increases in performance over polymeric membranes. Another key issue impeding the realization of industrially attractive MOF membranes is the lack of a scalable and inexpensive membrane fabrication process.[9] Most MOF membranes are fabricated on expensive ceramic supports such as alumina, zirconia and titania using techniques that are difficult to scale-up. Finally, the chemical stability of MOF materials used for membrane fabrication is still uncertain in many cases.[9]

## 1.2. MOF Membrane Fabrication Techniques

### 1.2.1. Single Phase Methods

An overview of fabrication approaches for pure MOF and mixed-matrix MOF membranes can be found in Figure 4. Most of the early MOF membrane fabrication techniques include solvothermal synthesis, in whichboth metal and organic precursor solutions are dissolved together with the substrate immersed in the growth solution directly. Here, we can classify the fabrication method into two categories; *in-situ* growth

and seeded or secondary growth. For *in-situ* growth, the substrate is directly immersed in the growth solution and contains no previously attached crystalline framework materials. One of the difficulties inherent in *in-situ* solvothermal synthesis is the lack of nucleation sites on the surface of support to promote favorable heterogeneous MOF layer growth (adhesion), usually resulting in a poorly intergrown film. Significant work has been reported to enhance the adhesion between the substrate and MOF layer. Most of the early works focused on chemical modification of the support to achieve the strong interfacial bonding between substrate and MOF. Caro et al provided a 3-aminopropyltriethoxysilane (APTES) modification approach on disc-type alumina supportd to create covalent bonds between nucleated ZIF crystals and the support. The APTES binder has amino groups that can react with the aldehyde group via an imine condensation reaction. APTES can also coordinate with the free $Zn^{2+}$ cluster thereby boosting favorable heterogeneous nucleation and growth on the support surface. It has been more generally uses for fabrication of ZIF membranes (ZIF-90, ZIF-22, ZIF-7, ZIF-8, and ZIF-95) on porous ceramic supports.[9,26] Other works have demonstrated the use of polymeric coatings on ceramic substrates to improve MOF membrane adhesion. Polydopamine (PDA) - modified alumina supports have been used to prepare ZIF-100 membranes.[27] Another similar approach was reported by using poly(methylmethacrylate) (PMMA) as a binder between silicon wafer substrate and a HKUST-1 MOF layer. PMMA was converted into poly(methacrylic acid) (PMAA) which provides the active localized nucleation sites (carboxylic groups). [28] More recently, the same group reported a 2D laminated ZIF-8-ZnAl-$NO_3$ layered double hydroxide (LDH) composite membrane starting from ZnAl-$NO_3$ LDH layer. Here ZnAl-$NO_3$ served as a $Zn^{2+}$ source for ZIF-8, thereby improving the

defect density of the membrane and achieving dramatic enhancement of $H_2/CH_4$ selectivity. Jeong et al reported well-intergrown ZIF-8 membranes in the presence of sodium formate. The sodium formate plays a critical role by reacting with $Zn^{2+}$ to form a ZnO layer on the support.[29] The ZnO layer acts as a secondary metal source boosting heterogeneous nucleation of ZIF-8 on the surface. Sodium formate can also enhance the quality of the MOF layer by deprotonating a ligand precursor and promoting a nucleation rate. Fischer et al developed atomic layer deposition (ALD) methods to form a ZnO layer on Si support surfaces as a secondary metal source for high rates of heterogeneous nucleation during growth of polycrystalline films.[30] Polymeric tubes and hollow fibers have also been recently considered as potential supports for *in situ* MOF membrane growth. For example, Mao et al. reported a 'pressure assisted' HKUST-1 membrane fabrication technique on polyvinylidene fluoride (PVDF) hollow fibers.[31] Here, nanoparticles called 'copper hydroxide nanostands' (CHNs) were used as a metal source, and were deposited on the outer surface of the hollow fiber by pulling a vacuum on the bore side. This was followed by *in-situ* solvothermal membrane growth from a $H_3BTC$ linker solution. Li et al. also reported a HKUST-1 membrane on a chemically modified polyacrylonitrile (PAN) hollow fiber. They reported a two-step modification of the fibers before use in membrane fabrication. The stiffness and compression strength of the polymer support was significantly improved by the chemical modification (dehydrogenation, cyclization and crosslinking reactions) to reduce the flexibility of the support. Then, deprotonated carboxylic acid groups were provided on the fiber surface to complex $Cu^{2+}$ ions and improve the adhesion between the MOF layer and substrate.[32]

On the other hand, seeded growth methods involve deposition of seed nanocrystals of the MOF on the substrate, followed by the growth of the seed layed into a polycrystalline intergrown film. It is hypothesized that seeded growth can obtain much better control of the MOF membrane characteristics (layer thickness, orientation, defects) by decoupling the nucleation and growth steps.[33] Various kinds of seeding techniques have been investigated. Early work in our group (Brown et al)[34] reported the fabrication of continuous ZIF-90 membranes on unmodified poly(amideimide) (PAI) hollow fiber supports., using ~200 nm seed crystals of ZIF-90. In addition to the formation of a seed layer to aid membrane formation, the carbonyl groups on the surface of the ZIF-90 particles were expected to interact with amide and imide groups of the fiber support and further improve film adhesion. Yuan et al. reported a ZIF-7 membrane that was seeded using thin ZIF-7 nanosheets.[35] They report the preparation of '1 nm ultra-thin' ZIFs nano sheets with large lateral area, which was hypothesized to allow better coverage of the support as well as the formation of an membrane layer after hot drop coating method. The Wang group reported the formation of 100 nm thin ZIF-8/graphene oxide (GO) membranes using hybrid ZIF-8 sheets/GO nanosheets as a seed layer.[36] The ZIF-8/GO hybrid nanosheets can not only provide a uniform seed layer but also act as a diffusion barrier between two precursor solutions to allow thinner ZIF membranes in a counter-diffusion growth process. The Jeong group has demonstrated a ZIF-67 membrane showing the possibility of heteroepitaxial growth. Here, ZIF-8 crystals were used to provide densely packed seed layers, followed by solvothermal ZIF-67 membrane growth. The resulting membrane showed excellent propylene/propane separation performance.[37] Physical or chemical modification of the support has also been investigated for defect-

free ZIF membranes. For example, the Lin group reported a ZIF-78 membrane using a reactive seeding method on porous ZnO support.[38] Here, the membrane support itself can be used as the metal precursor to generate the seed layer, leading to a strongly attached and uniform seed layer. The Wang group reported a precursor infiltration method on porous supports for ZIF-8 membrane synthesis.[39] The MeIM precursor was melted with a heater and infiltrated into the alumina support of pore size 0.1 μm. The pre-treated alumina support was then immersed into the $Zn^{2+}$ precursor solution to form an infiltrated ZIF-8 seed layer. A dense and mechanically stable 12 μm ZIF-8 layer was obtained after secondary growth from this seed layer.

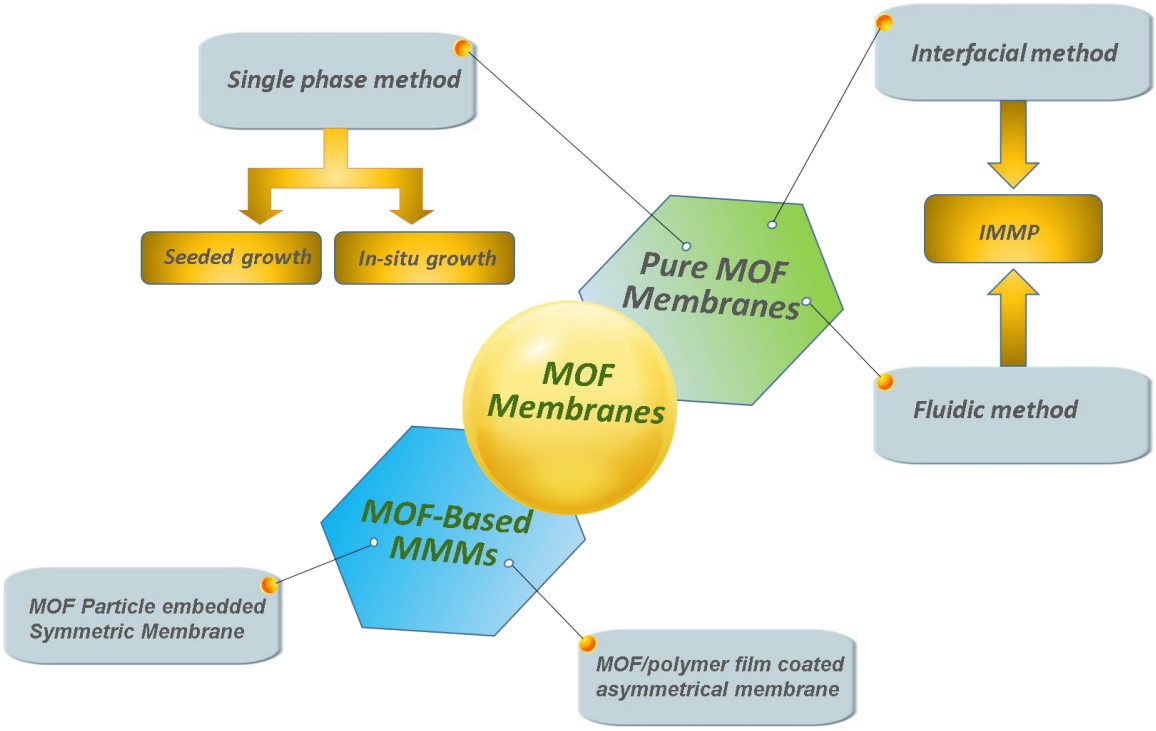


**Figure 4.** Overview of fabrication approaches for pure MOF and mixed-matrix MOF membranes.

### 1.2.2. Fluidic Methods

Despite the extensive work reported as described above, both *in-situ* and seeded growth methods still show important limitations such as defect control, number of steps in the process, use of expensive support materials, need for pre-treatment/modification steps, and overall scalability of the fabrication process. To overcome these challenges, our group developed fluidic methods to fabricate MOF membranes in/on hollow fiber supports. In this method, the precursor solutions are introduced into the bore and/or shell side of the fibers with a certain temporal flow profile (e.g, continuous, intermittent, static) and in either counter-diffusion (opposing reactants) or co-diffusion geometries. Brown et al was the first to demonstrate this approach to fabricate ZIF-8 membranes inside PAI hollow fibers by a counter-diffusion technique referred to as Interfacial Microfluidic Membrane Processing (IMMP).[9] The resulting membranes showed high permeance and good selectivity for hydrogen/propane and propylene/propane separation. Following this initial report, several groups have presented variations of this technique. Coronas et al grew continuous and thin layers of ZIF-7 and ZIF-8 on the inner surfaces of polysulfone and copolymer hollow fibers by means of microfluidic synthesis.[40,41] One pure solvent and two precursor solutions were simultaneously introduced in the bore side of polysulfone hollow fiber. The resultant ZIF/PSF membranes showed selectivity in $H_2/CO_2$ and $CO_2/CH_4$ gas separations, although their permeances were quite low. However, this work focused on co-current synthesis (simultaneous introduction of all reactants on the bore side). Huang and Lin reported a modified counter-diffusion method to form ZIF-71 membranes on ceramic hollow fibers.[42] Metal and organic precursor solutions were separated by the ceramic hollow fiber support, which was connected to

reservoirs to provide diffusion-driven supply of reactants for film growth. The resulting ZIF-71 hollow fiber membrane presented high performance for ethanol/water mixture separation.

In the IMMP-type methods, the metal ion and organic ligand are dissolved in two immiscible solvents respectively or the two precursor solutions are separated by the porous substrate. The two species can counter-diffuse through the porous channel of the substrates and meet each other at the interface. The MOF film nucleation and crystallization can take place only at the liquid-liquid interface, as shown in the case of free-standing MOF films.[43] This method has high potential for fabrication of more defect-free membranes because it has an intrinsic defect-limiting nature, *i.e.*, once the initial membrane is formed, further contact of the two precursors can only occur through the defects resulting in progressive "filling in" of such defects. Moreover, IMMP allows better control of a number of variables such as the solvent/reactant combinations on each of side of the fiber, the temporal flow profiles on each side, and other conditions such as concentration and temperature. While similar techniques have been used to form ZIF-8 and HKUST-1 membranes on conventional flat and tubular supports[44,45], the use of hollow fiber supports (< 300 μm ID) creates a number of new challenges in terms of reactant supply and control over film formation in the microscopic environment of the fiber bore. Finally, successful MOF membrane defect control strategies mentioned above are summarized in Figure 5. Here we categorize the defect control strategies into four groups (single phase method, fluidic method, interfacial, and MMM method) and brief illustration of each works was presented.

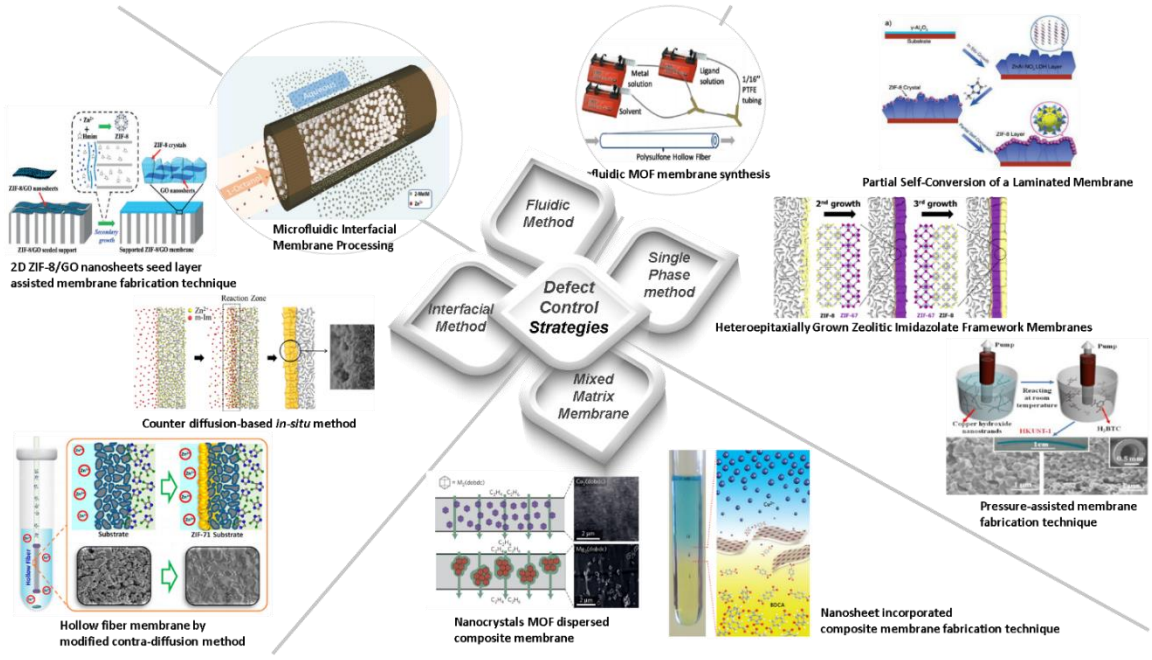


**Figure 5.** Successful defect control strategies for MOF membranes.[9,31,36,37,40,42,44,46-49]

### 1.2.3. Mixed Matrix Membranes

While pure MOF membranes offer the best possibilities for large enhancements in separation performance over existing polymeric membranes, their scalable fabrication has proved challenging. Therefore, an alternative approach based upon mixed-matrix membranes (MMMs) has also been pursued. MMMs are based upon the premise that one can combine (to a certain extent) the benefits of high processibility of polymers with the high performance of nanoporous MOF materials.[50,51] The MOF crystals are mixed with the polymer solution and then cast or spun into a hybrid membrane in which the MOF crystals are embedded in the polymer film and boost its performance. However, MMMs have a number of serious difficulties. Scalability is an issue, since it has not proved possible to obtain the required high loadings (>50 vol%) of MOFs in the polymer membrane during hollow fiber spinning.[50,51] Defect control is another issue when

fabricating MMMs in tubular or fiber configuration, in particular the presence of void spaces between the nanoporous particles and polymer matrix due to poor adhesion between the two phases.[7] Finally, MMM transport models indicate that the performance enhancements would be incremental at best, since the performance is ultimately constrained by the properties of the polymer matrix surrounding the dispersed MOF particles.[52] Ongoing work is attempting to address these limitations, e.g. the use of nano sized MOFs for better compatibility with polymers and reduction of plasticization at higher operating pressures[53-55], the introduction of high-aspect-ratio sheet-like (2D) MOFs to improve performance at lower MOF loadings[49], and *in situ* MOF particle growth in the polymer solution before membrane formation.[56] However, due to the intrinsic limits on MMM performance, we do not consider MMMs as a viable solution for separation of larger or more complex molecules which have low permeabilities in polymers.

### 1.3. Permeation Properties and Applications of MOF Membranes

Olefin/paraffin separation by distillation is considered to be the single largest energy consumer and $CO_2$ emitter in the chemical industry. There is a strong need for an alternative separation technology. For example, Kwon et al. showed the upper bound of $C_3H_6/C_3H_8$ for polymer membranes indicating that they are not industrially attractive (Figure 6). Carbon membranes show high performance in some cases, but are prepared by high-temperature pyrolysis processes and are challenging to scale up in an economical manner. On the other hand, some of the reported ZIF-8 membranes show promising permeation properties for $C_3H_6/C_3H_8$ separation (Table 1). However, it is also seen from

Table 1 that fabrication of ZIF-8 membranes on scalable platforms such as polymeric hollow fibers are challenging and has been fully developed only by our group.

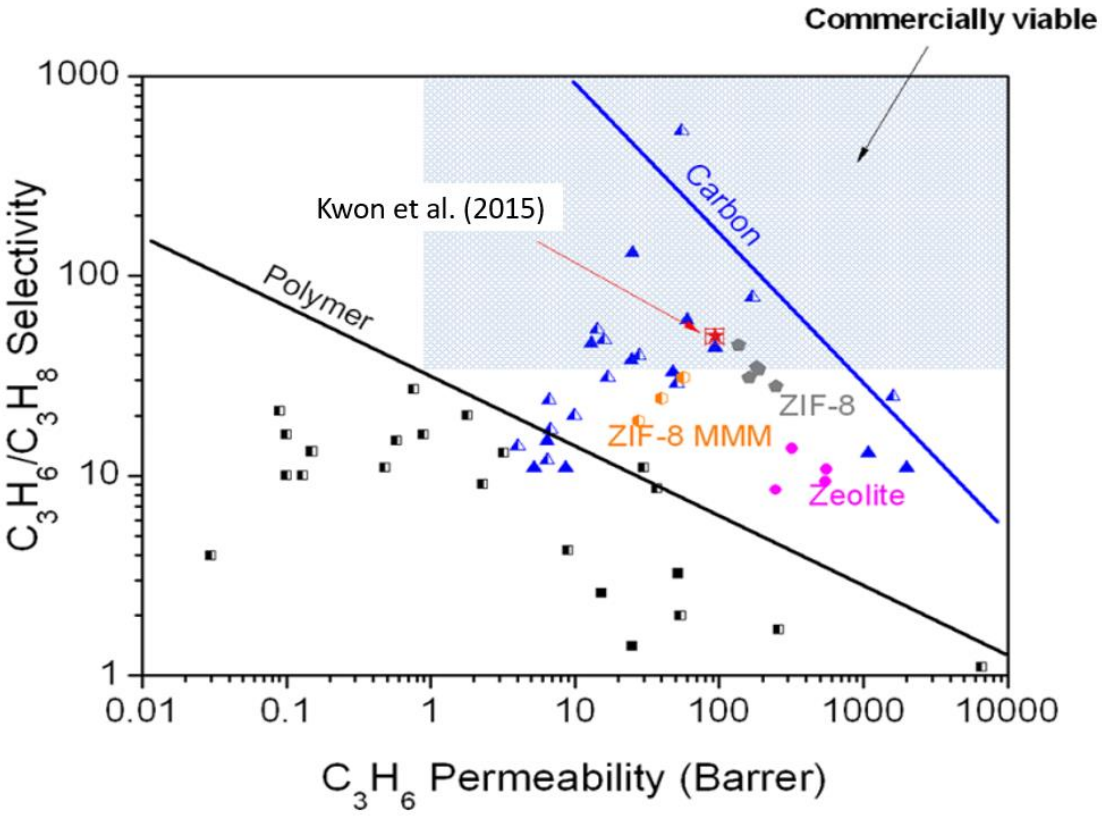


**Figure 6.** Comparison of the propylene/propane separation performance of our ZIF-8 membranes with those of other membranes reported in the literatures. Half- and full-filled symbols indicate separation data from single and binary gas permeation measurements, respectively. The shaded area in the graph implies the performance requirement of a membrane (a minimum permeability of 1 Barrer and selectivity of 35) for commercial application. The solid lines are the so called Robison upper bound. Triangle: Carbon membrane;[57-59] circle: zeolite membrane;[60] rectangle: polymer membrane;[61] pentagon: ZIF-8 membrane;[21] hexagon: ZIF-8 mixed matrix membrane;[53] star: ZIF-8 membrane in this work (Kwon et al.).[44]

**Table 1.** Representative summary of ZIF-8 membrane performance for $C_3H_6/C_3H_8$ separation.

| Ref | Support | Fabrication method | Temp [°C] | $C_3H_6$ permeance [GPU] | $C_3H_6/C_3H_8$ selectivity | Thickness [µm] |
|---|---|---|---|---|---|---|
| Pan (2012)[21] | Alumina Disk | hydrothermal seeded growth | 30 °C | 83 ± 3 | 35 ± 10 | 2.2 |
| Kwon (2012)[62] | Alumina Disk | Microwave assisted seeded growth | 30 °C | 62 ± 2 | 40 ± 9 | 1.5 |
| Liu (2014)[63] | Alumina Disk | hydrothermal seeded growth | 30-120 °C | 33 | 30 | 2.5 |
| Hara (2014)[64] | Alumina Tube | Counter diffusion *in-situ* growth | 50 °C | 7 | 59 | 80 |
| Brown (2014)[9] | PAI Hollow Fiber | IMMP *in-situ* growth | 30 °C | 36 ± 3 | 12 ± 3 | 8.8 |
| Pan (2015)[65] | Alumina Disk | hydrothermal seeded growth | 30 °C | 23 | 89 | 0.5-1.6 |
| Kwon (2015)[66] | Alumina Disk | Counter diffusion seeded growth | 120 °C | 80 ± 4 | 71 ± 11 | 1 |
| Yu (2016)[67] | Alumina Disk | hydrothermal seeded growth | 120 °C | 19 ± 3 | 50 ± 2 | 2.5 |
| Eum (2016)[68] | PAI Hollow Fiber | IMMP *in-situ* growth | 20-40 °C (non-isothermal) | 48 ± 3 | 180 ± 5 | 8 |

### 1.4. ZIF Membrane Transport Mechanisms

In this section we give a brief account of transport modeling approaches used for various purposes in this thesis. This description allows a better understanding of the adsorption, diffusion, and membrane permeation results discussed in later chapters of this work.

### 1.4.1. Gas Transport in Porous Membranes

Gas transport in nanoporous membranes entails both thermodynamic (sorption/desorption) and kinetic (diffusion) processes.[69] Generally speaking, the gas partial pressure difference across the membrane is the driving force, while the thickness of the membrane layer provides resistance. Permeability ($P$) is the measure of the ease that a gas species permeates through a membrane, and incorporates both adsorption and diffusion terms. It may be obtained experimentally from the pressure differential and thickness normalized gas flux (Eq. 1). The ideal selectivity ($\alpha_{A/B}$) of a membrane denotes the ratio of the permeability of the respective gases (Eq. 3). Thus, the membrane's selectivity—calculated by combining Eq. (1) and (2) to generate Eq. (3) —refers to the membrane's capability of providing a selective barrier to B relative to A. Permeability and selectivity are material properties of a membrane, and ideally, these are independent of process conditions such as feed pressure and flow rate. Still, both permeability and selectivity are temperature dependent.

$$\mathcal{P}_A = \frac{[\text{Flux}_{(A)} \text{ through membrane}]\,[\text{thickness}]}{[\Delta p_A]} \tag{1}$$

$$\alpha_{A/B} = \frac{\mathcal{P}_A}{\mathcal{P}_B} \tag{2}$$

$$\alpha_{A/B} = \frac{[\text{Flux}_{(A)} \text{ through membrane}][\Delta p_B]}{[\text{Flux}_{(B)} \text{ through membrane}][\Delta p_A]} \tag{3}$$

The ZIF membranes investigated in this work have an asymmetric structure, with a thin ZIF layer supported by a much thicker, highly porous Torlon® support. The resistance of the support is much lower (by at least two orders of magnitude) than the resistance within the ZIF membrane[70]. The porous Torlon® substructure merely provides mechanical support so that the membrane can hold high pressures. In addition to the permeability,

asymmetric membranes are also characterized by their permeance ($P/l$), with $l$ referring to the molecular sieving membrane layer thickness (Eq. 4). An asymmetric membrane's selectivity does *not* depend on the membrane layer thickness, but is the ratio of the permeances of the two different gases (Eq. 5).

$$(\frac{\mathcal{P}}{\ell})_A = \frac{[\text{Flux}_{(A)} \text{ through membrane}]}{[\Delta p_A]} \quad (4)$$

$$\alpha_{A/B} = \frac{(\frac{\mathcal{P}}{\ell})_A}{(\frac{\mathcal{P}}{\ell})_B} = \frac{\mathcal{P}_A}{\mathcal{P}_B} \quad (5)$$

### 1.4.2. Maxwell-Stefan Formulation

I can further explore the transport mechanism in ZIF membranes using equilibrium adsorption data at multiple temperatures. The Maxwell-Stefan (M-S) formulation is the most convenient and general macroscopic model of describing diffusion within microporous materials, as described below:[71]

$$N_i = -\rho q_{sat} D_{M-S,i} \Gamma_i \nabla \theta \quad (6)$$

Where N is molar flux, ρ is the ZIF density, $D_{M\text{-}S,i}$ is M-S diffusivity, $\Gamma_i$ is the thermodynamic correction factor, and $q_{sat}$ is saturation loading .

Skoulidas and Sholl have found that the M-S diffusivity of small guest molecules such as He or Ar in MFI is practically independent of loading.[72] This scenario, called *weakly confined* molecules means molecules can pass each other (either directly in the same pore or via detours into other pores) irrespective of loading. The M-S equation can be used to

calculate the flux through the membrane, as described below:[71]

$$N_i = \frac{\rho q_{sat} D_{M-s,i}}{L} \ln \frac{1+bp_0}{1+bp_L} = \frac{\rho q_{sat} D^0_{M-s,i} e^{-E_a/RT}}{L} \ln \frac{1+(b^0 e^{\Delta S/R}) p_0 e^{-\Delta H/RT}}{1+(b^0 e^{\Delta S/R}) p_L e^{-\Delta H/RT}} \quad (7)$$

Here, $D^0_{M\text{-}S,i}$, $b^0$ are M-S diffusivity and affinity constant in the chosen standard state. $p_0$ and $p_L$ represents the feed side and the permeate side pressure and L represents the membrane thickness. ΔH is Heat of adsorption.

In the second case of *strongly confined molecules* in the host framework, I can obtain the flux from following equation:

$$N_i = \frac{\rho q_{sat} D^0_{M-s,i} e^{-E_a/RT}}{L} \frac{(p_0 - p_L)(b^0 e^{\Delta S/R}) e^{-\Delta H/RT}}{(1+(b^0 e^{\Delta S/R}) p_0 e^{-\Delta H/RT})(1+(b^0 e^{\Delta S/R}) p_L e^{-\Delta H/RT})} \quad (8)$$

Permeability of the material is normalized by the pressure gradient and the length, the flux is related to permeability, $P_i$ by:[73]

$$N_i = P_i \frac{(p_0 - p_L)}{L} \quad (9)$$

Introducing Eq. (8) into Eq. (9) yields:[71,73]

$$P_i = \frac{(\rho q_{sat} D^0_{M-s,i} e^{-E_a/RT})(b^0 e^{\Delta S/R}) e^{-\Delta H/RT}}{(1+(b^0 e^{\Delta S/R}) p_0 e^{-\Delta H/RT})(1+(b^0 e^{\Delta S/R}) p_L e^{-\Delta H/RT})} \quad (10)$$

This equation represents the permeability of a single component gas through ZIF-8-90 membrane described by the Langmuir isotherm for its adsorption properties and ideal permselectivities of my target gases can be obtained by take the ratio of two permeability value.[73]

$$\alpha_{i/j} = \frac{P_i}{P_j} \tag{11}$$

The fundamental diffusion and adsorption parameters required in the above equations can be obtained experimentally as summarized below.

### 1.4.3. Transport Diffusivities from Uptake Data

Transport diffusivities can be estimated experimentally by fitting the initial linear gravimetric or volumetric uptake rate with an approximate analytical solution for uptake in spherical particles at constant gas pressure:[74]

$$\frac{M_t}{M_\infty} = \frac{6}{R}\sqrt{\frac{D}{\pi}} \cdot \sqrt{t} \tag{12}$$

$M_t$ and $M_\infty$ are moles adsorbed by sample at time t and time goes to infinity (mmol), respectively. $R$ is equivalent average radius of the spherical sample (cm) and $D$ is transport diffusivity ($cm^2/s$). However, accurate diffusivities may not be obtained using the average crystal size.[75] Also, the uptake process always involves changes in gas pressure with uptake time, which means that Eqn (1) is not strictly valid. Thus, a more detailed model taking into account the crystal size distribution (CSD) and the non-constant pressure boundary condition was used to calculate transport diffusivity:[74]

$$\frac{M_t}{M_\infty} \approx \sum_i X_i (1+\alpha)\left[1-\frac{\gamma_1}{\gamma_1+\gamma_2}eerfc\left\{\frac{3\gamma_1}{\alpha}\left(\frac{Dt}{R_i^2}\right)^{1/2}\right\}-\frac{\gamma_2}{\gamma_1+\gamma_2}eerfc\left\{\frac{3\gamma_2}{\alpha}\left(\frac{Dt}{R_i^2}\right)^{1/2}\right\}\right] \quad (13)$$

$$\alpha = \frac{1}{\Lambda} - 1 \quad (14)$$

$$\gamma_1 = \frac{1}{2}\left\{\left(1+\frac{4}{3}\alpha\right)^{1/2}+1\right\} \quad (15)$$

$$\gamma_2 = \gamma_1 - 1 \quad (16)$$

$$eerfc(z) = \exp(z^2) \times erfc(z) \quad (17)$$

Here $\Lambda$ is the fraction of adsorbate finally adsorbed by the crystal, and $X_i$ is the mass fraction of the crystals with a radius of $R_i$.

### 1.4.4. Fitting of Adsorption Isotherms

The adsorption isotherms of small hydrocarbons in ZIFs (measured by gravimetric or volumetric methods) are well described by the Langmuir model, with parameters listed in Eq (18):

$$C(p) = \frac{C_s bp}{1+bp} \quad (18)$$

Here, $p$ is the equilibrium pressure of sample chamber (bar), $C$ is the adsorbate concentration in the sample (mmol/g), $C_s$ is the Langmuir capacity constant (mmol/g) and $b$ is the Langmuir affinity constant (1/bar).

### 1.4.5. Maxwell-Stefan Diffusivities from Transport Diffusivities

The corrected Maxwell-Stefan diffusivity was calculated as follows:[76]

$$D = D_0 \frac{d \ln p}{d \ln C(p)} \qquad (19)$$

Here, $D$ is the transport diffusivity ($cm^2/s$) and $D_0$ is the corrected M-S diffusivity ($cm^2/s$). The correction factor on the right hand side of Eq. (8) is the derivate of the isotherm and was calculated from the adsorption isotherm data in logarithmic coordinates.

### 1.4.6. Modeling of Defects

The M-S model described in previous sections assumes the existence of a perfect (defect-free) ZIF membrane. However, in reality, the total permeation molar flow rate $N_i$ ($mol.s^{-1}$) of any component $i$ of molecular weight $M_i$ through the membrane is the result of three parallel transport pathways (Figure 7): ZIF ($z$), membrane defects and grain boundaries ($d$), and the 'lumen bypass' ($b$). The lumen bypass can be considerably reduced by sealing the ends of the fiber with an elastomeric material like polydimethylsiloxane (PDMS). The flow rates are then normalized by the applied pressure differential, which is the same for all three pathways, thus yielding the permeance of the real membrane. We assume that:

*Before PDMS sealing of the sides of the fiber*, flow through the $d$ and $b$ pathways is governed by Knudsen selectivity. Thus, the flow rates for different gases in these two paths will be proportional to the inverse square root of their molecular weights. Hence, the flow rate for any component $i$ in these two pathways is expressed in terms of the flow rate of a reference component (here, propylene, $C_3$=).

*After PDMS sealing of the sides of the fiber*, flow through the $d$ pathway is still governed by Knudsen selectivity (since the lumen sealing is not intended to infiltrate the membrane

defects) but the *b* path now follows selectivity behavior expected in PDMS.

For any component *i*, we therefore have the following equations:

*Before PDMS sealing:*

$$\left(\frac{N_i}{\Delta P}\right)_{total} = \left(\frac{N_i}{\Delta P}\right)_z + \left(\frac{N_{C_3=}}{\Delta P}\right)_d \cdot \sqrt{\frac{M_{C_3=}}{M_i}} + \left(\frac{N_{C_3=}}{\Delta P}\right)_b \cdot \sqrt{\frac{M_{C_3=}}{M_i}} \qquad (20)$$

*After PDMS sealing of the lumen:*

$$\left(\frac{N_i}{\Delta P}\right)_{total} = \left(\frac{N_i}{\Delta P}\right)_z .\theta + \left(\frac{N_{C_3=}}{\Delta P}\right)_d \cdot \sqrt{\frac{M_{C_3=}}{M_i}} .\theta + \left(\frac{N_{C_3=}}{\Delta P}\right)_{b-PDMS} . \alpha_{i,C3=}^{PDMS} \qquad (21)$$

The factor $\theta$ (used for the *z* and *d* pathways) represents the fraction of membrane area still available for permeation after axial penetration of the PDMS sealant. The factor $\alpha$ represents the selectivity of PDMS for component *i* over propylene.

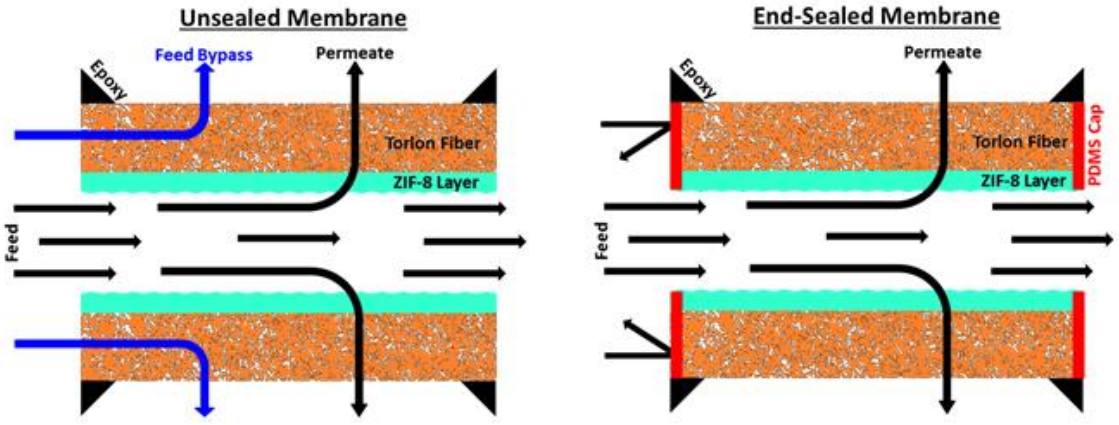


**Figure 7.** Schematic (left) showing feed gas molecules bypassing the ZIF-8 membrane through the fiber ends, and (right) suppression of the bypass effect by capping the fiber ends with a PDMS film (red).[9]

## 1.5. Impact of This Work

There are three main advances discussed in this work. Firstly, we show that the mixed linker ZIF synthesis approach allow us to access highly tunable adsorption and diffusion properties, thereby opening up the wider applicability of mixed-linker ZIF materials as a platform for a variety of membrane-based and adsorption -based molecular separations. Especially, continuous pore size tunability of mixed linker ZIFs broadens the spectrum of possible gas separations of interest that cannot be achieved by porous materials that have only "discrete" pore sizes such as single-linker ZIFs or zeolites. Secondly, this work considerably advances the interfacial microfluidic membrane processing (IMMP) methodology for scalable ZIF membrane fabrication, that combines three key concepts: (1) *in-situ* (2) two-solvent interfacial and (3) controlled supply, replenishment, and recycling of microfluidic conditions in the hollow fiber bore. In particular, we have obtained considerable mechanistic insights into the IMMP process, and showed how these insights can be used to greatly improve the membrane performance by engineering the IMMP conditions and the properties of the hollow fiber support. Thirdly, we also extend the IMMP technique for fabrication of other ZIF membranes and other types of separations, by the use of carbon fibers as inert, swelling-resistant support materials. By successfully fabricating ZIF-8 and ZIF-90 membranes in carbon fibers supports, we have shown the versatility of the IMMP technique for processing under a wide range of solvents and reaction conditions. This development also allows a notable step toward in realizing stable liquid-phase separations with ZIF membranes. Overall, this work brings closer to reality the use of advanced membrane separations that would lead to large capital, energy, and $CO_2$ emission reductions in the chemical sector.

# CHAPTER 2.

# SYNTHESIS AND CHARACTERIZATION OF ZIF-8-90 MIXED LINKER MATERIALS[1]

## 2.1. Introduction

Metal organic frameworks (MOFs) are nanoporous materials consisting of organic linkers coordinated to metal clusters in crystalline structures. They are potentially attractive as energy-efficient gas separation materials and membranes.[1] MOFs can be used for separations by exploiting differences in molecular adsorption strength, diffusivity, or both.[20] The vast range of MOF structures and the relative simplicity of their synthesis (in relation to other nanoporous materials like zeolites) create the possibility of rational design, synthesis, and modification of MOF structures[77,78] for specific adsorptive[79-81] or diffusion-based[44,53,63,82] separations. A subclass of MOFs, known as zeolitic imidazolate frameworks (ZIFs), consist of metal (mainly tetrahedral $Zn^{2+}$) bridged by the nitrogen atoms of imidazolate linkers. ZIFs form structural topologies equivalent to those found in zeolites and other inorganic nanoporous oxide materials. More than 100 ZIF structures have been synthesized, including crystal topologies not realized in zeolites.[83-87] Several ZIFs are known to have good thermal and chemical stability, high microporosity, and high internal surface area.[88] ZIFs have created substantial interest for potential use in diffusive and adsorptive separations. For example, ZIF-8 is useful for membrane-based separation of hydrogen from hydrocarbons and propylene from propane to potentially

[1] Reprinted with permission from K. Eum, K. C. Jayachandrababu, F. Rashidi, K. Zhang, J. Leisen, S. Graham, R. P. Lively, R. R. Chance, D. S. Sholl, C. W. Jones, S. Nair, "Highly Tunable Molecular Sieving and Adsorption Properties of Mixed-Linker Zeolitic Imidazolate Frameworks", Journal of the American Chemical Society, 137, p. 4191-4197. Copyright 2015 Americal Chemical Society

replace or debottleneck energy-intensive cryogenic distillation processes.[6,9,21]

A considerable body of work has appeared on the quantification of molecular diffusion properties of ZIFs (most notably ZIF-8) and their use in membranes for diffusion-dominated separations.[1,89-91] It has been shown that molecules with significantly higher kinetic diameters than the nominal pore limiting diameter of ZIF-8 (3.4 Å) can diffuse through its micropores.[91] Molecular modeling and experimental measurements have shown that ZIF-8 has high diffusion selectivity for methanol over ethanol, whereas ZIF-90 has moderate selectivity for the same molecules.[92] Recent work has demonstrated the high hydrophobicity of ZIF-8 *via* adsorption studies of water and a number of liquid organic adsorbates.[93] ZIF-8 has also been identified as a candidate for adsorptive recovery of ethanol, propanol and butanol from water due to its hydrophobicity.[94,95]

However, it is now clear that single-linker ZIF materials can only allow 'discrete' changes in pore size and adsorption characteristics by variation of the imidazolate linker. Diffusion-based molecular separations are extremely sensitive to small (< 0.1 Å) changes in the effective pore size. Only limited diffusive separations are possible with single-linker ZIFs, and *de novo* design and synthesis of ZIFs for each new separation target is difficult. Similarly, adsorptive separations are sensitive to small changes in the hydrophilicity or organophilicity of the ZIF which are difficult to design *de novo*. In previous work, I demonstrated a synthetic approach for a series of mixed-linker ZIF-8-90 and ZIF-7-8 materials by inclusion of 2-carboxyimidazole (ZIF-90 linker) and benzimidazole (ZIF-7 linker) along with 2-methylimidazole (ZIF-8 linker) during synthesis.[88,96] Preliminary characterization revealed these materials had a continuously tunable effective pore size (as measured by nitrogen physisorption) that is between the

pore sizes of the single-linker 'parent' materials (ZIF-7, ZIF-8, and ZIF-90). I denote the mixed-linker ZIF-8-90 materials as ZIF-$8_x$-$90_{100-x}$ ($0 \leq x \leq 100$), where $x$ is the percentage of ZIF-8 linkers in the framework. Here I demonstrate extensively that ZIF-8-90 materials have the remarkable property of continuously tunable diffusion and adsorption properties of hydrocarbons, alcohols, and water over several orders of magnitude. This result is facilitated by the controlled synthesis and characterization of a set of ZIF 8-90 mixed linker crystals spanning the entire range of 2-MeIM/OHC-IM linker ratios, and with a large and controllable range of crystal sizes (from less than 0.5 μm to about 100 μm). I use micro-Raman spectroscopy, as well as water adsorption isotherms, to conclusively prove the mixed-linker composition of the individual crystals. Comprehensive diffusion and adsorption measurements using PFG-NMR, gravimetric, and volumetric techniques allow a detailed demonstration and evaluation of the tunable separation properties of mixed-linker ZIFs.

## 2.2. Experimental Methods

### 2.2.1. Materials

2-Methylimidazole (99%, 2-MeIM), $Zn(NO_3)_2 \cdot 6H_2O$ (99%) and sodium formate (99%, $NaCO_2H$) were obtained from Sigma-Aldrich. Carboxyaldehyde-2-imidazole (99%, OHC-IM), dimethylformamide (DMF), and methanol (MeOH) were obtained from Alfa Aesar. Deionized water (DI-$H_2O$) was produced with a Thermo Scientific 7128.

### 2.2.2. Synthesis of ZIF-8, ZIF-90, and ZIF-8-90

Different synthesis procedures were used to produce ZIF crystals of different size ranges

suitable for hydrocarbon diffusion measurements. Each of these synthesis procedures is described in detail below.

**(*1*)** ZIF-8-90 mixed-linker crystals of ~100 μm size were synthesized by modifying the procedure reported by Cravillon *et al*.[97] A solution of 0.544 g (8 mmol) ofNaCOOH, *x* mmol of 2-MeIm (ZIF-8 linker), and (8-*x*) mmol of OHC-Im (ZIF-90 linker) was dissolved in 40 ml of MeOH. The value *x* was 0-8. A mixture consisting of 0.595 g (2 mmol) of $Zn(NO_3)_2{\cdot}6H_2O$ dissolved in 40 ml MeOH was poured into 2-MeIM/OHC-IM solution. The resulting solution was heated at 90°C for 24 hr in a sealed glass jar. The large crystals formed on the walls were collected and washed several times with DI- $H_2O$ and MeOH, and then dried in an oven at 80°C.

**(*2*)** ZIF 8-90 crystals in the 10 μm range were synthesized as reported by Thompson *et al*.[88] A solution of *x* mmol of 2-MeIM, (20-*x*) mmol of OHC-IM and 20mmol of $NaCO_2H$ in 50 ml of MeOH was prepared. The value *x* was 0- 20. The solution was stirred and heated at 50 °C until it became clear, and then cooled to room temperature. A solution of 5 mmol of $Zn(NO_3){\cdot}6H_20$ in 50 ml of DI- $H_2O$ was prepared, poured into the first solution, and the resulting mixture was allowed to stir at room temperature for 1 hr. ZIF crystals were collected by centrifugation at 7500 rpm for 7 min, washed in MeOH three times, and dried in an oven at 80 °C.

**(*3*)** ZIF-8 crystals of 338 nm average size were synthesized as reported by Lai *et al*.[82] 22.7 g (276.5 mmol) of 2-MeIM (ZIF-8 linker) was added to 70mL DI-water and stirred with a magnetic bar until the solution became clear at room temperature. A mixture consisting of 1.17 g (3.7 mmol) of $Zn(NO_3)_2{\cdot}6H_2O$ dissolved in 18 mL DI- $H_2O$ was poured into the 2-MeIM/DI-water solution and stirred at room temperature for 12 hr. The

resulting milky solution was centrifuged at 9000 rpm for 15 min followed by washing with MeOH and DI- $H_2O$ three times to collect the ZIF crystals, which were then dried in an oven at 80°C.

**(*4*)** ZIF-90 crystals of 55.7 μm average size were synthesized by modifying the procedure of Gee *et al*.[92] 3.84 g (40 mmol) of OHC-IM and 2.97 g (10 mmol) of $Zn(NO_3)_2 \cdot 6H_2O$ were added to 100mL DMF. The solution was heated to 120 °C while stirring for 10 min in a glass jar. The light-orange colored solution was poured into a wide-necked bottle and capped for 24 hr at room temperature. The large crystals on the walls were collected, washed extensively with DI-$H_2O$ and MeOH, and dried in an oven at 80 °C.

### 2.2.3. Characterization

XRD patterns were measured on a PANalytical X'Pert Pro diffractometer at room temperature using Cu Kα radiation of λ = 0.154 nm and 5-40° 2θ. Crystal size distribution (CSD) analyses were conducted with a Protein Solutions DynaPro DLS instrument, a Hitachi SU 8010 SEM, and a Nikon Eclipse 50i optical microscope. The CSD of 338 nm ZIF-8 was obtained by DLS. The ZIF-8 powder was dispersed by sonication in a filtered MeOH solution for 5 min. The colloidal suspension was inserted into a cuvette via a 5 μm syringe filter for DLS measurements. CSDs of 1-10 μm ZIF-8-90 materials were measured from multiple SEM images to obtain sample sizes of more than 200 crystals in each case. CSD of ZIF crystals greater than 30 μm in size were obtained by optical microscopy. The samples were dispersed on a slide glass and the CSD was measured from about 200 crystals in each case. Since large ZIF crystals are highly faceted, the equivalent spherical crystal radius was taken to be that of the smallest circle

that encompasses the entire crystal. Solution $^{1}$H-NMR measurements were performed with a Bruker 400 MHZ spectrometer after digesting the ZIF crystals in d4-acetic acid ($CD_3CO_2D$). To determine the fraction of each imidazole linker in the ZIF materials, the integrated peak area of the methyl protons of 2-MeIM (chemical shift 2.65 pm) was normalized to that of the aldehyde proton of OHC-Im (9.84 pm). The chemical shifts of both imidazole linkers was referenced to the chemical shift (2.30 pm) of d4-acetic acid. Powder FT-Raman spectroscopy was performed with a Bruker Vertex 80v FTIR/RAM II FT-Raman Analyzer in open atmosphere and a He/Ne red laser (1054 nm). Raman microscopy of individual ZIF crystals was carried out using a Horiba *Jobin*-Yvon HR-800 dispersive spectrometer with an 1800 l/mm grating and a green laser (532nm). A spot size of 2.5 μm was used. Numerical integration of FT-Raman and micro-Raman peak areas was carried out with the instrument software. The 2-MeIM and OHC-IM peaks were background-subtracted using a polynomial, and then fitted with mixed Gaussian–Lorentzian functions to obtain the integrated peak areas.

### 2.2.4. Adsorption and Diffusion Measurements

The *n*-butane and *i*-butane transport diffusivities and adsorption isotherms were measured with a volumetric (pressure decay) apparatus.[98] A known amount of ZIF sample was sealed into a 0.5 μm filter element and installed in the sample chamber. The volumes of the sample chamber and reservoir chamber are precisely known. It was determined that all my experiments satisfied the criterion for isothermal macroscopic diffusion.[99] The apparatus was placed in a silicone oil bath equipped with a circulator for temperature control. The sample was degassed under vacuum at 150°C for 12 h and then maintained

for 12 h at 35°C. The vacuum was then isolated, and a known quantity of hydrocarbon gas was injected into the reservoir chamber. The valve connecting the sample and reservoir chambers was then opened. Sensitive pressure transducers attached to the sample and reservoir chambers were used to measure the pressure changes over time, occurring due to adsorption. The data were converted to uptake curves using a virial equation of state.

## 2.3 Results and Discussion

### 2.3.1. Crystal Size Distributions

To successfully measure intracrystalline diffusivities that vary over several orders of magnitude, control over the mixed-linker ZIF-8-90 crystal size is critical. For example, the uptake of *i*-butane is slow enough to allow reliable diffusivity measurements at 35°C with 1-10 μm crystals, whereas crystals larger than 50 μm are required to accurately measure *n*-butane diffusivities. I synthesized ZIF-8-90 mixed linker crystals of diameters ranging from 338 nm to 120 μm for uptake measurements. The mixed-linker crystals were synthesized solvothermally, and equimolar amounts of sodium formate and organic linkers were used to obtain a macroscopically random linker distribution in the framework. Thermodynamically, the $Zn^{2+}$ metal center favors crystallization with 2-MeIM than with OHC-IM.[100] However, in the presence of sufficient concentrations of sodium formate, both linkers will be largely deprotonated before addition of $Zn^{2+}$ ions.[97] This allows kinetic control of the metal-linker coordination reaction, and allows the formation of mixed-linker frameworks of continuously variable compositions. Figure 8 (Supporting Information) shows example SEM images of the large range of crystal sizes

synthesized, and Figure 9 shows the crystal size distributions obtained from DLS, SEM, or optical microscopy. The ZIF-8/ZIF-90 structure topology of all the materials was confirmed by powder XRD (Figure 10).

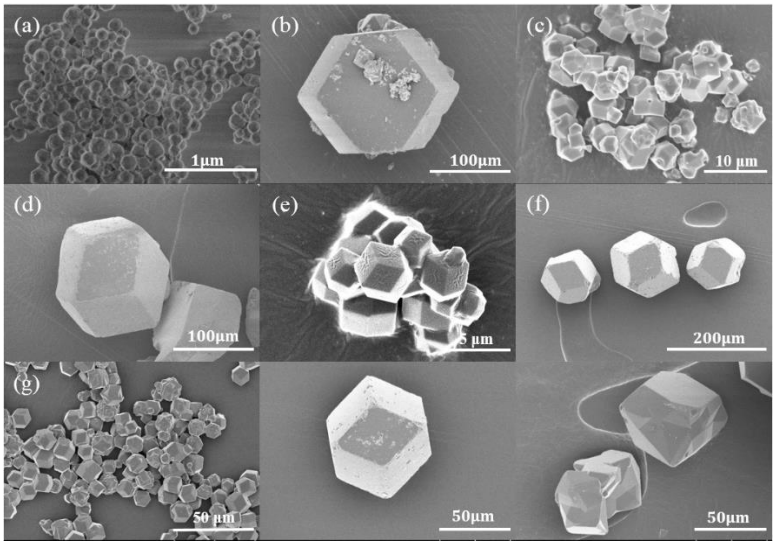


**Figure 8.** Example SEM images of: (a) 338 nm ZIF-8, (b) 112.0 μm ZIF-8, (c) 3.9 μm ZIF-$8_{63}$-$90_{37}$, (d) 80.4 μm ZIF-$8_{63}$-$90_{37}$, (e) 3.5 μm ZIF-$8_{28}$-$90_{72}$, (f) 87.1 μm ZIF-$8_{28}$-$90_{72}$, (g) 10.3 μm ZIF-$8_{7}$-$90_{93}$, (h) 60.6 μm ZIF-$8_{7}$-$90_{93}$, and (i) 55.7 μm ZIF-90 crystals. The crystal sizes listed here are the number averages obtained from the crystal size distributions

.

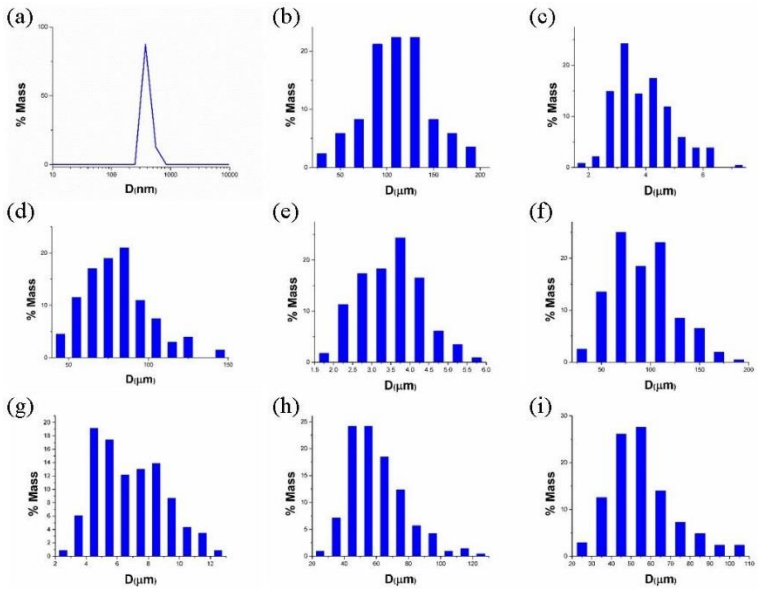


**Figure 9.** Crystal size distributions (CSDs) of: (a) 338 nm ZIF-8, (b) 112.0 μm ZIF-8, (c) 3.9 μm ZIF-$8_{63}$-$90_{37}$, (d) 80.4 μm ZIF-$8_{63}$-$90_{37}$, (e) 3.5 μm ZIF-$8_{28}$-$90_{72}$, (f) 87.1 μm ZIF-$8_{28}$-$90_{72}$, (g) 10.3 μm ZIF-$8_{7}$-$90_{93}$, (h) 60.6 μm ZIF-$8_{7}$-$90_{93}$, and (i) 55.7 μm ZIF-90 crystals. The crystal sizes listed here are the number averages obtained from the CSDs, and example SEM images of these crystals are shown in Figure 8. The CSDs were obtained by DLS for sample (a), by SEM for samples (c, e, g), and by optical microscopy for samples (b, d, f, h, i).

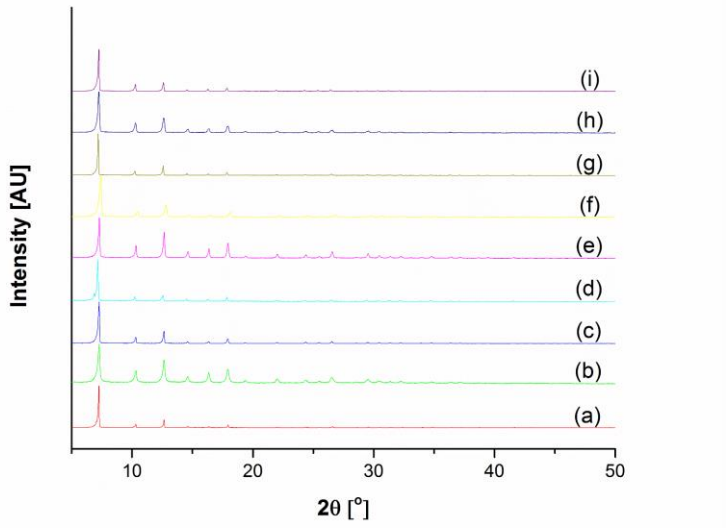


**Figure 10.** Powder XRD patterns of the materials shown in Figure 8 and Figure 9: (a) 338 nm ZIF-8, (b) 112.0 μm ZIF-8, (c) 3.9 μm ZIF-$8_{63}$-$90_{37}$, (d) 80.4 μm ZIF-$8_{63}$-$90_{37}$, (e) 3.5 μm ZIF-$8_{28}$-$90_{72}$, (f) 87.1 μm ZIF-$8_{28}$-$90_{72}$, (g) 10.3 μm ZIF-$8_{7}$-$90_{93}$, (h) 60.6 μm ZIF-$8_{7}$-$90_{93}$, and (i) 55.7 μm ZIF-90 crystals. The crystal sizes listed here are the number averages obtained from the CSDs.

### 2.3.2. Composition Analysis

In general, one expects thermodynamic and kinetic differences in the incorporation of the two different linkers in the ZIF crystal structure. As a result, the percentage ($x$) of ZIF-8 linkers in the crystallized material is not identical to that originally present in the synthesis solution. It is therefore necessary to establish the 'composition curve' that relates the two quantities and allows selection of the appropriate synthesis solution for a particular hybrid ZIF-8-90 material.[2] Solution-phase $^{1}$H-NMR spectroscopy is a reliable tool for this purpose, and the composition curves thus determined are shown in Figure 11. Due to the different synthesis conditions (and hence different crystallization characteristics) used in the synthesis of 'smaller' (< 10 μm) and 'larger' (> 50 μm) ZIF-8-90 crystals, the composition curves are different for the two cases. Overall, it is seen that 2-MeIM is incorporated into the frameworks at lower fractions than present in the initial reactant solution. The data in Figure 11 is in good agreement with our initial data for small crystals of ZIF-8-90 materials.[88] Based upon the foregoing results, it is clear that ZIF-8-90 hybrids of any composition and a large range of average crystal sizes can be synthesized by the combination of techniques used in this work.

[2] This crystal composition analysis was done by Nair group member Dr. Fereshteh Rashidi (Post Doc, School of Chemical & Biomolecular Engineering, Georgia Institute of Technology).

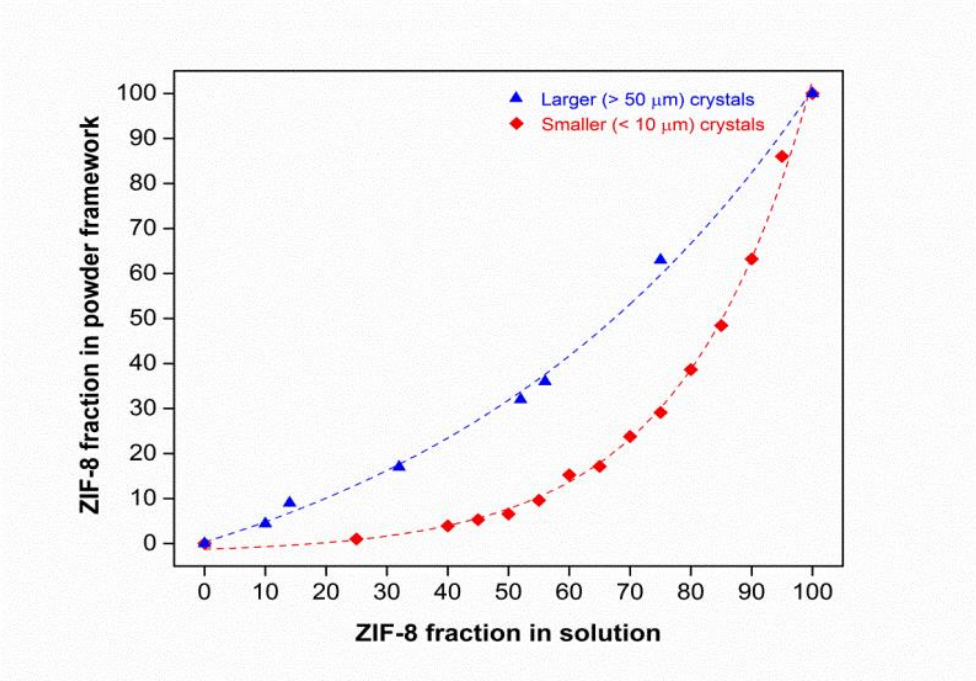


**Figure 11.** Composition analysis curves of ZIF-$8_x$-$90_{100-x}$ hybrid frameworks obtained by solution $^1$H-NMR. Composition curves for smaller (< 10 mm) and larger (> 50 mm) crystals are shown. The composition of the hybrid materials can be continuously tuned by adjusting the composition of the synthesis solution. The dashed lines are only a guide to the eye.

The XRD patterns of ZIF-8-90 materials are all essentially identical (Figure 10) because all the materials have the same framework topology and only a small difference in electron density. In these circumstances, it is difficult to obtain direct evidence of compositional variations by powder diffraction techniques. Previously[88], we provided indirect evidence (via $N_2$ physisorption measurements) that the crystallized ZIF-8-90 materials were true hybrids and not physical mixtures of ZIF-8 and ZIF-90 crystals. However, conclusive evidence of hybrid crystal formation, as well as the distribution of the ZIF-8 linker fraction ($x$) across individual crystals, can only be obtained from a micro analytical technique. Here we use a comparative approach based upon micro-Raman and

powder FT-Raman spectroscopy.[3] Figure 12(a) shows powder FT-Raman spectra from several ZIF-8-90 materials. We use the peaks at 680 $cm^{-1}$ (ring puckering of 2-MeIM) and 1680 $cm^{-1}$(C=O stretching vibration of OHC-Im) as signatures[11-13] of the ZIF-8 and ZIF-90 linkers, respectively. We then obtain the integrated areas ($I_{ZIF8}$ and $I_{ZIF90}$) of these peaks in each spectrum, and use the normalized quantity $X = 100 \times I_{ZIF8}/(I_{ZIF8}+I_{ZIF90})$ as a measure of the percentage of ZIF-8 linkers in the framework. A similar procedure is carried out using micro-Raman spectra collected from at least six randomly selected individual crystals in each sample, and at three different locations on each selected crystal. Figure 12(b) shows example micro-Raman spectra from one crystal in each ZIF-8-90 sample. The quantity $X$ allows the cancellation of sample size effects, but is not the exact equivalent of the ZIF-8 linker fraction ($x$) because of the different polarizabilities of the two characteristic linker vibrations. However, if the crystals are true hybrids, the 'bulk' macroscopic value of $X$ obtained from a powder FT-Raman measurement must be similar to that obtained microscopically by micro-Raman measurements from individual crystals and locations in the sample. Moreover, a small standard deviation of $X$ (as obtained from averaging the micro-Raman measurements over multiple crystals) would denote a highly uniform value of the ZIF-8 linker percentage $x$ across crystals in a given powder sample. Figure 12(c) plots the values of $X$ obtained from FT-Raman and micro-Raman measurements versus the values of $x$ obtained previously from $^1$H-NMR measurements. The FT-Raman and micro-Raman techniques are in close agreement, providing clear evidence that the crystals are true mixed-linker hybrids.

[3] This micro-Raman and powder FT-Raman spectroscopy were done by Nair group member Dr. Fereshteh Rashidi (Post Doc, School of Chemical & Biomolecular Engineering, Georgia Institute of Technology).

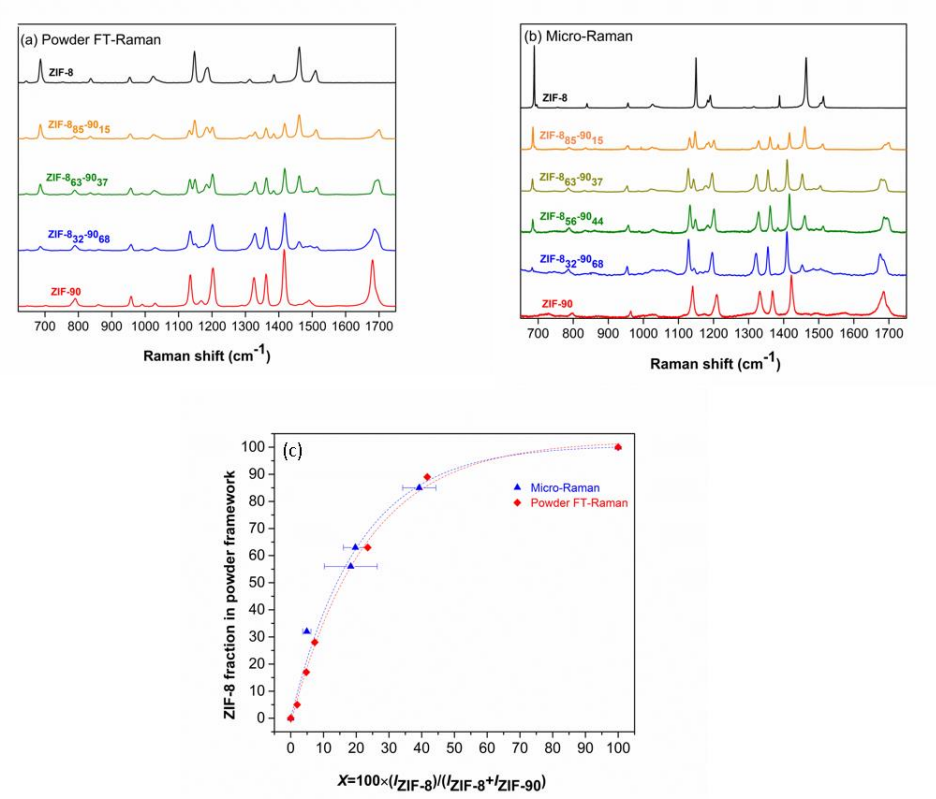


**Figure 12.** (a) Powder FT-Raman spectra of ZIF-8-90 hybrid framework materials, (b) micro-Raman spectra from individual ZIF-8-90 crystals, and (c) Composition analysis of ZIF-8-90 hybrid crystals from FT-Raman and micro-Raman data. The quantity $X = 100\times I_{ZIF8}/(I_{ZIF8}+I_{ZIF90})$ is obtained from the Raman measurements whereas the quantity $y$ is the corresponding ZIF-8 linker fraction obtained from $^{1}$H-NMR. The error bars shown for the micro-Raman curve represent the standard deviation in $X$ across at least six different crystals of the sample and three different locations in each crystal.

The generally small standard deviations (represented as horizontal error bars in Figure 12c) of $X$ also indicate good compositional uniformity of the ZIF-8-90 crystals. It is important to note that the above discussion does not provide insight on the *molecular-level* distribution of the two different linkers within the ZIF crystals. As recently shown, such understanding could be obtained in a specific MOF system through a combination of NMR spectroscopy and structure modeling.[101] The present work, on the other hand, is focused on demonstrating the role of linker substitution in obtaining large changes in adsorption and diffusion behavior.

### 2.3.3. Adsorption in ZIF-8-90

Volumetric uptake profiles of *n*-butane and *i*-butane were collected at 308 K for five materials with $x$ = 100, 63, 28, 7, and 0, representing decreasing ZIF-8 linker content and increasing effective pore size from pure ZIF-8 to pure ZIF-90. Figures 13 show the adsorption isotherms obtained at equilibrated conditions up to a pressure of about 1.8 bar. The data are fitted to Langmuir isotherms. The fitted Langmuir capacity ($C_s$), affinity constant ($b$) and the Henry constant ($K = C_s.b$) are tabulated in Table 2. There is a general increase in the Langmuir capacity and Henry constant with the fraction of ZIF-8 linkers, due to the more favorable interactions of alkanes with the methyl groups of the 2-MeIM linker. All the ZIF-8-90 materials slightly favor *i*-butane adsorption over *n*-butane. Overall, the adsorption properties show moderate changes as a function of $x$, as expected for adsorption of alkanes in ZIF materials which is governed by van der Waals interactions of the alkyl groups with the framework.

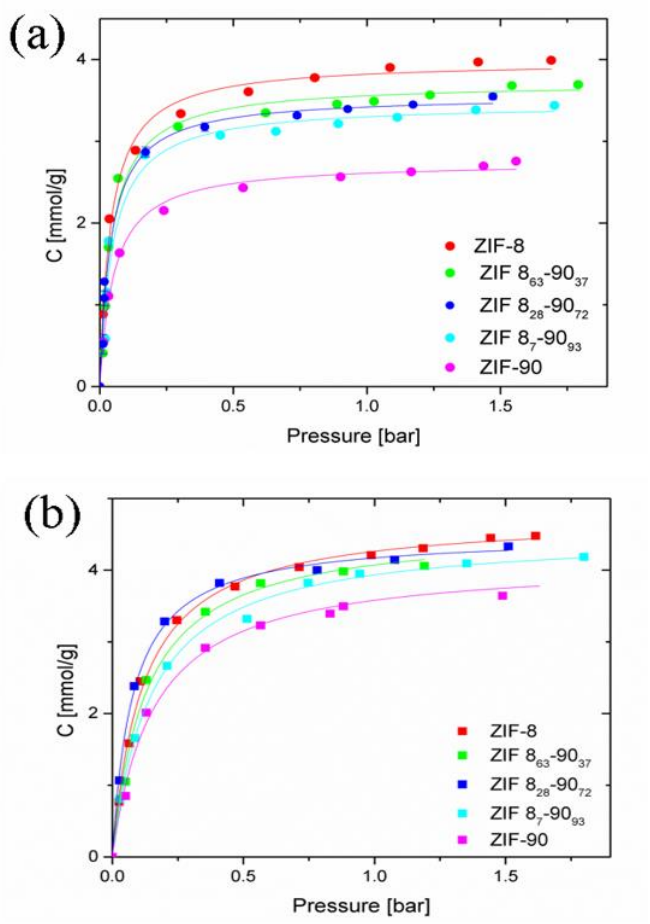


**Figure 13.** Adsorption isotherms at 35°C of (a) *n*-butane and (b) *i*-butane, for materials with ZIF-8 linker percentage $x$ = 100 (pure ZIF-8), 63, 28, 7, and 0 (pure ZIF-90). The solid lines represent Langmuir model fits, with parameters shown in Table 2.

**Table 2.** Langmuir model parameters and Henry constants at 35°C.

| Material | *n*-butane | | | *i*-butane | | |
|---|---|---|---|---|---|---|
| | $C_s$ mmol/g | $b$ 1/bar | $K$ mmol/(g·bar) | $C_s$ mmol/g | $b$ 1/bar | $K$ mmol/(g.bar) |
| **ZIF-8$_{100}$-90$_0$** | 4.0±0.1 | 24±2 | 96±8 | 4.8±0.1 | 9±1 | 41±2 |
| **ZIF- 8$_{63}$-90$_{37}$** | 3.7±0.1 | 22±3 | 82±10 | 4.6±0.1 | 8±1 | 36±5 |
| **ZIF- 8$_{28}$-90$_{72}$** | 3.6±0.1 | 24±3 | 85±11 | 4.5±0.1 | 13±1 | 59±3 |
| **ZIF- 8$_7$-90$_{93}$** | 3.5±0.1 | 20±3 | 71±12 | 4.5±0.1 | 7±1 | 30±2 |
| **ZIF-8$_0$-90$_{100}$** | 2.8±0.1 | 19±1 | 52±4 | 4.2±0.1 | 6±1 | 26±3 |

### 2.3.4. Diffusion in ZIF-8-90

To clearly isolate the effect of pore tunability on molecular sieving in ZIF-8-90 materials, I again focus on the low-pressure regime wherein adsorbate-adsorbate interactions have minimal impact. In the case of the two hydrocarbon isomers *n*-butane and *i*-butane, the transport (i.e., Fickian) diffusivities are obtained by fitting the initial linear gravimetric uptake curves with an analytical model for uptake in spherical particles of given CSD (see Supporting Information for details of the methodology). To further elucidate the role of tunable molecular sieving, I obtain the corrected (Maxwell-Stefan, M-S) diffusivity from the transport diffusivity.[71] The M-S diffusivity captures the intrinsic rate of hopping of individual molecules through the pore windows of the material. Figure 14 shows the butane isomer transport diffusivities, M-S diffusivities, and the corresponding *n*-butane/*i*-butane diffusion selectivities of ZIF-8-90 materials. The data is also listed in Tables 3-4. It is clear that the *n*-butane and *i*-butane transport diffusivities can be tuned continuously over 2-3 orders of magnitude by variation of the ZIF-8 linker fraction ($x$). The *n*-butane diffusion selectivity over *i*-butane can be tuned between 900-50,000. A decreasing value of $x$ leads to an increase in the effective pore size and allows faster hopping of both butane isomers through the pore windows. All the ZIF 8-90 materials have quite a sharp intrinsic selectivity for *n*-butane (kinetic diameter 0.43 nm) over *i*-butane (0.5 nm). However, several important considerations drive the selection of an optimum material for membrane-based separation of butane isomers based upon Figure 14. Materials close to ZIF-8 have impractically low *n*-butane diffusivities. Hence, materials closer to ZIF-90 are desired. The *n*-butane diffusivity appears to reach a plateau when $x$ decreases below 28, whereas such an effect is not observed with *i*-butane. This is likely due to an uncertainty

in determining accurate *n*-butane diffusivities in the larger-pore materials, due to fast *n*-butane diffusion and potential contamination of the data by external and surface mass transfer resistances even in the largest crystals used in this work. On the other hand, the data may also include a real effect, i.e., additional increase in the pore size at smaller values of *x* can no longer affect significantly the diffusion of the smaller hydrocarbon *n*-butane, whereas the larger *i*-butane continues to feel the limiting effect of the pore size. In either case, Figure 14 shows that materials close to ZIF-90 ($0 < x < 30$) are appropriate choices for *n*-butane/*i*-butane separation based on molecular sieving, since they combine high *n*-butane diffusivity ($> 2\times10^{-9}$ $cm^2/s$) and high selectivity (at least 900-6000, considering the measured *n*-butane diffusivities as lower-bound values).

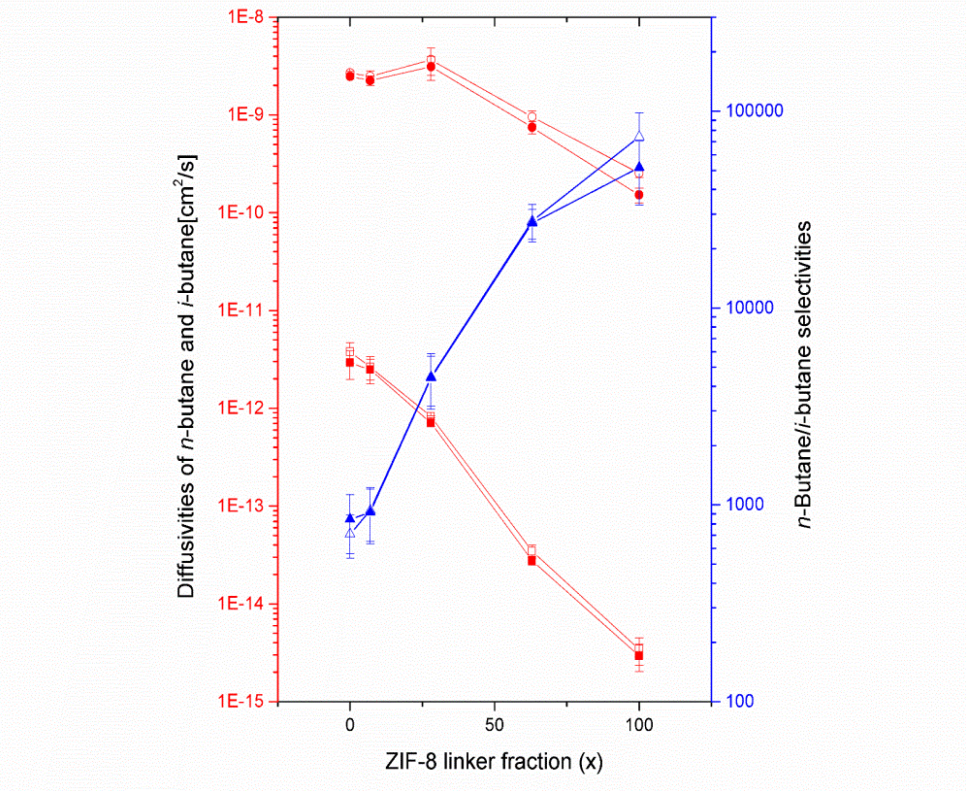


**Figure 14.** Fickian (open symbols) and corrected Maxwell-Stefan (closed symbols) diffusivities of *n*-butane and *i*-butane (left axis), and the corresponding *n*-butane/*i*-butane selectivities (right axis) of ZIF 8-90 materials with varying values of *x*, measured at 308 K.

**Table 3.** Transport (Fickian) diffusivities of *n*-butane and *i*-butane in ZIF 8-90 mixed linker varying materials at 35°C, measured at an initial pressure of 0.2 bar and a final pressure of 0.03 bar. The error bars are based upon measurements using three independently synthesized powder samples of each ZIF material.

| | ***n*-butane** | ***i*-butane** | **Selectivity** |
|---|---|---|---|
| **Material** | Diffusivity $[10^{-9}cm^2/s]$ | Diffusivity $[10^{-12}cm^2/s]$ | |
| **ZIF-8** | 0.25±0.03 | 0.003±0.002 | 70000±20000 |
| **ZIF $8_{63}$-$90_{37}$** | 0.95±0.15 | 0.035±0.005 | 28000±6000 |
| **ZIF $8_{28}$-$90_{72}$** | 3.7±1.2 | 0.82±0.02 | 4000±1000 |
| **ZIF $8_{7}$-$90_{93}$** | 2.5±0.3 | 2.6±0.7 | 900±300 |
| **ZIF-90** | 2.7±1.2 | 3.8±0.9 | 700±200 |

**Table 4.** Corrected M-S diffusivities of *n*-butane and *i*-butane in ZIF 8-90 mixed linker materials at 35°C, obtained from the transport diffusivities shown in Table 3.

| | ***n*-butane** | ***i*-butane** | **Selectivity** |
|---|---|---|---|
| **Material** | Diffusivity $[10^{-9}cm^2/s]$ | Diffusivity $[10^{-12}cm^2/s]$ | |
| **ZIF-8** | 0.15±0.03 | 0.003±0.001 | 50000±20000 |
| **ZIF- $8_{63}$-$90_{37}$** | 0.7±0.1 | 0.028±0.003 | 27000±5000 |
| **ZIF- $8_{28}$-$90_{72}$** | 3.1±0.9 | 0.71±0.06 | 4000±1000 |
| **ZIF- $8_{7}$-$90_{93}$** | 2.3±0.3 | 2.5±0.7 | 900±300 |
| **ZIF-90** | 2.5±0.2 | 2.9±1.0 | 800±300 |

## 2.4 Conclusions

I have demonstrated the continuous tuning of molecular sieving and adsorption behavior in mixed-linker ZIF-8-90 frameworks, which is due to the tunability of effective pore size as well as the ratio of polar and non-polar functional groups in the framework. These results are facilitated by the synthesis of a range of ZIF-8-90 mixed linker materials with average crystal sizes spanning from 338 nm to almost 100 μm, and the detailed determination of the CSDs. Micro-Raman composition analysis of individual ZIF-8-90 crystals conclusively shows the hybrid nature and high uniformity of the mixed-linker materials. The *n*-butane and *i*-butane diffusivities and the *n*-butane/*i*-butane diffusion selectivity can be continuously tuned over several orders of magnitude, allowing the selection of suitable materials for membrane-based separation of these isomers. This detailed demonstration of tunable adsorption and diffusion properties in ZIF-8-90 materials opens up the wider applicability of mixed-linker ZIF materials as a platform for a variety of membrane-based and adsorption -based molecular separations.

# CHAPTER 3.

# INTERFACIAL MICROFLUIDIC MEMBRANE PROCESSING (IMMP): DEVELOPMENT, METHANISTIC STUDIES, AND OPTIMIZATION[4]

## 3.1. Introduction

The chemical industry relies heavily on energy-intensive separation technologies such as distillation. For example, approximately 0.45 quads of energy (1 quad= $10^{16}$ BTU) are used yearly for olefin/paraffin separations using cryogenic distillation columns that contain nearly 200 stages.[102] Membrane-based separation is an attractive alternative for energy efficient olefin/paraffin separations and many other molecular separations.[103] Although polymeric membranes have low cost and high processibility[104], their performance limitations (represented by the Robeson 'upper bound')[105] make them unviable for olefin/paraffin separations. Metal-organic frameworks (MOFs), which are crystalline materials comprised of organic linkers and metal ions, have recently shown interesting molecular separation properties.[1] For example, the MOF material ZIF-8 shows exceptionally high performance for propylene/propane separation.[44] Furthermore, the synthesis conditions required for MOF membrane formation are much more benign than those of other molecular sieves such as zeolites and carbons, and their diffusion properties can be finely controlled by structural variations.[22,27,106]

[4] Reprinted with permission from K. Eum, A. Rownaghi, D. Choi, R. R. Bhave, Christopher W. Jones, S. Nair, "Fluidic Processing of High-Performance ZIF-8 Membranes on Polymeric Hollow Fibers: Mechanistic Insights and Microstructure Control", Advanced functional materials, 2016, Copyright 2016 John Wiley and Sons.

An important issue impeding the realization of industrially attractive MOF membranes is the lack of a scalable and inexpensive membrane fabrication process. Several reports have described in detail the synthesis of ZIF membranes on disk-type and tubular inorganic supports such as alumina, zirconia, and titania.[65,107] However, such membranes have very low surface-to-volume ratio, are expensive due to the use of ceramic supports, and require intermediate synthesis steps or post-synthesis treatment steps.[35,108] These challenges can potentially be overcome by fabrication of MOF membranes on low-cost polymeric supports that also permit enhanced interfacial compatibility with the MOF membrane layer.[109] In particular, hollow fiber supports provide high throughput by increasing the active surface area to volume ratio (>1000 $m^2/m^3$).[110] For example, our group previously reported ZIF-90 membranes fabricated by static seeded growth on the outer surfaces of polyamide(imide) (PAI, specifically Torlon®) hollow fibers of 300 μm OD by immersion in a methanolic precursor solution at mild conditions (65°C).[34] More recently we introduced an interfacial microfluidic membrane processing (IMMP) methodology for MOF membrane fabrication in PAI hollow fibers with specific application to ZIF-8 membranes, and demonstrated control over membrane position and morphology.[9] The IMMP module acts as both a membrane fabrication apparatus as well as an *in situ* permeation measurement device. Importantly, ZIF-8 membrane fabrication did not require seeding procedures, nor pre-treatment with interface compatibility promoters or reactant sources such as ZnO or poly(ethyleneimine). Other recent works have also reported the fabrication and properties of MOF (including ZIF) membranes on polymeric tubes or hollow fibers using either static or fluidic techniques, highlighting their promising performance in a variety of gas

separations.[40,111,112] However, the above initial demonstrations reveal that hollow-fiber MOF membrane processing is still at an early stage, and require detailed understanding and control of the mechanisms of MOF membrane growth under fluidic conditions in the confined spaces of microscale hollow fibers. In this work, I firstly demonstrate detailed IMMP studies that lead to a mechanism of ZIF-8 membrane growth in hollow fibers that elucidates the roles of reactant transport, film crystallization, and the hollow fiber support microstructure. Secondly, I demonstrate how the mechanistic understanding of ZIF-8 hollow fiber membrane formation can be used to engineer a higher-throughput, higher-selectivity membrane for propylene/propane separation. Finally, I also present detailed binary and ternary mixed gas ($H_2/C_3H_8$, $C_3H_6/C_3H_8$, and $H_2/C_3H_6/C_3H_8$) permeation measurements to highlight the excellent separation characteristics of ZIF-8 hollow fiber membranes.

## 3.2 Experimental Methods

### 3.2.1. Materials

2-Methylimidazole (99%, 2-MeIM) and $Zn(NO_3)_2{\cdot}6H_2O$ (99%) were obtained from Sigma-Aldrich. 1-Octanol was obtained from Acros Organics and methanol (99%, MeOH) was obtained from Alfa Aesar. Deionized water (DI-water) was produced with a Thermo Scientific 7128. Translucent epoxy (DP 100), and Fluorinert (FC-40) and were obtained from 3M. Corning Sylgard 184 was purchased from Ellsworth Adhesives. Torlon® 4000T-HV, a commercially available polyamide-imide (PAI) (Solvay Advanced Polymers, Alpharetta, GA) was used as the major polymer in this study. Reagent grade with 99% purity N-Methyl-2-pyrrolidone (NMP), ethanol (EtOH), and lithium nitrate were obtained

from Sigma Aldrich to form the fiber spinning dope. Methanol (ACS grade, VWR) and hexane (ACS Reagent, >98.5%, VWR) were used for solvent exchange after fiber sorbent spinning.

### 3.2.2. IMMP Modules

As shown in Figure 15, the body of the module was machined in-house from a 3" x 3" x 1.5" SS 304 block. Top: 2" diameter cylinder with 1.38" depth was drilled into the center of the top face; a groove was machined to accept an o-ring with an inner diameter of 2.25" and 0.6" cross-section (AS568-035); a hole to accommodate a 10-32 hex screw was placed in each corner of the top, 0.35” away from the o-ring; a hole for a temperature probe was drilled into the top near one of the holes for a hex screw; Sides: a hole with the specifications for 1/8” NPT fittings was drilled into the center of each face. Side A holes were a 1" height and not completely bored through. A 0.1" thick wall remained, in which a smaller 0.02" hole was bored through to create an aperture for fiber mounting. Side B holes were offset 1/8" higher than Side A and were completely bored through into the interior. Lid: a 3" x 3" x ¼" SS 304 block was used as a lid. Holes corresponding to the positions of the hex screws and temperature probe were machined into the lid to create a flange seal with an O-ring upon tightening the lid to the base.

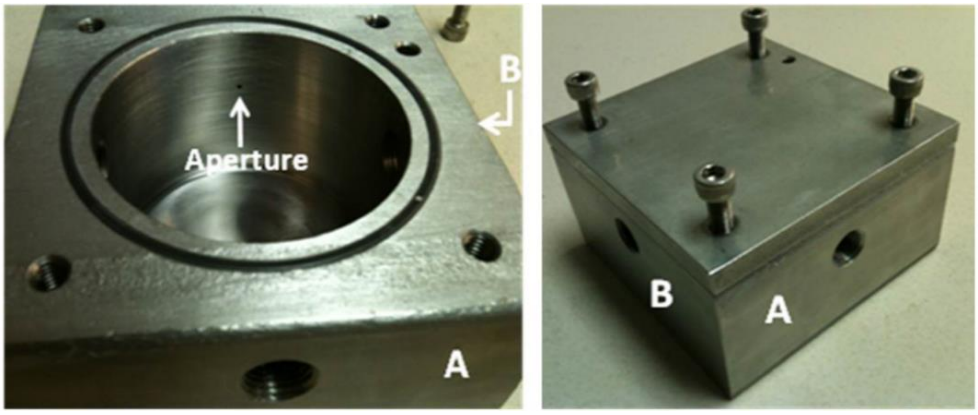


**Figure 15.** IMMP module for MOF membrane synthesis in hollow fibers. Dimensions are as described in the Materials and Methods section.

### 3.2.3. Mounting/Sealing of Bare Fibers

A 4" length of Torlon® fiber substrate was inserted horizontally through the holes of Sides B. A small drop of 3M translucent epoxy was then applied to the shell of each fiber end where the fiber contacts the module interior. After allowing the epoxy to cure at least 90 minutes, the excess fiber ends were removed with tweezers. The permeances of the mounted fibers were then collected to ensure that the fiber was properly sealed by the epoxy and that the bore had not been crushed/blocked.

### 3.2.4. Synthesis of ZIF-8 Membrane

*Cases 1 and 2:* 10 mL of neat 1-octanol was first introduced through the bore side of the fiber using syringe pump and the pump rate was set to 2ml/min. 9 g of 2-MeIM and 0.22 g of zinc nitrate hexahydrate were each dissolved in 80 mL DI-water and 40 mL 1-octanol. 3mL of $Zn(NO_3)_2 \cdot 6H_2O$ /1-octanol solution was introduced through the bore side of the fiber using syringe pump with the flow rate of 0.6 ml/hr. Temperature of IMMP module was set and maintained to 30°C. Then 2-MeIM/DI-water solution was slowly poured into the IMMP module while stirring the solution at 60 rpm. Syringe pump

was stopped for 210 min after 120 min of continuous membrane grow step. Syringe pump was turned on again for 20 min followed by another 210 min of static growth step. Pump flow rate was changed to 2ml/min and 10 mL of neat 1-octanol was introduced through the bore side of the fiber while the 2-MeIM/DI-water solution was replaced with fresh DI-water three times to quench the reaction and remove excessive ZIF precursors. 10 mL of heptane solution was flowed through the bore side of the fiber while shell solution was replaced with heptane to remove the 1-octanol. Next, similar procedure was performed with more volatile hexane solution. Lastly, 20 mL of MeOH was introduced into the bore side of the fiber and the shell solution was replaced with MeOH. The membrane was dried at room temperature for 2 days. *Case 3:* Membranes was prepared with same synthesis procedure of Case 1 and 2 membranes except for the temperature profile. The continuous membrane growth step was begun at 22 °C and with a linear increase in temperature to 42°C over 25 mins followed by a decrease to 30°C over 60 mins and steady holding at the latter temperature for the remainder of the synthesis.

### 3.2.5. End Sealing of Membranes

A 9 wt% PDMS (Sylgard 184)/heptane solution was heated at 90°C under vigorous stirring for 4 hr to thermally crosslink the PDMS.[113] After cooling to 25°C, a 2 μL PDMS droplet was applied to the end of the mounted module using capillary action. Argon gas was immediately flowed through the fiber bore upon addition of the PDMS/heptane solution followed by curing at 120°C for 2 hr.

### 3.2.6. Fabrication of Torlon Hollow Fiber Supports

The initial Torlon® (Polyamide-imide) hollow fibers of OD 300 µm and ID 200 µm were produced by a spinning method identical to that reported by us in several previous works.[114] The new type of Torlon® fibers of OD 360 µm and ID 270 µm and enhanced porosity were fabricated by a modified spinning approach. The optimized polymer dope compositions and modified spinning conditions are shown in Table 5. Non-volatile solvent (NMP), non-solvent (DI-water) and pore formers ($LiNO_3$) in the dope composition, quench bath temperatures (i.e., 25 °C), take-up rate (i.e., 40 $m.min^{-1}$) and air gap height (i.e., 15 cm) were applied in order to identify a robust process window to produce hollow fibers with engineered surface porosity. The key parameters control the morphology of the hollow fibers namely, composition of the polymer dope, composition of the bore liquid, height of the air gap and spinning speed. A developed Torlon® (Figure 16) core dope was fed to the spinneret compartment. The extruded polymer dope passed through an air-gap and into a water quench bath (primary coagulant) where the fiber phases separate. A standard bore fluid used in this study comprise NMP and DI-water with the weight ratio of 85:15. The fiber then passed over a Teflon® guide and was collected on a rotating take-up drum partially submerged in a second water-bath, which was continuously replenished with fresh water. Next, fibers spun under identical conditions were removed from the take-up drum, tied loosely and soaked in DI-water for 5 days at room temperature (25 °C) with fresh DI-water added daily to remove any residual NMP and promote complete removal of the water-soluble $LiNO_3$. The DI-water present in the fiber was then solvent exchanged by immersion for 1 h each in three batches of fresh methanol (to remove excess water) and then 1 h each in three batches of

fresh hexane (to remove excess methanol). After a 2 h air drying step, PAI fibers were dried at 130 °C for 24 h to completely remove any residual NMP.

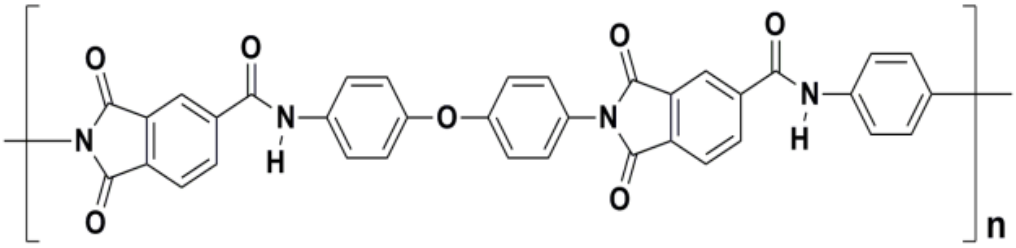


**Figure 16.** Chemical structure of Torlon®

**Table 5.** Optimized spinning conditions of Torlon® (polyamide-imide) hollow fibers.

| **Dope composition (PAI/$LiNO_3$/NMP/ethanol) (wt %)** | **15/15/66/4** |
|---|---|
| **Dope flow rate (ml/hr)** | 300 |
| **Bore fluid (NMP/DI-water) (wt %)** | 85/15 |
| **Bore fluid flow rate (ml/hr)** | 100 |
| **Air gap (cm)** | 15 |
| **Take up rate (m/min)** | 40 |
| **Operating temperature (°C)** | 27 |
| **Quench bath temperature (°C)** | 25 |

### 3.2.7. Characterization

XRD patterns were measured on a PANalytical X'Pert Pro diffractometer at room temperature using Cu Kα radiation of λ = 0.154 nm and a scanning range of 5-40° 2θ. Cross-sectional images of ZIF-8 inner surface membrane were examined using Hitachi SU 8010 scanning electron microscope after a thin layer of gold was sputtered onto the

cross-sectional surface. The samples were soaked with a hexane solution for 30 min followed by dipping into liquid nitrogen for a clean cut. For scanning probe microscopy (SPM) of the hollow fiber support surfaces, the fibers were immersed in hexane followed by immersion of the saturated fibers in liquid nitrogen. The fibers were then gently broken into several pieces, which were then transferred to a silicon wafer for the SPM surface roughness measurements. The RMS surface roughness was obtained by averaging data from several 2 μm × 2 μm area images. Permeance data were collected by the steady-state Wicke-Kallenbach technique.[76] A precisely determined flow rate (10 mL/min) of feed (single-component or binary/tertiary mixture) was continuously injected to the bore side at 1 atm *via* a mass flow controller (MFC). The injected gases were contacted in a mixer before entering the feed side of the IMMP module. Argon was used as the sweep gas at the permeate side and the flow rate was set to 30 mL/min. A similar apparatus was used for measurements at higher feed pressures (up to 6 bar), except that MFCs rated for high-pressure operation were used. The composition of the permeate stream was analyzed by on-line gas chromatography (Shimadzu GC-2014). Membrane defect characterization was performed with permporosimetry equipment with the IMMP Module directly acting as a permeation module. First, helium was introduced into one end of the bore side of the membrane while plugging the other end with a Swagelok fitting. The pressure differential between the bore and the shell side was thus controlled from 0-90 psi and the shell-side helium flow rate was measured using a digital flow meter. Then, the bore side of the membrane was saturated with Fluorinert (FC-40) solution that has a low surface tension. Then the helium flow rate was measured again. Atomic force microscopy (AFM) images of inner surfaces of the hollow fibers were obtained with an ICON Dimension® scanning

probe microscope (Bruker). The AFM was operated under tapping mode with Mikromasch NSC14 silicon cantilevers (8 nm tip radius, 5 N/m force constant, and 160 kHz typical resonance frequency).

## 3.3. Results and Discussion

### 3.3.1. IMMP Mechanism

Figure 17(a) shows a schematic of IMMP for ZIF-8 membrane fabrication on the inner surface (bore side) of PAI (Torlon®) hollow fibers. Further details of the IMMP method are described in my recent works and in the Experimental Methods section.[9,115] The formation of a ZIF-8 membrane is achieved in an opposing-reactants geometry[116] by contacting the two reactant streams ($Zn^{2+}$ ions dissolved in 1-octanol on the bore side, and 2-methylimidazole dissolved in water on the shell side) across the porous hollow fiber support. In the present case, the two solvents are chosen to be immiscible, thereby allowing a sharp interface between the two phases. The two immiscible solvents (1-octanol and DI-water) keep the reactants separated in different phases everywhere except at the interface, thereby allowing ZIF-8 nucleation only at the surface of the hollow fiber (where the interface is deliberately created by use of appropriate initial conditions). The use of a large excess of 2-mIm (2-mIm/Zn concentration ratio = 75) allows $Zn^{2+}$ to act as a limiting reactant, thereby leading to ZIF-8 film formation on the inner surface. The temporal flow profile in the bore side is shown in Figure 17b. It comprises four steps: 120 min of membrane formation under continuous flow of 62 μL/hr $Zn^{2+}$/octanol solution (Step 1), 210 min of membrane growth under static conditions (Step 2), 20 min of $Zn^{2+}$/octanol solution replenishment at a continuous flow of 62 μL/hr step (Step 3), and a

final 210 min of static growth (Step 4). Two different temperature profiles are also shown in Figure 17(b) and will be discussed below. To investigate the membrane formation process, I repeated the IMMP process multiple times and arrested the membrane growth at three different selected points as indicated by the numbered temporal locations in Figure 17(b). The growth arrest was carried out by introducing neat 1-octanol through the bore side of the fiber while exchange the shell side solution with fresh MeOH. Binary propylene/propane permeation measurements were then conducted *in situ* at each arrest point, and finally each membrane was removed from the IMMP module and cross-sectioned for SEM imaging and thickness measurements.

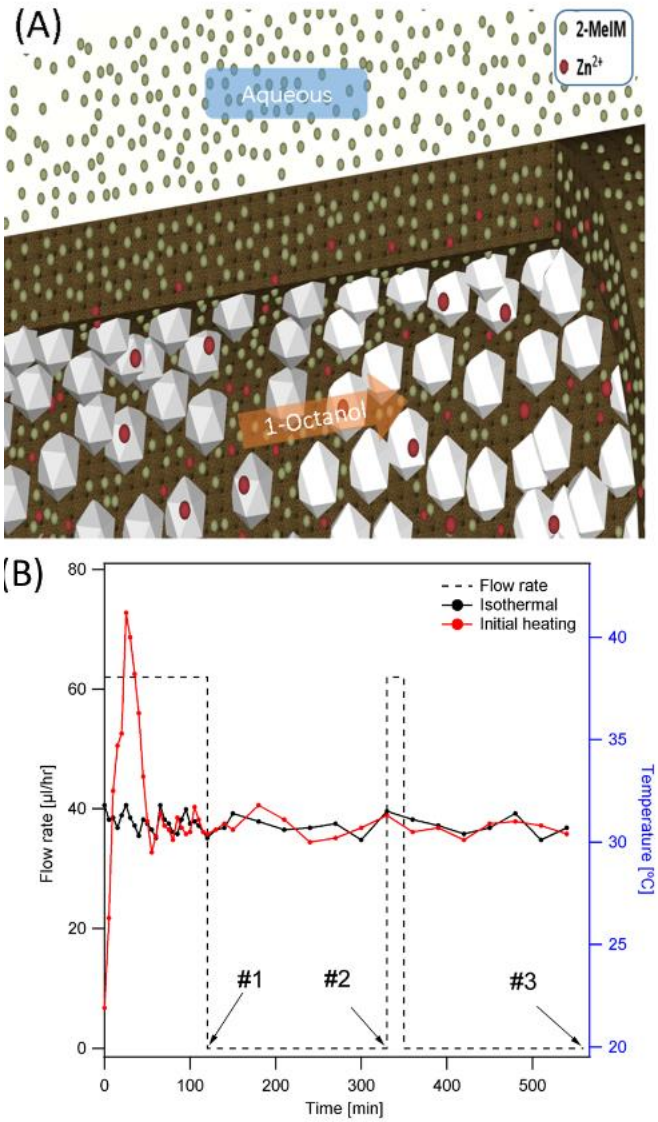


**Figure 17** (A) Schematic of the IMMP geometry showing the two feed streams for ZIF-8 membranes in hollow fibers, (B) Bore flow rate and two different temperature profiles (isothermal and initial heating) to synthesize ZIF-8 membranes on the inner surface of Torlon® hollow fibers. The numbered temporal locations (#1, #2, and #3) indicate the times where the membrane growth were arrested.

Initially, ZIF-8 membrane growth was carried out using a pre-heated IMMP module which was maintained at isothermal conditions of 31.0 ± 0.5°C (Figure 1b) throughout the process. Figures 18a-18c show the development of the membrane morphology at the three different arrest points shown in Figure 17b. Table 6 and Table **7** show information

about the membrane thickness and olefin/paraffin permeation characteristics at these points. At the outset, I established that all permeation measurements are reliably measuring the intrinsic properties of the ZIF-8 membranes with negligible effects of support and external mass transfer resistances (see Supporting Information for details). At the end of 120 min of growth under continuous flow (arrest point #1), a dual-layer film is observed on the inner surface of the hollow fiber (Figure 18a, and a more magnified version in Figure 19 in Supporting Information) with an overall thickness of ~7 μm (Table 6), of which ~4.5 μm is a dense ZIF-8 layer and the remainder is a discontinuous layer composed of plate-like structures. This morphology can be understood as arising from the rapid penetration of 2-mIm (which is soluble in both water and octanol) into the octanol phase. At the inner surface of the fiber, 2-mIm is rapidly consumed by reaction with $Zn^{2+}$ to form a dense ZIF-8 layer. However, the formation of this initial dense layer then acts as a barrier that restricts the availabilty of 2-mIm species further into the octanol phase, thereby leading to the diffusion-limited formation of a second discontinuous film morphology on top of the dense layer (as depicted schematically in Figures 20(a)-20(b)). Since this effect is difficult to observe directly inside the hollow fiber, I performed a similar experiment by contacting the two phases in a transparent glass vial (Figure 20(e)). One can clearly observe the formation of a dense film at the water-octanol interface, and additionally a cloudy layer with sparse crystallization further into the octanol phase. Furthermore, the dense layer also has nanoscopic defects which lead to high permeances of both propylene and propane and a low propylene selectivity (~3). The initial continuous growth step therefore does not yield a viable membrane, and further processing is needed. After a subsequent 210-min static growth step (arrest point #2)

during which there was no continuous replenishment of the limiting reactant $Zn^{2+}$, a ~10 μm ZIF-8 layer was observed (Table 6). Clearly the overall film growth rate in the static period is much lower than in the initial continuous flow step due to low availability of $Zn^{2+}$ as well as slow diffusion of 2-mIm through defects in the dense layer. Importantly, Figure 19b reveals that the previous dual-layer morphology is replaced with essentially a single dense layer. During the static growth period, the discontinuous layer is gradually densified by slow addition of crystallized material as depicted in Figure 20c. Table 7 shows a sharp drop in propane permeance and increase in selectivity to ~14 during this period, clearly indicating that nanoscopic defects are being filled in with ZIF-8 material and that the static growth step is crucial for defect control. Finally, the process is completed with a 20-min replenishment step followed by another static growth period (arrest point #3). Figure 19c, Figure 20d, Table 6, and Table 7 show a single continuous layer (albeit with some visible defects), as well as further increases in film thickness (~12 μm) and selectivity (~17) with a propylene permeance of ~23 gas permeation units (GPU, 1 GPU = $3.348\times10^{-10}$ mol $m^{-2}$ $s^{-1}$ $Pa^{-1}$).

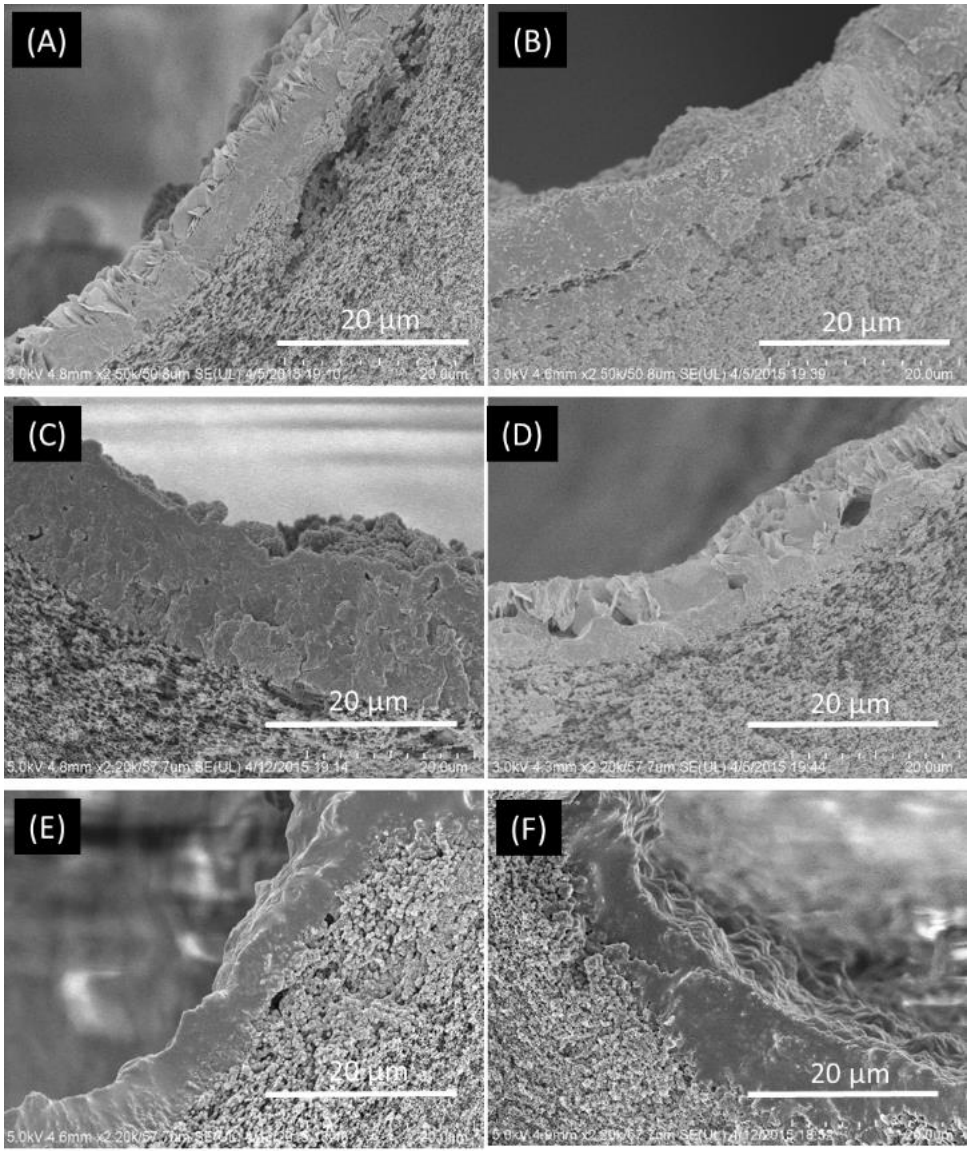


**Figure 18.** Cross-sectional SEM images of ZIF-8/hollow fiber membranes after: (a) 2 hr of continuous membrane growth (Step 1), (b) 3.5 hr of static membrane growth (Step 2), and (c) 20 min of metal solution replenishment followed by a final 3.5 hr of static growth (Step 3); and the membranes obtained from a similar experiment with a modified temperature profile: (d) Step 1, (e) Step 2, and (f) Step 3.

**Table 6.** The average thickness of ZIF-8 membranes along the entire fiber measured at each growth arrest point (#1: 2 hr of continuous membrane growth step, #2: 3.5 hr of static membrane growth, #3: 20 min of metal solution replenish step followed by final 3.5 hr of static growth).

| **Processing** | **Arrest point #1** | | **#2** | | **#3** | |
|---|---|---|---|---|---|---|
| **Method** | **Dense** | **Discontinuous** | **Dense** | **Discontinuous** | **Dense** | **Discontinuous** |
| Isothermal | 4.5±0.5 | 2.7±0.4 | 10.2±2.1 | N/A | 12.3±1.6 | N/A |
| Initial Heating | 2.5±0.6 | 3.2±0.9 | 7.0±1.2 | N/A | 8.0±2.3 | N/A |

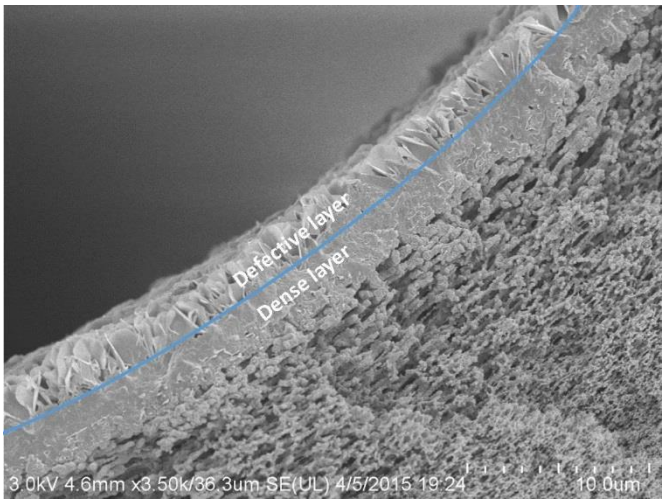


**Figure 19.** Magnified SEM image of dense and defective membrane layers after 120 min of continuous growth at isothermal conditions.

**Table 7.** Gas permeation properties of ZIF-8 membranes at each arrest point, for an binary $C_3H_6/C_3H_8$ equimolar feed mixture. The arrest points are the same as those described in the caption of Table 1.

| **Isothermal** | | | | **Initial Heating** | | | |
|---|---|---|---|---|---|---|---|
| [GPU] | #1 | #2 | #3 | [GPU] | #1 | #2 | #3 |
| $C_3H_6$ | 31 | 26 | 23 | $C_3H_6$ | 45 | 30 | 33 |
| $C_3H_8$ | 11 | 1.8 | 1.3 | $C_3H_8$ | 14 | 2.5 | 1.9 |
| $C_3H_6/C_3H_8$ | 2.8 | 14.3 | 17.7 | $C_3H_6/C_3H_8$ | 3.2 | 12 | 17.5 |

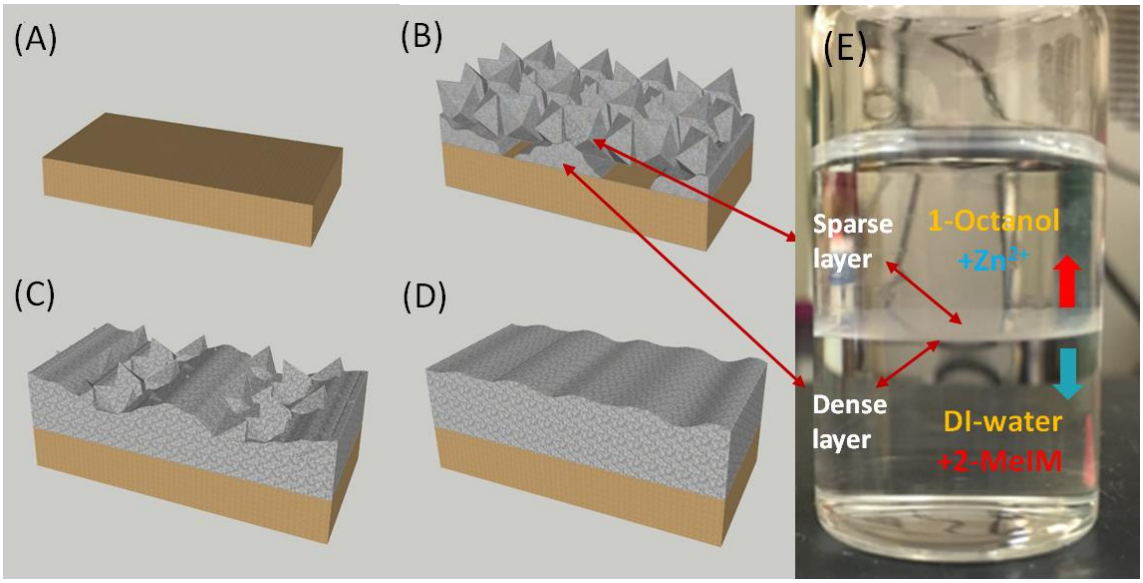


**Figure 20.** Schematic of the ZIF-8 membrane growth mechanism on Torlon® hollow fibers: (a) 0 hr and (b) 2 hr of continuous membrane growth (Step 1), (c) after 3.5 hr of static membrane growth (Step 2), and (d) after 20 min of metal solution replenishment followed by a final 3.5 hr of static growth (Step 3); and (e) photograph of metal ($Zn^{2+}$) and linker (2-MeIM) solution after 15 min of interfacial contact in a glass vial.

### 3.3.2. IMMP Modifications

Based upon these mechanistic findings, I hypothesized that increasing the rates of initial ZIF-8 crystal nucleation and formation of the initial dense barrier layer would significantly reduce its thickness (or crystal grain size) during the initial continuous flow step, since a more rapidly formed barrier layer would effectively inhibit further reaction-limited dense film growth. This would have the effect of a reduced overall membrane thickness and hence a higher permeance. To increase the rate of formation of the initial dense layer, I modified the temperature profile by heating the IMMP module from 22°C to 40°C (Figure 17b) over the first 30 mins of synthesis, followed by a downward temperature ramp and stabilization at the same isothermal conditions as previously for the remainder of the membrane fabrication process. Figures 18d-18f, Table 6, and Table 7 clearly support the validity of this hypothesis. A considerably thinner (~2.5 μm) dense

layer is formed initially, leading to a final membrane thickness of ~8 μm with a correspondingly higher propylene permeance (33 GPU) and no loss of selectivity over the isothermal case. Next, I considered the role of the support hollow fibers in determining the defect density and selectivity of the membrane. It has been recently shown that the porosity and microstructure of ceramic supports exerts a significant influence on the quality of ZIF-8 membranes.[66] The PAI hollow fibers initially used in this work were identical to those fabricated and used by us in previous works.[9] These fibers have OD 300 μm and ID 200 μm. In addition, the inner surface roughness of these fibers was measured with scanning probe microscopy. The RMS roughness was obtained as 63 ± 5 nm, which is much smaller than the membrane thickness and is not expected to lead to large heterogeneities in the film thickness. I also characterized the porosity of the fiber from SEM images using the Khare and Burris method.[117] For this purpose (Figures 21a-21b), binary images were obtained from cross-sectional SEM images of the support *via* the image analysis program ImageJ.[118] The porosity (ε) and average pore size of the fibers were estimated at 44% and 290 nm, respectively. The fibers are also highly permeable, as characterized by their $N_2$ permeance of 54000 GPU and permeability of $2.7\times10^6$ Barrer (1 Barrer = 1 GPU. μm) at 25°C. I hypothesized that fibers with larger porosity and somewhat larger pore size would allow faster formation of a thin membrane layer and better anchoring of this layer to the fiber surface. To this end, I modified the PAI spinning conditions as follows. A NMP/DI-water mixture (with NMP being a solvent and DI-water being a non-solvent) is used as a bore fluid solution during the fiber spinning. In order to obtain fibers of higher porosity, I increased the solvent (NMP) content from 80 wt% to 85 wt%. The resulting fibers had an RMS roughness of 62±6 nm which is similar to the

previous fibers. However, the porosity and average pore size of the new fibers were considerably larger at 55% and 480 nm, respectively. (Figures 21(c)-21(d)).

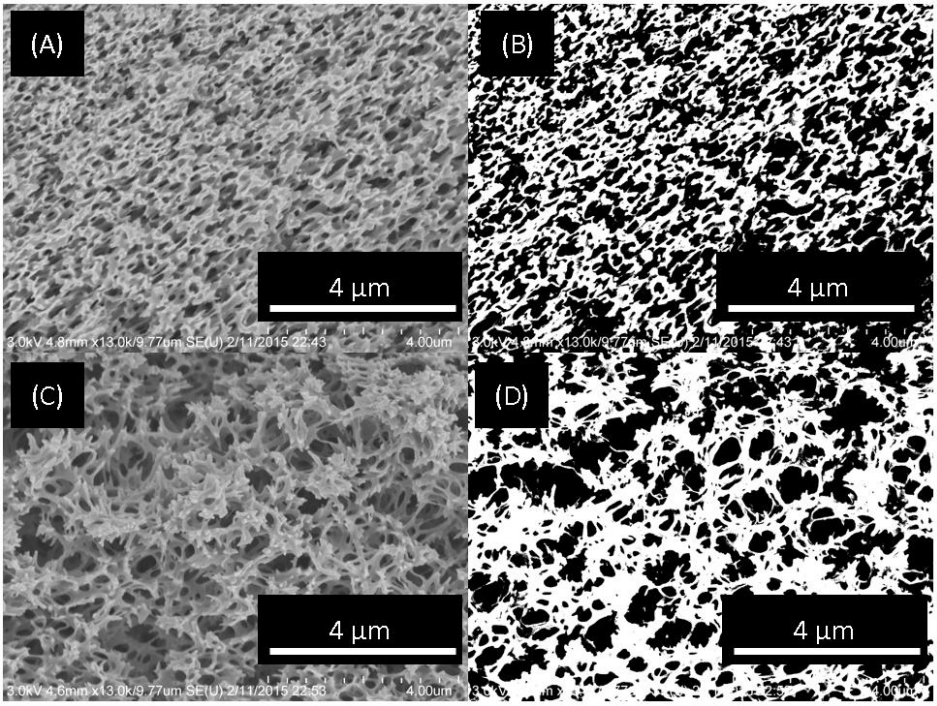


**Figure 21.** Cross-sectional SEM images of (a) Torlon® fiber, and (c) modified Torlon® fiber. (b), and (d) are associated binary images for porosity estimation.

To investigate the effect of the support fibers in conjunction with the modified growth technique (developed earlier in this report), I then prepared ZIF-8 membranes in three different ways. Case 1 is identical to the previously reported ZIF-8 membrane using the previous PAI fiber support and the original (isothermal) IMMP technique[9], Case 2 uses the new PAI fibers prepared using the modified spinning technique but with the original IMMP method for membrane growth, and Case 3 uses both the new PAI fibers and the modified (non-isothermal) IMMP technique. Further details of the membrane growth procedures are in the experimental section. Figure 22 shows cross-sectional SEM images of the final ZIF-8 membranes obtained in each case. Uniform ZIF-8 layers were observed for all cases. Detailed measurements of membrane thickness at different axial locations

along the 5 cm length of the hollow fiber for all cases are shown in Figure 23. Notably, the membrane thickness in Case 3 (5 ± 1 μm) is much lower than for Case 1 and Case 2 (10 ± 2 μm, and 9 ± 2 μm, respectively) indicating that the non-isothermal IMMP remains effective in reducing the membrane thickness on the new PAI support as well. To compare the performance of these membranes, equimolar $C_3H_6/C_3H_8$ mixed-gas permeation data were collected using a steady-state Wicke-Kallenbach technique at 25°C with the IMMP module directly acting as a permeation module (Table 8). Case 3 membranes show much higher $C_3H_6$ permeance than Cases 1 and 2, due to the much lower thickness. Additionally, Case 3 membranes also show much higher $C_3H_6/C_3H_8$ selectivity due to a significant drop in the $C_3H_8$ permeance. This clearly indicates the mitigation of membrane defects due to better anchoring of the ZIF-8 layer on the more porous fiber support. The microstructural changes were investigated in more detail with helium permporosimetry.[119] The helium flux was measured under dry conditions and then after wetting with Fluorinert (FC-40) liquid that has a low surface tension. Helium permeance is measured as a function of pressure in the feed gas. Under wetted conditions, membranes that have mesopore defects such as pinholes or cracks would show a sudden increment in helium permeance at a pressure that is sufficient to displace the wetting liquid from the mesopore defects. The defect size can then be estimated by the Cantor equation.[120] However, such phenomena are not observed in the pressure range 0-90 psi in all the Case 1-3 ZIF-8 membranes (Figure 24), clearly showing that continuous membrane layers are formed over the entire fiber with no large defects (> 20 nm in size, corresponding to the maximum pressure of 90 psi used in the measurements). However, the dry helium permeabilities (Figure 24) also allow the qualitative characterization of

nanoscopic (< 20 nm) defects. The ideal range of helium permeability from a defect-free ZIF-8 membrane is represented by the shaded area in Figure 24, which is obtained using the range of corrected diffusivity and adsorption isotherm parameters for helium in ZIF-8 as given by Zhang et al.[121] Case 1 ZIF-8 membranes display significantly higher dry helium permeability outside the ideal region, clearly indicating the presence of nanoscopic defects. However, the dry helium permeability progressively declines and reaches the ideal region in Case 2 and Case 3 membranes, clearly indicating that simultaneous reductions in both membrane thickness and defect density have successfully occurred. Case 3 has the lowest dry helium permeability, corresponding to the most defect-free membranes which also have the best separation performance as shown in Table 8.

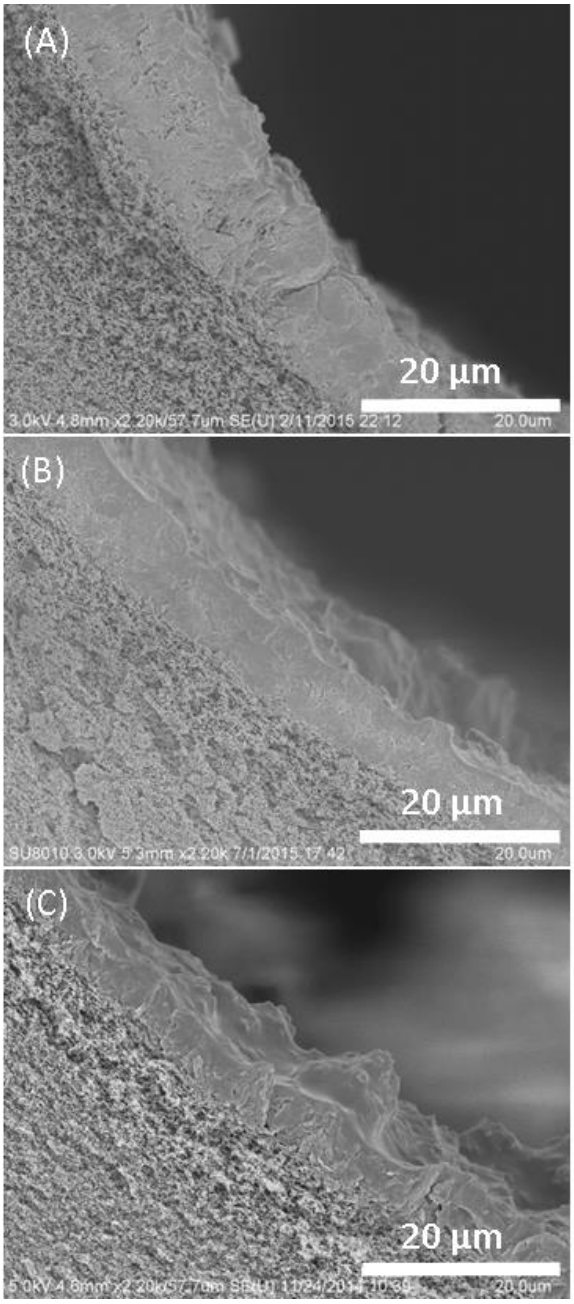


**Figure 22.** Cross-section SEM images of ZIF-8 membranes grown under **(a)** Case 1, **(b)** Case 2, and **(c)** Case 3 conditions.

**Table 8.** ZIF-8 membrane permeances from a $C_3H_6/C_3H_8$ equimolar mixed gas feed at 25°C processing with (modified) IMMP and with (modified) Torlon® fiber substrate.

| Case # | $C_3H_6$ Permeance [GPU] | $C_3H_8$ Permeance [GPU] | $C_3H_6/C_3H_8$ Binary Selectivity |
|---|---|---|---|
| 1 | 27 ± 4 | 3 ± 1 | 9 ± 1 |
| 2 | 34 ± 4 | 1.4 ± 0.3 | 24 ± 3 |
| 3 | 66 ± 3 | 1.0 ± 0.1 | 65 ± 5 |

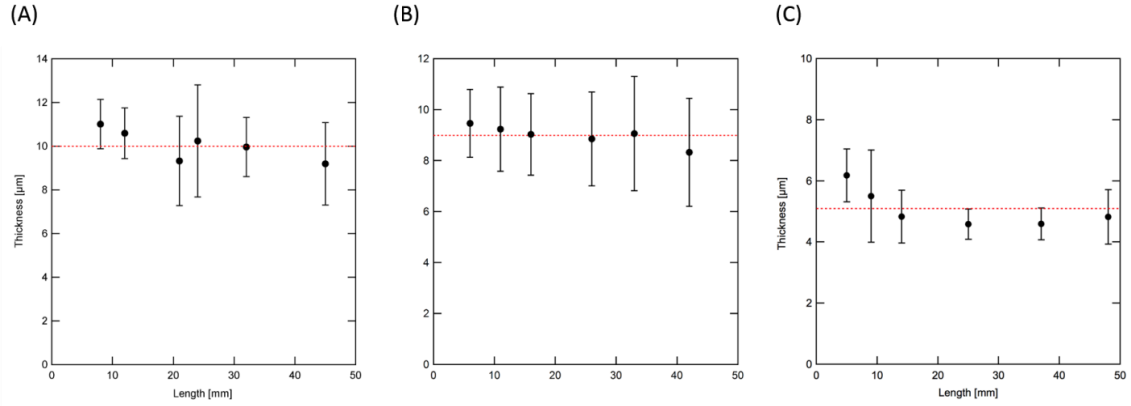


**Figure 23.** ZIF-8 layer thickness measured from SEM cross-sections obtained along the 5 cm length of membranes made with (a) isothermal IMMP, (b) modified hollow fiber, and (c) non-isothermal IMMP plus modified hollow fiber. Thickness at each location was measured from five randomly chosen points along the fiber circumference. Dotted lines indicate average thickness of each membrane, 10.0±1.8 µm, 9.1±1.7 µm, and 5.0±1.0 µm, respectively.

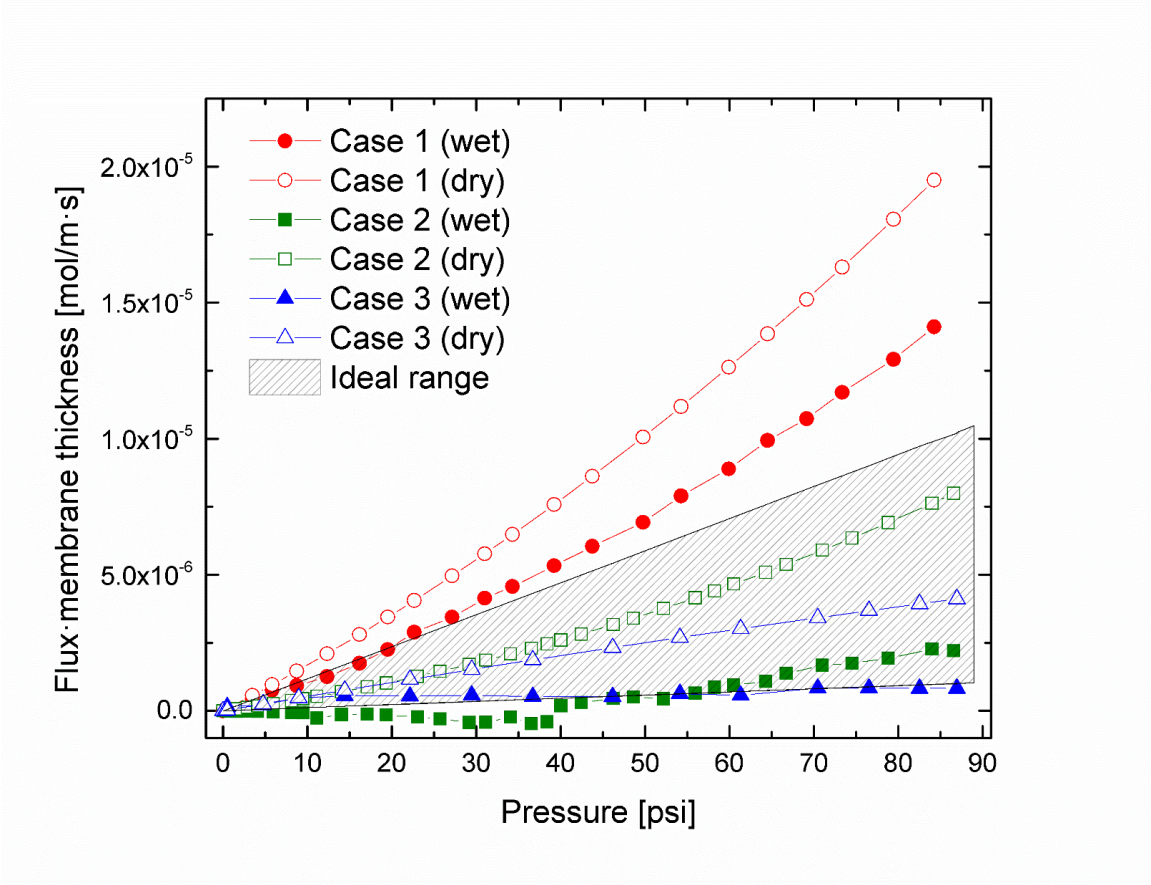


**Figure 24.** Helium permeabilities (expressed as flux × membrane thickness) in Cases 1-3 of ZIF-8 inner surface membranes as measured at room temperature under dry and wetted conditions. The ideal range of helium permeability was calculated from corrected diffusivity and adsorption data (see text for details).[5]

### 3.3.3. Separation Properties

Finally, I characterized the binary and ternary mixture separation properties of Case 3 ZIF-8 membranes in more detail as a function of temperature (25-120°C). Figure 25a shows equimolar binary $H_2/C_3H_8$ and $C_3H_6/C_3H_8$ mixture permeation properties. Clear molecular sieving effects are observed, with $H_2/C_3H_8$ and $C_3H_6/C_3H_8$ separation factors as high as 2000±200 at 70°C and 65±5 at 25°C respectively. This performance is much improved from the previously reported ZIF-8 hollow fiber membranes made by IMMP

[5] This work was done in collaboration with Dr. Ramesh R. Bhave from Oakridge National Lab.

(370±60 at 120°C and 12±3 at 25°C respectively)[9] and is also comparable to the characteristics of ZIF-8 membranes reported in the literature using multistep/seeded growth techniques on disk-type or tubular ceramic supports (Table 1). The data also shows the strong temperature dependence of the $C_3H_6$ permeance and the resulting moderate decrease in separation factor as temperature increases. However, the ZIF-8 membranes still achieve a $C_3H_6/C_3H_8$ separation factor of 31±1 even at 120°C. Figure 25b shows the equimolar ternary ($H_2/C_3H_6/C_3H_8$) mixture separation properties. This feed mixture simulates the composition of the exit stream from near-equilibrium propane dehydrogenation (PDH) reactors that are used for propylene production. The present ZIF-8 membranes continue to effectively separate $C_3H_6$ from $C_3H_8$ in the presence of $H_2$ with separation factor of 53±3 at 25°C. It is also noted that these membranes can be utilized to separate $H_2$ from $C_3H_6$ ($H_2/C_3H_6$ separation factor of 99 ± 3 at 120°C, which is industrially attractive.[2] The performance of ZIF-8 membranes at higher feed pressures is also an important issue that has only recently been examined in the literature. Initial reports suggest that ceramic-supported ZIF-8 membranes may exhibit drastic decreases in $C_3H_6/C_3H_8$ selectivity at feed pressures of 4 bar, an effect that was attributed to the opening of nanoscopic defects at higher pressures.[67] While not the main focus of the present work, I mention here that high-performance ZIF-8 membranes fabricated *via* non-isothermal IMMP using modified fiber supports (Case 3) have also been examined for binary $C_3H_6/C_3H_8$ separation performance at feed pressures up to 6 bar at 25°C. The selectivity remains high and shows only minor (13-15%) reduction at 6 bar. The $C_3H_6$ permeance shows a reduction of about 25%, which is expected in molecular sieve materials due to pore saturation effects. However, it is important to note that the actual

$C_3H_6$ flux (throughput) at 6 bar is 3.75-4 times higher than at 1 bar, due to the much greater pressure driving force. These initial data suggest that ZIF-8 membranes fabricated by IMMP in PAI hollow fibers have greater resistance to opening of defects caused by mechnical stress at higher pressures. my findings regarding higher-pressure operation of ZIF-8 membranes will be discussed in detail in a forthcoming section.

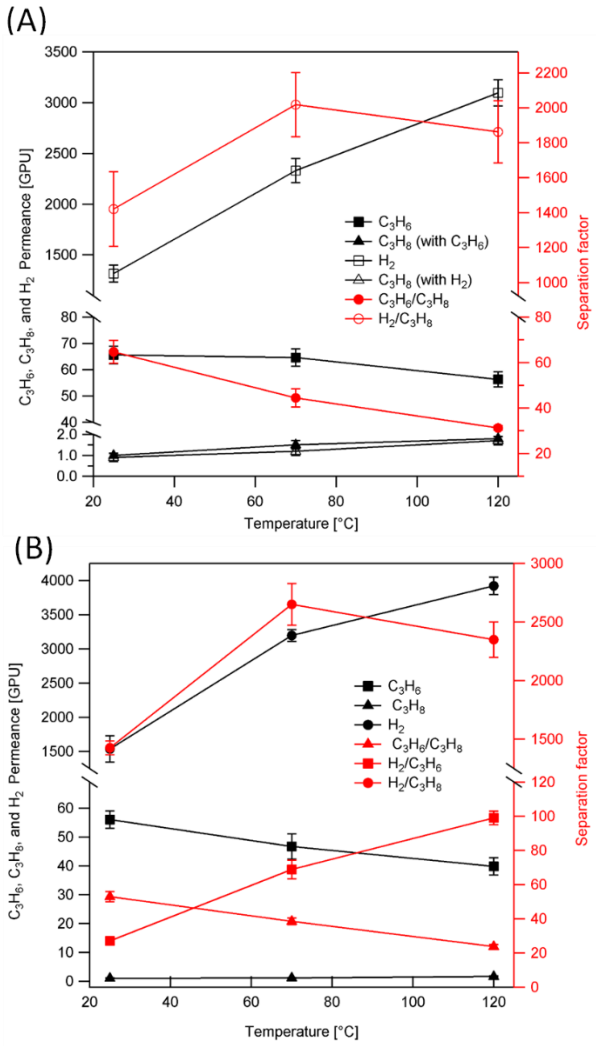


**Figure 25.** Gas permeation properties of Case 3 ZIF-8/hollow fiber membranes in (a) binary equimolar $C_3H_6/C_3H_8$ and $H_2/C_3H_8$ separations, and (b) ternary equimolar $H_2/C_3H_6/C_3H_8$ gas separation. Error bars are obtained from three independently synthesized membrane samples, all made from the same batch of hollow fibers.

### 3.4. Conclusion

The mechanistic findings and resulting significant improvements in membrane performance allow one to envisage a two stage separation of ternary $H_2/C_3H_6/C_3H_8$ mixtures, *i.e*. a first ZIF-8 membrane stage of small total area that takes advantage of the very high $H_2$ permeance to separate it from $C_3H_6$ and $C_3H_8$, followed by a second ZIF-8 membrane stage of larger area that separates $C_3H_6$ from $C_3H_8$. This is made possible by two new developments, firstly the modification of the IMMP technique to include an initial non-isothermal growth step and secondly the engineering of a new hollow fiber PAI support with enhanced surface properties. Additionally, the low cost and benign IMMP route, free of other intermediate or post-synthesis steps, creates a real possibility for scalable fabrication of high-performance ZIF-8 membranes.

# CHAPTER 4.

# ZIF-8 MEMBRANE VIA INTERFACIAL MICROFLUIDIC PROCESSING IN POLYMERIC HOLLOW FIBERS: EFFICIENT PROPYLENE SEPARATION AT ELEVATED PRESSURE

## 4.1. Introduction

Zeolitic imidazolate frameworks (ZIFs) are a class of nanoporous metal organic frameworks (MOFs) consisting of imidazolate linker moleculess coordinated to metal (usually Zn) ions.[16] Due to their range of pore sizes and good thermal and chemical stability, ZIFs are attractive as materials for energy-efficient separation of gas or liquid mixtures.[22,112] Considerable work has appeared in the literature on ZIF membranes, particularly ZIF-8 and its promising performance for $H_2/C_3H_8$ and $C_3H_6/C_3H_8$ separations.[37,65,122-124] Although ZIF-8 has a nominal crystallographic pore size of 0.34 nm, the dynamic flexibility of the crystal structure leads to an effective pore aperture size in the range of 0.40 nm to 0.42nm. This important property allows ZIF-8 to separate $C_3H_6$ from $C_3H_8$ by virtue of diffusivity differences, thereby suggesting a membrane-based route to perform this important industrial olefin/paraffin separation process. A key issue impeding the fabrication of industrially attractive ZIF membranes is the lack of a scalable and inexpensive membrane fabrication process. Several reports have introduced synthesis methods for ZIF-8 membranes.[18,27,42,125] However, the synthesis of high-performance ZIF-8 membranes required several types of intermediate steps (such as modification of the support and growth of intermediate ZnO layers to promote the nucleation of the ZIF-8

thin film), or post-synthesis treatment steps. Furthermore, operation at higher pressures (in the range of 6-10 bars) is an important criterion for $C_3H_6/C_3H_8$ separations. ZIF-8 membranes reported so far lose their selectivity at higher pressure, and this occurrence is thought to be due to the opening of defects in the membrane layer when subjected to higher pressures. For example, Jerry Lin *et al* reported a decrease of $C_3H_6/C_3H_8$ separation factor from 30 at 1 bar feed pressure to 27 at 4.5 bar.[63]

Our group have reported the fabrication of ZIF-8 membranes on the inner surface of polyamide-imide (PAI) hollow fiber supports by a technique that I refer to as interfacial microfluidic membrane processing (IMMP).[9,46] IMMP has the advantage of being an *in situ* technique that can be scaled up to larger hollow fiber membrane modules. Furthermore, I have shown that ZIF-8 membranes of high quality can be fabricated by mechanistic understanding and control of the processing parameters (reactant flow profiles, concentrations, temperature profiles) as well as the microstructures of the PAI hollow fiber supports, without any need for support modification or other intermediate/post-synthesis treatment steps. In this work, I report two new findings of importance in the development of ZIF-8 membranes for olefin separations: (1) the synthesis and detailed characterization of defect-free ZIF-8/hollow fiber membranes with $C_3H_6/C_3H_8$ separation factor of ~180 at 1 bar, which is essentially equal to the ideal value of ~182 based upon the product of adsorption selectivity (1.3) and diffusion selectivity (140)[121]; and (2) maintenance of a high selectivity at elevated pressures (up to 9.5 bar) and in long-term operation (over one month of testing). The separation data reported in this work are average values recorded from three membrane samples synthesized independently, and are found to be highly reproducible.

## 4.2. Experimental Methods

### 4.2.1. Materials

For membrane module fabrication and IMMP, translucent epoxy (DP-100) was purchased from 3M and PDMS (Corning Sylgard 184) was obtained from Ellsworth Adhesives. 1-Octanol was obtained from Acros Organics and Deionized water (DI-water) was produced with Thermo Scientific 7128. $Zn(NO_3)_2 \cdot 6H_2O$ (99%), poly-vinylpyrrolidone (PVP) (MW 1,300,000), and 2-Methylimidazole (99%) were obtained from Sigma Aldrich. For fabrication of the hollow fiber membrane supports, Torlon® 4000T was obtained from Solvay Advanced Polymers and lithium nitrate was obtained from Sigma Aldrich. Both methanol and hexane (>99 %) were purchased from VWR and used as received.

### 4.2.2. IMMP Modules

Detailed descriptions and photographs are presented in chapter 3.2.2.[9,46] The IMMP module is made of SS 304 and has a volume of 70 mL. Fittings for mounting of hollow fibers are provided as described in my previous work. A 4" length of Torlon fiber substrate was inserted horizontally through diametrically opposite holes in the module. A small drop of 3M translucent epoxy was then applied to the outer (shell) side of each fiber at the ends in order to achieve sealing. After allowing the epoxy to cure for at least 90 min, the excess fiber ends were removed with tweezers. Helium (He) permeance of the mounted fiber was then measured to ensure that the fiber was properly sealed by the epoxy and that the inner (bore) side had not been crushed or blocked.

### 4.2.3. Synthesis of ZIF-8 Membrane

Three membrane fabrication methods were used (referred to as Cases 1-3 in the following discussion). *Cases 1 and 2:* 10 mL of neat 1-octanol was first introduced through the bore side of the fiber using a syringe pump at 2 ml/min. 9 g of 2-MeIM and 0.22 g of zinc nitrate hexahydrate were dissolved in 80 mL DI-water and 40 mL 1-octanol, to generate solutions with 2-MeIM and $Zn^{2+}$ concentrations of 1.37 mol/L and 0.018 mol/L respectively. 3 mL of $Zn(NO_3)_2 \cdot 6H_2O$/1-octanol solution was introduced through the bore side of the fiber using the syringe pump at 0.6 ml/hr. Then 2-MeIM/DI-water solution was slowly poured into the module while stirring the solution at 60 rpm. The continuous membrane growth step was begun at 22°C and with a linear increase in temperature to 42°C over 25 min followed by a decrease to 30°C over 60 min and steady holding at the latter temperature. The syringe pump was stopped for 210 min after 120 min of the continuous membrane growth step. The syringe pump was turned on again for 20 min followed by another 210 min of static growth step. Pump flow rate was changed to 2 ml/min and 10 mL of neat 1-octanol was introduced through the bore side of the fiber while the 2-MeIM/DI-water solution was replaced with fresh DI-water three times to quench the reaction and remove excessive ZIF precursors. 20 mL of MeOH was introduced into the bore side of the fiber and the shell solution was replaced with MeOH. The membrane was dried at room temperature for 2 days. *Case 3:* Membranes were prepared with the same synthesis procedure of Case 1 and 2 membranes, except for a different 2-MeIM concentration in the shell side solution (4.5 g of 2-MeIM in 80 ml DI-water, corresponding to a concentration of 0.69 mol/L).

### 4.2.4. End Sealing of Membranes

To complete the membrane fabrication process, PDMS sealing was performed on both ends of the fibers to prevent the 'lumen bypass' effect.[9,113] A 9 wt% PDMS (Sylgard 184)/heptane solution was heated at 90 °C under vigorous stirring for 4 hr to thermally crosslink the PDMS. After cooling to 25°C, a 2 μL PDMS droplet was applied to the end of the mounted module using capillary action. Argon (Ar) gas was immediately flowed through the fiber bore upon addition of the PDMS/heptane solution followed by curing at 120°C for 2 hr.

### 4.2.5. Fabrication of Torlon Hollow Fiber Supports

For Case 1, the PAI hollow fibers were fabricated by a spinning process as described in detail in my previous work.[46] For Case 2, PAI hollow fibers were fabricated with a modified spinning process. Detailed spinning condition can be found in Table 9.

**Table 9.** Baseline (Case 1) and modified (Case 2) spinning conditions of PAI Torlon® hollow fiber porous supports. Case 3 ZIF-8 membranes utilize the same hollow fibers as Case 2.

| | **Case 1** | **Case 2** |
|---|---|---|
| **Dope composition<br>Case1: (PAI/NMP/EtOH/$LiNO_3$) (wt %)<br>Case2: (PAI/NMP/$H_2O$/PVP) (wt %)** | 15/66/4/15 | 25/63/5/7 |
| **Dope flow rate (ml/hr)** | 300 | 360 |
| **Bore fluid (NMP/$H_2O$) (wt %)** | 85/15 | 80/20 |
| **Bore fluid flow rate (ml/hr)** | 100 | 200 |
| **Air gap (cm)** | 15 | 0.5 |
| **Take up rate (m/min)** | 40 | 40 |
| **Operating temperature (°C)** | 27 | 50 |
| **Quench bath temperature (°C)** | 25 | 55 |

### 4.2.6. Characterization

XRD patterns were measured on a PANalytical X'Pert Pro diffractometer at room temperature using CuKα radiation and a scanning range of 5-40° 2θ. Cross-sectional images of ZIF-8 membranes were collected with a Hitachi SU 8010 scanning electron microscope after a thin layer of gold was sputtered onto the cross-sectional surface. The samples were soaked with a hexane solution for 30 min followed by dipping into liquid nitrogen for a clean cut. The membrane thickness was obtained by averaging thickness measurements made at different cross-sections along the 5 cm fiber length. All permeation measurements were performed by the time-lag or the Wicke-Kallenbach technique.[9,76] In the time-lag technique, both the feed and permeate side were maintained under vacuum. Then, gas is fed into the IMMP module at a constant pressure and temperature. The feed flow rate was set to 10 SCCM by a carefully calibrated MFC (Aalborg, GFC17S) and injected to the bore. The pressure increase on the permeate side (equivalent to the number of permeated gas molecules) was recorded over time using a pressure transducer (Omega). In the Wicke-Kallenbach technique (Figure 26), Ar was used as the sweep gas at the permeate side and pressure was maintained at 1 bar during the experiment. The permeate stream was analyzed by online gas chromatography (Shimadzu GC-2014) after calibration. For binary mixture permeation measurements, gases were well mixed at a mixer before entering the feed side of the module. The pressure of the feed gas is adjusted using a back-pressure regulator (Cole Parmer, 0-300 psi range). The temperature of the module was controlled by placing it in a convection oven (Cole Parmer). The reported permeances and selectivities are average values recorded from three membrane samples synthesized independently. The error bars

associated with each permeation data point represent the standard deviations of the measurements from the three independently fabricated samples.

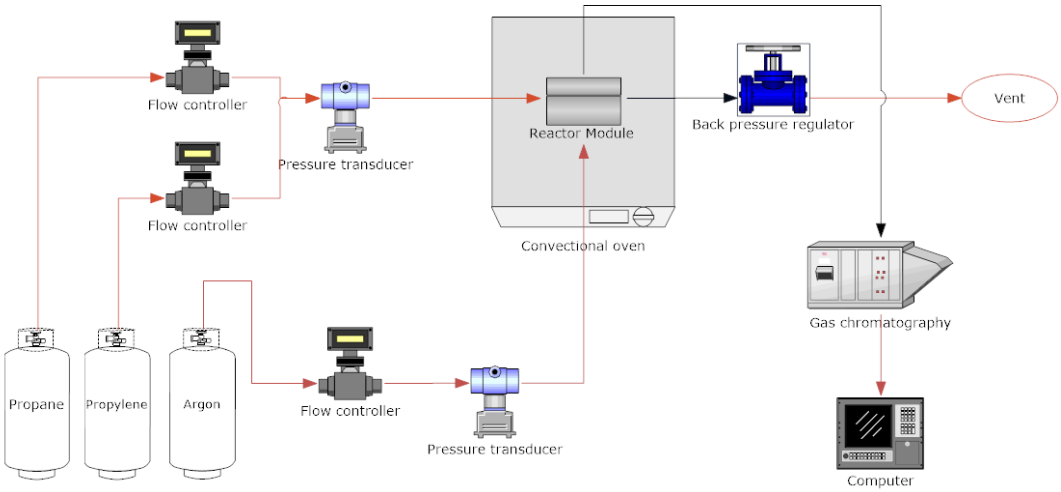


**Figure 26.** Schematic of mixed-gas permeation measurement system operated in Wicke-Kallenbach mode.

### 4.3. Results and discussion

#### 4.3.1. IMMP Optimization

We first reported the fabrication of ZIF-8 membranes by the IMMP technique with $H_2/C_3H_8$ selectivity ~400 and $C_3H_6/C_3H_8$ selectivity ~10.[9] In a more recent work, I studied the IMMP mechanism in more detail.[46] Based upon mechanistic understanding of the ZIF-8 membrane growth inside the PAI hollow fiber, I developed higher-performance membranes ($C_3H_6/C_3H_8$ selectivity ~70 at 1 atm feed pressure) *via* use of an initial non-isothermal growth step and PAI hollow fiber supports with larger pore size. In the present paper, the Case 1 membrane synthesis is identical to that described in my recent work, and is treated as a baseline. This synthesis includes the initial non-isothermal growth step, and PAI hollow fibers with $N_2$ permeance of 54,000 GPU (1 Gas Permeation Unit =

$3.348\times10^{-10}$ mol.m$^{-2}$.s$^{-1}$.Pa$^{-1}$) at room temperature. However, the microstructure of these hollow fibers showed some densification of the pore structure (Skin layer) near the shell surface. (Figure 27a) In the present work, I hypothesized that PAI hollow fibers with more open pore structure at the membrane growth interface would lead to higher permeability, thereby allowing the formation of a more defect-free membrane layer by minimizing reactant transport limitations and interfacial inhomogeneities. It has been achived by utilizing PVP as a pore forming agent. PVP can boost the permeability of support by increasing the external pore density without affecting the pore size and its distribution.[126] We also successfully reduce the dense skin layer by by optimizing fiber spinning condition especially air gap, quench bath temperature, and bore fluid composition (Figure 27b).[6] we can achieve higher permeability by reducing the presence of skin layer. Finally, elevated quench bath temperature boost a solvent exchange rate result in the uniform pore structure by supressing the micro void area of the torlon fiber. The resulting fibers had a much higher $N_2$ permeance of 77000 GPU.

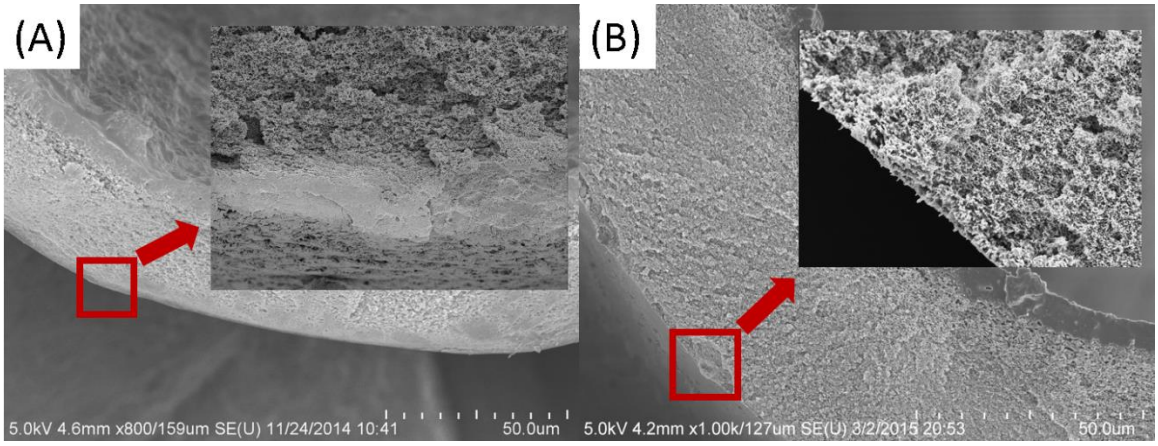


**Figure 27.** Cross-sectional SEM images of (a) Case 1 PAI fiber with skin layer, and (b) Case 2 PAI fiber showing suppression of the densified pore structure at the shell side.

[6] This work was done in collaboration with Dr. Ali Rownaghi from Missouri University of Science and Technology.

Figure 28a shows an example of the Case 2 ZIF-8 membrane grown by the same IMMP method as Case 1 (Experimental Section), but using the high-permeability PAI hollow fibers as supports.[9] Although a continuous ZIF-8 layer is formed at the bore surface of the fiber, we observe extensive overgrowth inside the bore of the fiber, leading to a defective membrane. This overgrowth is a result of the increased permeability of the fiber, and is caused by the fast penetration of 2-MeIM linkers into the bulk of the bore fluid, where they react with $Zn^{2+}$ ions to form the overgrowth crystals in addition to the ZIF-8 membrane layered formed by interfacial crystallization. To prevent this occurrence, I tuned the IMMP method by reducing the 2-MeIM concentration by half. Figures 28b-28c show the morphology of the resulting membrane (Case 3), which is uniform, of average thickness 8.1±1.6 μm along the fiber length (Figure 29), and exhibits no overgrowth of crystals on the membrane surface. The XRD pattern (Figure 28) confirms that a ZIF-8 membrane has been formed.

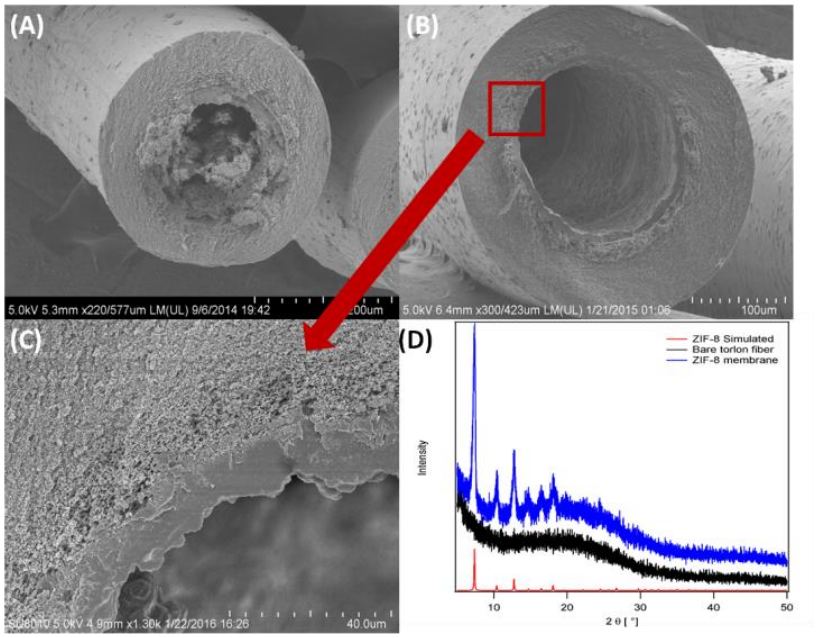


**Figure 28.** Cross sectional SEM images of (a) Case 2 ZIF-8 hollow fiber membrane showing crystal overgrowths inside the fiber bore; (b, c) Case 3 ZIF-8/hollow fiber membrane; and (d) XRD patterns of bare PAI membrane and Case 3 ZIF-8 membrane, with a simulated XRD pattern of ZIF-8 shown for comparison.

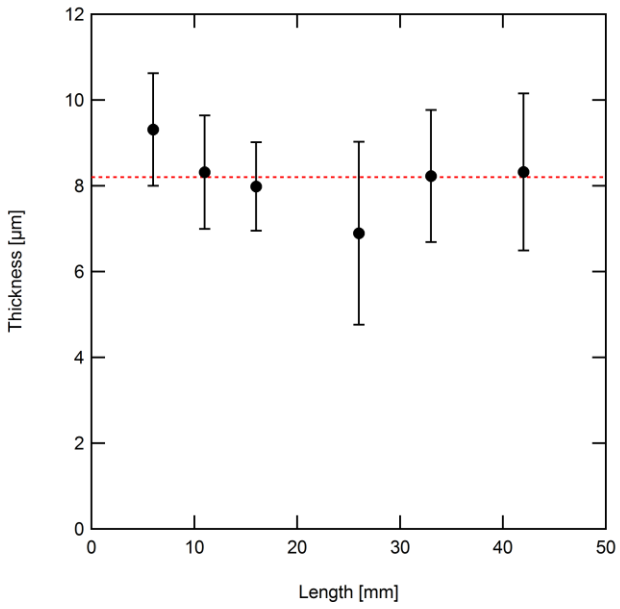


**Figure 29.** Case 3 ZIF-8 membrane thickness as measured from cross sections obtained at different locations along the 5 cm length of the hollow fiber. Each data point is obtained by averaging the thicknesses measured at multiple locations along the circumference. The average thickness over the entire fiber length, obtained by averaging all the data points shown, is indicated by the dashed red line.

### 4.3.2. Single Component Permeability of ZIF-8 Membranes

Figure 30 shows the single-component permeabilities of gases (at 25°C and transmembrane partial pressure differential of 1 atm) in the Case 3 ZIF-8 membrane as a function of kinetic diameter. The gas fluxes were measured by time-lag ($H_2$, $CO_2$, Ar, $O_2$, Kr, $N_2$, $CH_4$, Xe, and $SF_6$) or Wicke-Kallenbach ($C_2H_4$, $C_2H_6$, $C_3H_6$, $C_3H_8$, $C_4H_{10}$, and *i*-$C_4H_{10}$) techniques (Experimental Section). The permeabilities ae then obtained in the standard manner, dividing the flux by the transmembrane pressure difference of the gas of interest and then multiplying by the membrane thickness. The ZIF-8 membrane shows clear molecular sieving properties: the molecular permeability generally decreases with increase in kinetic diameter. In agreement with previous work, a large permeability drop was observed around the kinetic diameter of 4.2 Å which is therefore designated as the effective aperture size. This leads to a classification of the gas molecules into two groups. For the first group of molecules with kinetic diameters smaller than the effective aperture size ($H_2$, $CO_2$, Ar, $O_2$, Kr, $N_2$, $CH_4$, Xe, $C_2H_4$, $C_2H_6$, and $C_3H_6$), permeation in the ZIF-8 pores is not significantly constrained by steric hindrance and the ZIF-8 framework is not particularly size-selective. It is noted that the crystallographically derived aperture size of 3.4 Å is located between $CO_2$ and $N_2$; however, the single-component $CO_2/N_2$ selectively is only ~5. Hence, the "rigid pore aperture" assumption is not valid for ZIF-8, which can be considered as a "soft molecular sieve" material with a flexible framework in comparison to "hard molecular sieves" such as zeolites which show much smaller effects of framework flexibility on permeation selectivity.[127] The three light hydrocarbons $CH_4$, $C_2H_4$, and $C_2H_6$ show minor anomalies from the general trend (of decreasing permeation with increasing kinetic diameter), mainly due to the contribution of strong adsorption of

these hydrocarbons in ZIF-8. The gas permeability is a product of diffusivity and adsorption strength, the latter being considerably stronger for the above hydrocarbons than for the next smaller gas ($N_2$). For example, it is reported that the Henry constants of $C_2H_4$ and $N_2$ are 1.18 and 0.09 at 35°C.[121] For the second group of molecules with kinetic diameters larger than the effective aperture size ($C_3H_8$, $C_4H_{10}$, *i*-$C_4H_{10}$, and $SF_6$), the effect of size exclusion by the ZIF-8 framework is evident in the very low observed permeabilities (<2 Barrer). These permeances are mostly the result of small levels of defects remaining in the membrane. It is also noted that $C_3H_6$ and $C_3H_8$ have similar adsorption characteristics, confirming that the exceptionally high single-component $C_3H_6/C_3H_8$ selectivity (~130) is a result of molecular sieving, albeit by a flexible framework.[128]

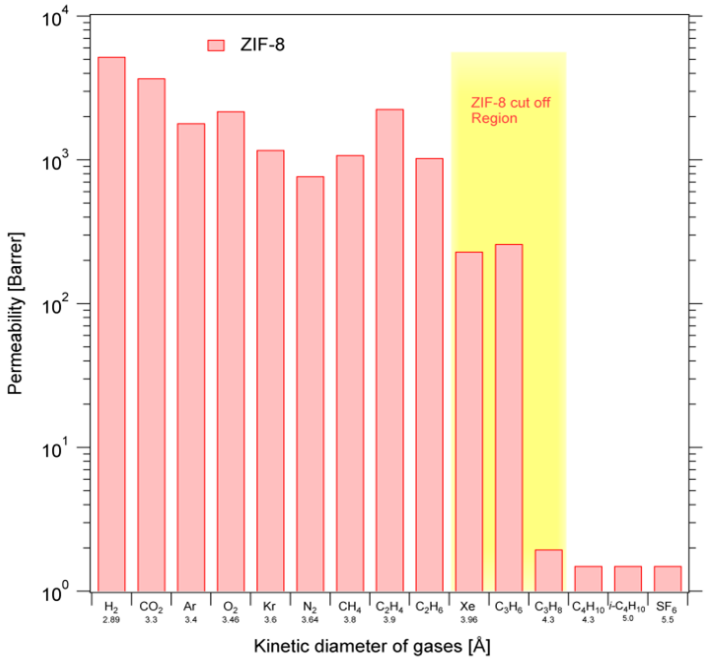


**Figure 30.** Unary gas permeabilities of Case 3 ZIF-8 hollow fiber membranes by the time-lag techniques at 25°C.

### 4.3.3. Binary and Tertiary Gas Mixture Separation Properties of ZIF-8 Membranes

Next, the equimolar binary mixture ($C_3H_6/C_3H_8$ and $H_2/C_3H_8$) separation properties of the ZIF-8 membranes were characterized as a function of temperature with the Wicke-Kallenbach technique at a feed pressure of 1 bar. Clear molecular sieving effects are observed, with $H_2/C_3H_8$ and $C_3H_6/C_3H_8$ separation factors as high as 3200±200 at 75°C and 180±5 at 25°C respectively (Figure 31). To the best of my knowledge, these are the highest selectivities reported thus far for ZIF-8 membranes. The permeance of $C_3H_6$ decreases with increasing temperature since it is mainly limited by adsorption strength, whereas the permeance of $C_3H_8$ increases slowly with temperature since it is limited by activated diffusion in the pore windows of ZIF-8. As a result the $C_3H_6/C_3H_8$ separation factor decreases with increasing temperature, but the ZIF-8 hollow fiber membranes still achieve a high $C_3H_6/C_3H_8$ separation factor of 60±3 even at 120°C. The $H_2$ and $C_3H_8$ permeances are both mainly limited by activated diffusion at lower temperatures, but adsorption effects begin to limit the $H_2$ permeance at higher temperatures. As a result, a maximum separation factor of 3300±175 is observed at 75°C. Figure 31 (b) shows the equimolar ternary ($H_2/C_3H_6/C_3H_8$) gas mixture separation properties. $C_3H_6/C_3H_8$ separation of 167±7 was obtained at 25 °C in the presence of $H_2$. The present ZIF-8 membrane also shows the $H_2/C_3H_6$ separation factor of 66±2 at 120°C demonstrating the possibility of two-stage separation of ternary $H_2/C_3H_6/C_3H_8$ that can be found from industrial product stream of propane dehydration (PDH) process, *i.e*. $H_2$ separation from $C_3H_6/C_3H_8$ mixture followed by $C_3H_6$ separation from $C_3H_8$.

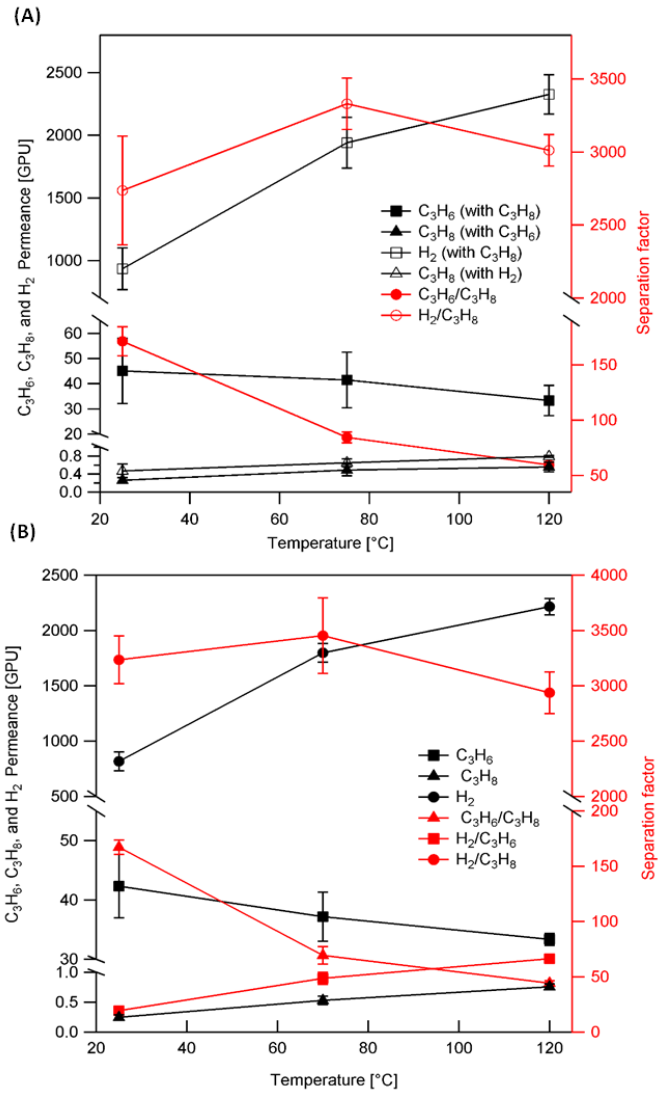


**Figure 31.** (a) Binary equimolar $C_3H_6/C_3H_8$ and $H_2/C_3H_8$, and (b) ternary equimolar $H_2/C_3H_6/C_3H_8$ gas mixture separation properties of ZIF-8 hollow fiber membranes as a function of temperature at a feed pressure of 1 bar.

### 4.3.4. Elevated Pressure Operability and Long Term Stability of ZIF-8 Membranes

We then examined the pressure dependence of the binary $C_3H_6/C_3H_8$ mixture separation properties of the ZIF-8 membranes, using feed pressures of 1–9.5 bar at a fixed temperature of 25°C. The Wicke-Kallenbach technique was used and the pressure of the permeate side was maintained at 1 bar. Once again, clear molecular sieving effects are

observed (Figures 32a-32b). As also reported in Figure 31, the $C_3H_6/C_3H_8$ separation factor is 180±5 at 1 bar feed pressure (*i.e.*, transmembrane ΔP = zero). As ΔP increases, the separation factor decreases (mainly due to the decrease in $C_3H_6$ permeance) but I still obtain excellent selectivity of 90±6 at ΔP = 8.5 bar. The permeance of $C_3H_6$ drops with increased pressure and that of $C_3H_8$ remains very small (about 0.3 GPU). Neither of these observations can be explained by a hypothesis of high-pressure defects, which would result in significant permeance increases for both mixture components. An alternative explanation can be proposed based on the fundamental characteristics of transport in nanoporous materials. The $C_3H_6$ molecules permeate through the ZIF-8 pores, and one expects a roughly logarithmic flux increase with pressure, due to the increasing saturation of adsorption sites and competitive adsorption by $C_3H_8$ molecules. This type of permeation behavior is indeed observed in Figure 32b, with the result that the $C_3H_6$ permeance (obtained by dividing the flux by ΔP) decreases with increasing feed pressure. On the other hand, $C_3H_8$ permeates very slowly through ZIF-8 (*i.e.*, it is limited by activated diffusion and not by adsorption) and potentially also through any small concentration of defects present in the membrane. Both these pathways would lead to a roughly linear increase in flux with ΔP and hence a roughly constant permeance, as observed in Figures 32a-32b. In Figure 32b, it is important to note that despite the decrease in $C_3H_6$ permeance, the increase in feed pressure leads to a large increase in $C_3H_6$ flux (by about a factor of 4.3 at ΔP = 8.5 bar in relation to ΔP = zero). To the best of my knowledge, only the group of Jerry Lin et al. have reported disk type ZIF-8 membrane performance data in the 1-4.5 bar feed pressure, showing a large drop in selectivity from 30 at 1 bar to 27 at 4.5 bar.[63]

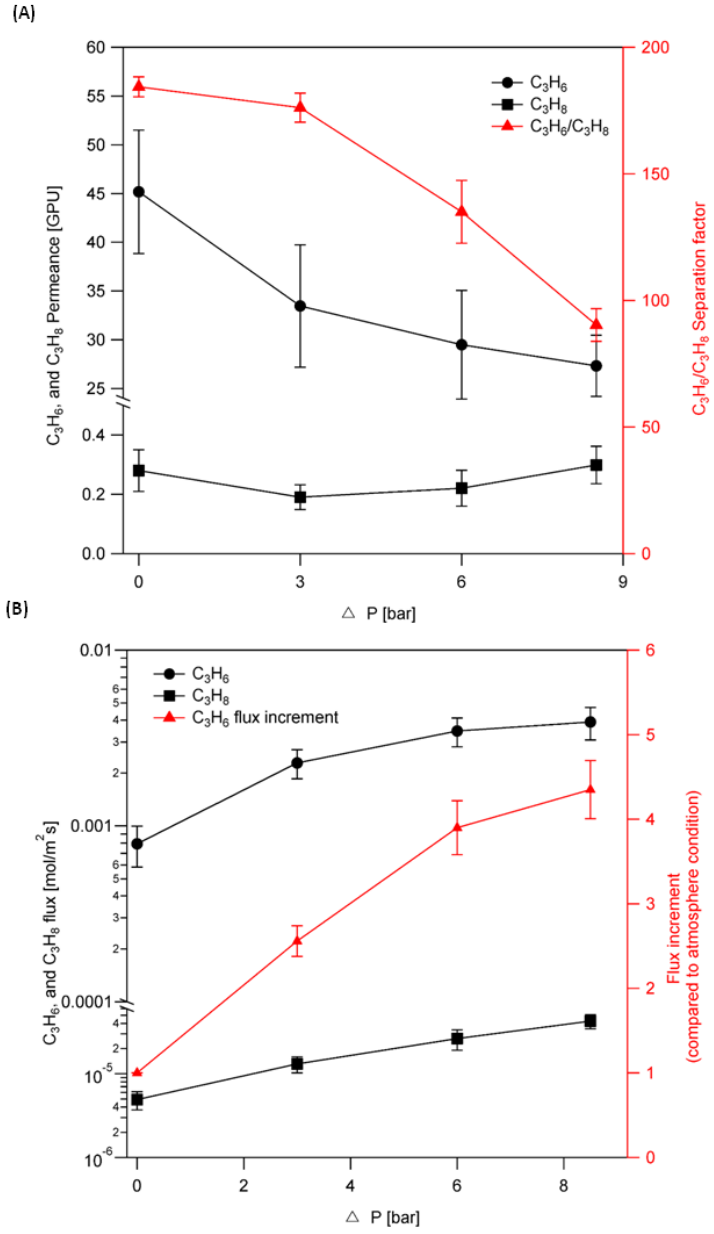


**Figure 32.** Binary equimolar $C_3H_6/C_3H_8$ and $H_2/C_3H_8$ separation properties of ZIF-8 hollow fiber membranes as a function of transmembrane pressure differential ΔP up to 8.5 bars: **(a)** permeance and separation factor, and **(b)** flux (absolute values as well as relative ratios with respect to the results obtained at 1 bar transmembrane pressure differential.

Figure 33 shows the results of longer-term operation of a ZIF-8 hollow fiber membrane that was continuously operated for 30 days with an equimolar binary $C_3H_6/C_3H_8$ feed at 25°C and 1 bar feed pressure. The membrane shows an initial $C_3H_6$ permeance of 50

GPU and a separation factor of 160, both of which are maintained over 30 days of operation, thereby indicating a durable molecular sieving membrane.

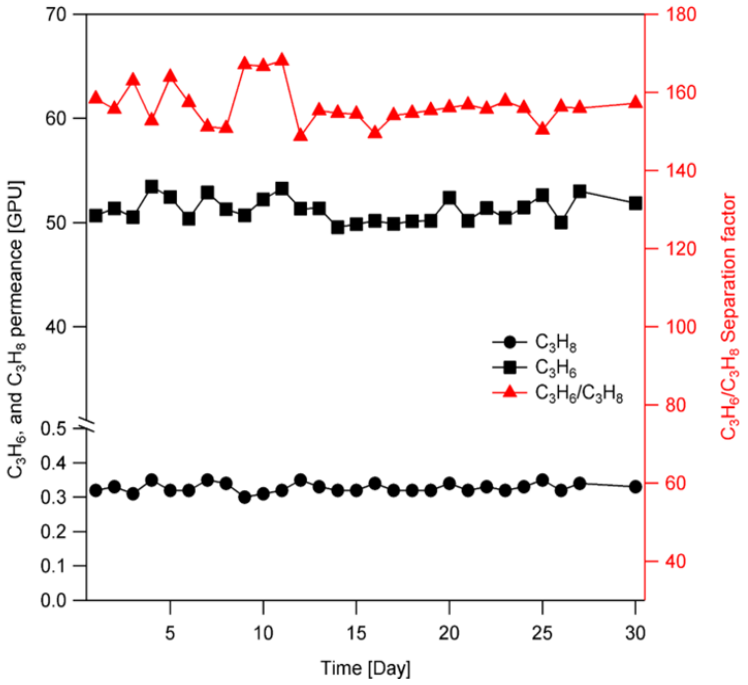


**Figure 33.** Permeance and separation factor of a ZIF-8 hollow fiber membrane operated continuously for 30 days under an equimolar $C_3H_6/C_3H_8$ mixture feed at 25°C and 1 bar feed pressure.

### 4.4 Conclusions

Defect-free ZIF-8 membranes have been fabricated on PAI hollow fibers by a novel IMMP technique, which has potential as a scalable methodology for MOF membrane fabrication. By controlling the characteristics of the hollow fiber and modifying the IMMP parameters, I have produced membranes with exceptional separation performances for $C_3H_6/C_3H_8$ and $H_2/C_3H_8$ mixtures. The present membranes also show excellent performance characteristics at elevated feed pressures of up to 9.5 bar, maintaining a $C_3H_6/C_3H_8$ separation factor of 90 and $C_3H_6$ fluxes as high as 4 mmol/m$^2$/s at 9.5 bar feed pressure. I also provide single-component data for a number of gases,

which clearly establish the molecular sieving properties of the membrane. The present ZIF-8 membranes also show excellent stability under longer-term operation, maintaining a $C_3H_6/C_3H_8$ separation factor of 160 and $C_3H_6$ permeance of 50 GPU over 30 days of continuous operation. Another important conclusion of this work is that high-quality ZIF-8 hollow fiber membranes can be directly fabricated on polymeric hollow fibers by a combination of control over IMMP parameters and support fiber morphology, without any need for surface treatments, intermediate steps, or post-synthesis treatments.

# CHAPTER 5.

# ZEOLITIC IMIDAZOLATE FRAMEWORK MEMBRANES ON MACROPOROUS CARBON HOLLOW FIBERS

## 5.1. Introduction

As mentioned in previous chapters, membrane-based separation is a promising idea for efficient separations of light hydrocarbons. Zeolitic imidazolate frameworks (ZIFs) have created great interest for use in high-performance membrane based separation systems for gas applications.[16] ZIF-8 membranes are the most extensively studied and account for more than 70% of published reports on ZIF membranes.[18] ZIF-8 membranes have been most extensively investigated for $C_3H_6/C_3H_8$ separation to replace energy-intensive cryogenic distillation.[5] A few other ZIFs, such as ZIF-7, ZIF-67, and ZIF-90, have also been fabricated into membranes.[34,35,37,129] In previous chapters, we have elucidated the IMMP methodology to process ZIF-8 membranes on PAI hollow fibers. However, the broader objective of IMMP is to provide a generalized processing platform for different types of ZIF/MOF membranes on/in scalable hollow fiber supports. In this chapter we consider two important and related issues: (1) fabrication of ZIF membranes for use in liquid- or vapor-phase separations, and (2) fabrication of ZIF membranes in an extended range of solvent and reactant environments. In both issues, the nature of the hollow fiber support assumes significance. Polymeric supports such as PAI can be susceptible to chemical instabilities such as swelling upon exposure to organic solvents such as DMF or NMP.[130] Swelling can be explained as a process of slow dissolution of a polymer by the solvent.[131] It begins with the diffusion and infiltration of

solvent molecules into polymer generating a swollen gel. Swelling effects can be mitigated, but not completely eliminated by crosslinking or strong hydrogen bonding. In the context of MOF membrane fabrication, two problems may thus arise. Firstly, the hollow fiber support may be unstable in the solvents required for synthesis of the MOF membranes. Secondly, MOF membranes may not be functional for organic liquid-phase separations (e.g., pervaporation) if the underlying polymeric support is weakened by the organic species, thereby leading to support-swelling-induced fracture of the MOF layer. For example, among three different phases of ZIF-7 (ZIF-7-I, ZIF-7-II, and ZIF-7-III), only ZIF-7-I and ZIF-7-II are nanoporous materials and can only be obtained in the presence of DMF, an aprotic polar solvent.[132,133] However, most polymer supports such as PVDF or PAI are easily swollen/soluble in DMF and therefore are unsuited for ZIF-7 membrane fabrication by IMMP. Similarly, even though high-quality ZIF-8 membranes can be fabricated on PAI hollow fiber supports, they cannot be used for important water/organic separations such as water/furfural or water/ethanol, since the organic species begins to swell the PAI support leading to a loss of membrane integrity.

Recently, the Lively group was able to successfully fabricate macroporous carbon hollow fibers.[7] These fibers were produced by a two-step process: spinning of macroporous polymeric hollow fibers followed by pyrolysis, under conditions that allow preservation of the macroporous nature of the fiber without substantial collapse into a dense carbon structure. The hypothesis of this chapter is that the use of carbon hollow fibers could allow the extension of IMMP to fabricate ZIF membranes to address the two main issues of important mentioned earlier. Here, for the first time, we demonstrate the successful

[7] Carbon fibers and cross-linked PVDF fibers were provided by Dr. Dong-Yeun Koh (Post Doc, School of Chemical & Biomolecular Engineering, Georgia Institute of technology)

fabrication of ZIF-8 and ZIF-90 membranes on the inner surfaces of carbon hollow fibers. We show that the use of carbon fiber supports allows us to use a wider range of solvents (especially for ZIF-90 membrane fabrication) and circumvent the swelling issue faced by PAI or other polymeric supports.

## 5.2 Experimental Methods

### 5.2.1. Materials

2-Methylimidazole (99%, 2-MeIM) and $Zn(NO_3)_2 \cdot 6H_2O$ (99%) were obtained from Sigma-Aldrich. 1-octanol was obtained from Acros Organics. Carboxyaldehyde-2-imidazole (99%, OHC-IM), dimethylformamide (99%, DMF), and methanol (99%, MeOH) were obtained from Alfa Aesar. Deionized water (DI-water) was produced with a Thermo Scientific 7128. Translucent epoxy (DP 100), and Fluorinert (FC-40) and were obtained from 3M. Corning Sylgard 184 was purchased from Ellsworth Adhesives. Silicone Gasket Maker was purchased from Permatex. Poly(vinylidene fluoride) (PVDF) was obtained from Alfa Aesar and dried under vacuum (60°C) overnight before use. N,N-Dimethylacetamide (DMAc, 99%, Sigma-Aldrich), lithium chloride (LiCl, 99.5%, Alfa Aesar), methanol (MeOH, 99.9%, Alfa Aesar), *p*-xylylenediamine (99.5%, Alfa Aesar), magnesium oxide (99.9%, Alfa Aesar) and sodium hydroxide (99%, Alfa Aesar) was used as received.

### 5.2.2. Fabrication of PVDF Hollow Fiber Supports

Polymer solution containing polymer (PVDF), non-solvent (lithium chloride and water), and solvent (dimethylacetamide) were prepared and the composition is listed in Table

10.[134] The polymer solution was fully mixed on a shear mixer for over a week and subsequently degassed by placing it steady upright position overnight before use. The polymer solution and bore fluid were loaded into separate high-pressure syringe pumps (Teledyne Isco, 500D), and a custom-made spinneret was used for the spinning process. A dry-jet/wet-quench solution spinning process was performed, and the spinning conditions are shown in Table 10. The post-spinning solvent exchange step includes soaking as-spun fibers in DI water for 3 days and further treatment of the fibers with methanol and hexane to remove any residual solvent and non-solvent from the fibers. The fibers were then dried under vacuum overnight (60 °C).

**Table 10.** Polymer solution compositions and hollow fiber spinning parameters.

| Conditions | Value |
|---|---|
| **Solution composition Case1: (PVDF/DMAc/DI-water/LiCl) (wt %)** | 25/71.5/1.05/2.45 |
| **Solution flow rate (ml/hr)** | 240 |
| **Bore fluid (DMAc/DI-water) (wt %)** | 80/20 |
| **Bore fluid flow rate (ml/hr)** | 160 |
| **Air gap (cm)** | 30 |
| **Take up rate (m/min)** | 40 |
| **Operating temperature (°C)** | RT |
| **Quench bath temperature (°C)** | 50 |

### 5.2.3. Fabrication of Cross-linked PVDF and Carbon Supports

To crosslink the PVDF hollow fiber support, one-pot crosslinking process using methanol as the solvent was used[134]. Crosslinking solution is prepared by dissolving 1g of sodium hydroxide (NaOH) and 4 g of p-xylylenediamine in 15 g of methanol. Additionally, 2 g of magnesium oxide powder was added to the solution as an acid scavenger. Fibers are

immersed into the solution and the slowly reacted on a shear mixer at room temperature for 44 hours. The fibers were solvent exchanged in the order of nitric acid (1M) solution, methanol, and hexane. The fibers were dried in vacuum oven overnight (120 °C). We confirmed that the initial morphology of the asymmetric hollow fiber support has not changed during crosslinking process.

Thermal pyrolysis was performed under inert argon conditions using a tube furnace. Oxygen level in the tube furnace was maintained below 10 ppm before each pyrolysis runs. Temperature protocol used are as follows: (1) 50 – 250 °C, 10 °C/min, (2) 250 – 535 °C, 3.8 °C/min, (3) 535 – 550 °C, 0.25 °C/min, (4) 550 °C, isothermal for 2 hr.

### 5.2.4. IMMP Modules, Mounting, and Sealing

Detailed descriptions of IMMP module can be found in the previous chapter 3.2.2. 4" length of cross linked PVDF or carbon fiber was prepared and introduced horizontally through the holes of the custom designed IMMP module. A small drop of silicon was then added to the shell of each fiber end where the fiber contacts the IMMP module interior. After allowing the silicon to be cured at least 24 hr, the excess fiber ends were removed with tweezers. $N_2$ permeance of the mounted fibers were then collected to ensure that the fiber was properly sealed by the silicon and that the bore had not been crushed/blocked.

### 5.2.5. Synthesis of ZIF-90 and ZIF-8 Membranes

*Case 1: ZIF-90 film synthesis on cross-linked PVDF fiber support*

10 mL of neat 1-octanol was first flowed through the fiber bore using a syringe pump. Next, 0.22 g zinc nitrate hexahydrate was dissolved in 40 mL 1-octanol and 4.5 g

Carboxyaldehyde-2-imidazole (OHC-IM) was dissolved in 80 mL DMF. 3mL of the octanol/$Zn^{2+}$ solution was then flowed through the bore and the pump flow rate was set to 0.6 ml/hr. The DMF/OHC-IM solution (~70 mL) was then slowly poured into the reaction chamber, immersing the fiber. The shell side solution was gently stirred at 60 rpm to prevent the formation of local concentration gradients. A temperature probe set at 30°C was then inserted into the reactor and the lid was used to cover the fiber interior during membrane growth. Here, membrane growth step was begun at 22 °C and with a linear increase in temperature to 42°C over 25 mins followed by a decrease to 30°C over 60 mins and steady holding at the latter temperature for the remainder of the synthesis. After 120 min of bore solution flow, the pump was turned off for 3.5 hr to provide a static growth step. Flow was then continued for 20 min followed by a final 3.5 hr growth step. To quench the reaction and remove excess Zn, 10 mL neat octanol was pushed through the bore while the shell solution was replaced with neat DMF (3 times). Next, 20 mL MeOH was flowed through the bore and the shell was soaked with 70 mL MeOH. The modules were then allowed to air dry at least 4 days before permeation testing.

*Case 2: ZIF-90 film synthesis on carbon hollow fiber support*

Here, synthesis was beginning with pre-treatment of the carbon fiber. 10 mL of neat DMF and 4.5 g Carboxyaldehyde-2-imidazole (OHC-IM) dissolved in 80 mL DMF were prepared. First, neat-DMF was flowed through the fiber bore using a syringe pump while OHC-IM/DMF precursor solution was poured through the shell side of the reactor. The shell side solution was gently stirred at 60 rpm. Then bore fluid was replaced with $Zn^{2+}$/1-Octanol (0.018 mol/L) and flow rate was set to 0.6 ml/hr to initial the reaction.

Reaction temperature was set to 30 °C Bore solution was flowed for 2 hr followed by 3.5 hr of static membrane growth step. Flow was then continued for 20 minutes followed by another 3.5 hr static growth step. The reaction was quenched following the ZIF-90 cross-linked PVDF fiber membrane synthesis procedure.

*Case 3: ZIF-8 film synthesis on carbon hollow fiber support*

A synthesis procedure similar to Case 2 was used except that neat MeOH was used as the bore side pre-treatment solution. First, 10 mL of neat MeOH and 9.0 g 2-Methylimidazole (2-MeIM) dissolved in 80 mL DI-water were prepared. Then, neat-MeOH was flowed through the fiber bore using a syringe pump while 2-MeIM/DI-water precursor solution was poured through the shell side of the reactor. The shell side solution was gently stirred at 60 rpm. Then the bore fluid was replaced with $Zn^{2+}$/1-Octanol (0.018 mol/L) and the flow rate was set to 0.6 ml/hr to initiate the reaction. Reaction temperature was then set to 30 °C. Bore solution was flowed for 2 hr followed by 3.5 hr of static membrane growth step. Flow was then continued for 20 minutes followed by another 3.5 hr static growth step. The reaction was quenched in the same manner as the ZIF-90 cross-linked PVDF fiber membrane synthesis procedure.

### 5.2.6. Characterization

Cross-sectional images of ZIF membranes were collected with a Hitachi SU-8010 scanning electron microscope after a thin layer of gold was sputtered onto the cross-sectional surface. The samples were soaked with a hexane solution for 30 min followed by dipping into liquid nitrogen for a clean cut. The membrane thickness was obtained by

averaging thickness measurements made at different cross-sections along the 5 cm fiber length. All permeation measurements were performed by the time-lag or the Wicke-Kallenbach technique.[76,135] In the time-lag technique, both the feed and permeate side were maintained under vacuum. Then, gas was fed into the permeation module at a constant pressure and temperature. The pressure increase on the permeate side (equivalent to the number of permeated gas molecules) was recorded over time using a pressure transducer (Omega). The steady-state Wicke Kallenbach technique was used to test binary *n*-C4H8/*i*-C4H8 mixtures (Figure 34). Specifically, 1:1 feed mixtures were flowed through the bore at 20 mL/min while an Ar sweep gas was flowed across the shell at 30 mL/min using MFC (Aalborg, GFC17S). For binary mixture permeation measurements, gases were well mixed at a mixer before entering the feed side of the module. The temperature of the module was controlled by placing it in a convection oven (Cole Parmer). A carefully calibrated gas chromatograph with FID detectors (Shimadzu GC-2014) was used to determine the composition of the permeate. Permeation data were measured for three different membranes synthesized under the same conditions.

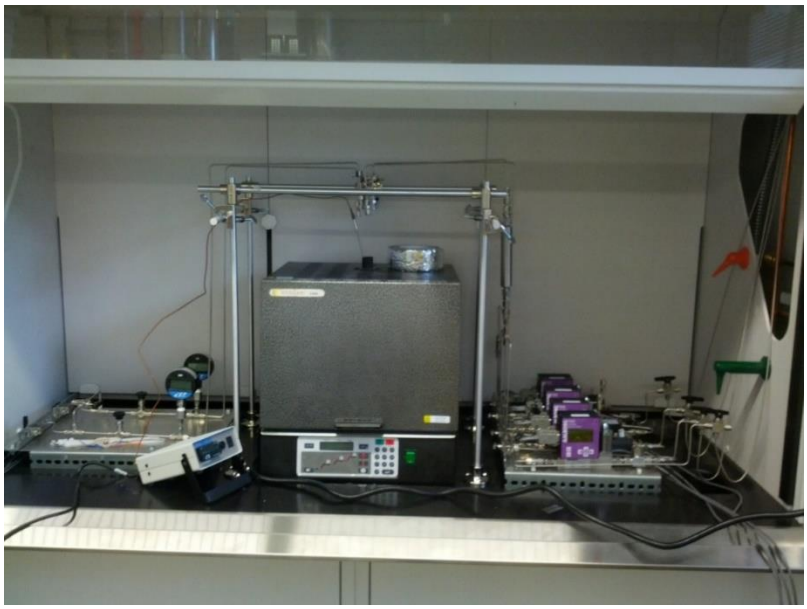

**Figure 34.** Photograph of mixed gas permeation equipment.

## 5.3. Results and Discussion

### 5.3.1. Carbon Supported ZIF-8 and ZIF-90 Membrane Fabrication

Figure 35 shows a schematic of IMMP for ZIF-90 membrane synthesis on the inner surface (bore side) of carbon hollow fibers. In my previous work, I used DI-water as a solvent to deliver the ZIF-8 linkers to the shell side during IMMP. However, here I choose DMF as the shell-side solvent since the ZIF-90 linker (OHC-Im) has very poor solubility in water. The solubility of OHC-Im in DMF (an aprotic polar solvent) high enough that one can prepare a concentrated solution (0.58 mol/L) that can boost the rate of ZIF-90 nucleation when contacting with the metal precursor ($Zn^{2+}$) present in the 1-octanol bore fluid. However, the use of DMF leads to another issue of the stability of the PAI (Torlon) support fiber, which is easily degraded by DMF or other aprotic polar solvents. Therefore, I used cross-linked PVDF fibers as supports for ZIF-90 membrane growth.[134] Cross-linked PVDF(c-PVDF) fibers can be produced by a post-spinning

crosslinking strategy using *p*-xylylenediamine as a crosslinking agent between the polymer chains ( Experimental Section). The resulting fiber supports exhibit improved tolerance towards solvents including DMF and NMP. Free surface amine groups (generated by the *p*-xylylenediamine treatment) can also be beneficial for heterogeneous nucleation of ZIF-90 by increasing the affinity with the carbonyl groups of OHC-Im. Figure 36a-b shows a cross-sectional SEM image of the ZIF-90 membrane grown on a c-PVDF fiber. A ZIF-90 layer is clearly observed on the inner surface of the c-PVDF fiber. However, the film was is poorly adhered to the support surface and is partially crumpled, mainly because of the swelling of the support fiber. The c-PVDF support, while more resistant than PAI to swelling by DMF, is still considerably swelled during the membrane synthesis. During the drying step it shrinks back to its original dimensions, creating an interfacial strain that results in detachment of the ZIF-90 membrane. Therefore, it was concluded that polymer supports in general are of doubtful utility for synthesis of ZIF-90 membranes. As a result, it was decided to replace polymeric supports with pyrolyzed carbon supports, specifically by pyrolysis of the c-PVDF fibers (Experimental Section).[134] The membrane synthesis steps otherwise remained identical. As seen in Figure 37a, a continuous ZIF-90 layer has been formed inside the carbon support (rather than on the surface). Although some large crystals of ZIF-90 are found on the inner surface of the fiber, they do not form a continuous layer and are only seen in a few regions. EDX elemental mapping of zinc (Figure 37b) also confirms the localization of ZIF-90 layer inside the fiber. Membranes embedded inside the support have certain advantages. Such membranes usually have higher mechanical strength and stability because of its better interlocking with the porous support. Secondly, it has a larger

circumference than a membrane on the inner-surface. In the present case, the circumference is about 16 % greater than an inner-surface membrane.On the other hand, the tradeoff is that support-embedded membranes have a reduced effective area (since it is interlocked with the support material) and hence a reduced effective permeability.. The microstructure of the carbon support was imaged by SEM and analyzed by the image analysis software ImageJ (Figure 38). The impermeable fraction of the carbon support isvolume is about 62.8% and the porosity is about 37.2%. The net result of circumference and support porosity effects is that that the effective surface area (per unit fiber volume) of the ZIF-90 support-embedded membrane is about 43 % that of an inner-surface membrane.

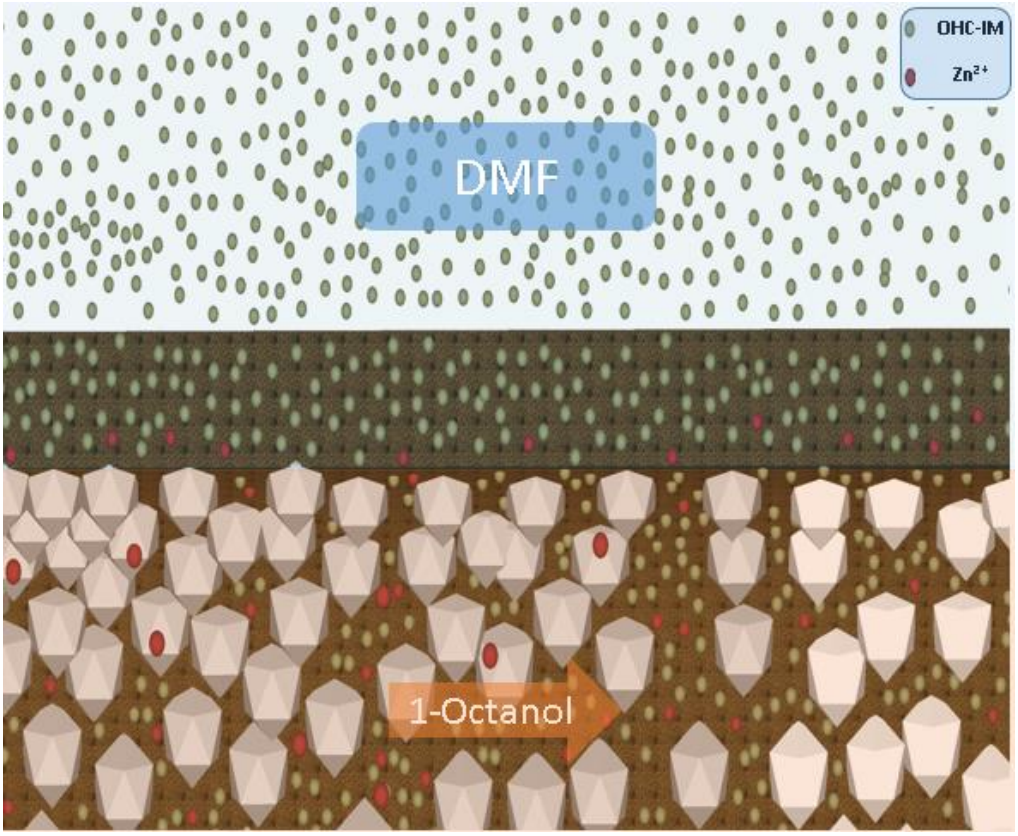


**Figure 35.** A schemtics of IMMP for ZIF-90 membrane synthesis on the inner surface (bore side) of carbon hollow fibers.

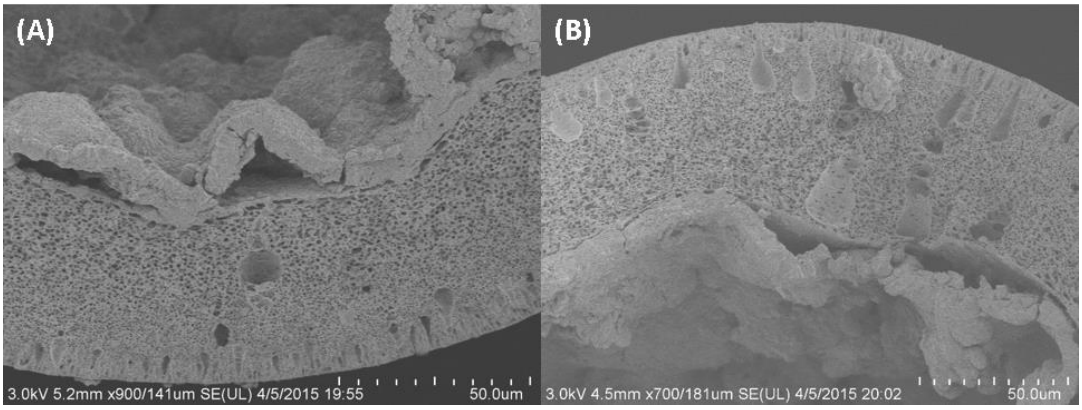


**Figure 36.** (a, b) Cross sectional SEM image of ZIF-90 cross linked PVDF fiber membrane showing partically folded film structure inside the fiber bore.

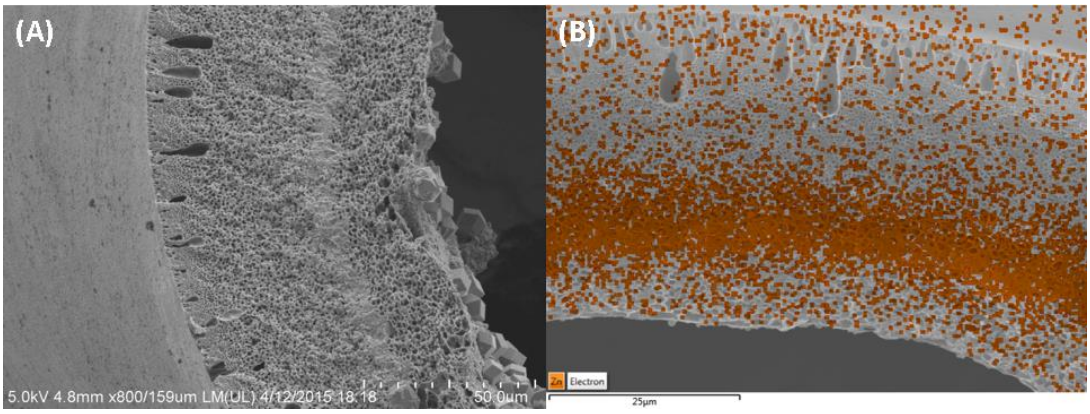


**Figure 37.** (a) SEM image of ZIF-90 membrane grown inside of carbon fiber (b) EDX elemental maps of zinc (orange) showing the localization of the ZIF-90 membrane inside the fiber.

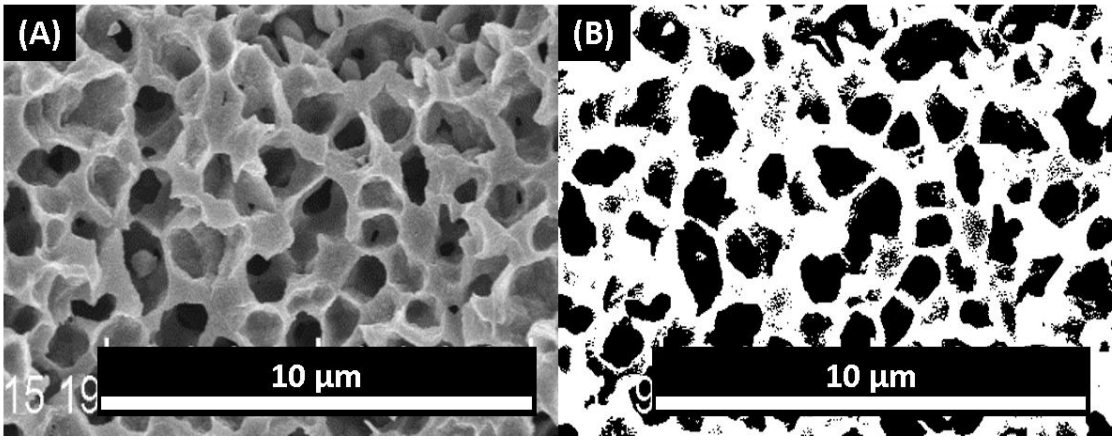


**Figure 38.** Cross-sectional SEM images of (a) carbon fiber, and (b) associated binary images for porosity estimation.

As qualitatively explained by Brown et al, the location of the membrane (inner surface, outer surface, or inside the fiber itself) can be controlled by several factors such as the miscibility of the shell and bore side solvents, the diffusion rates of the two reactants, and the order of introduction of the shell and bore side solutions (i.e., initial conditions).[9] I hypothesized several possible reasons for the formation of the ZIF-90 membrane inside of the support. Firstly, it is possible that the driving force (concentration gradient) of the shell-side precursor is not enough to penetrate into the bore side, and the crystallization front moves into the support. Secondly, the relatively low permeability (e.g, 12000 GPU $N_2$) of the carbon support (compared to the PAI support: ~77000 GPU $N_2$) may also hinder efficient penetration of the linkers to the bore side. However, I previously reported the fabrication of ZIF-8 IMMP membranes varying either the precursor concentration (Figure 28) or the permeance of support (Figure 22). Based on the results, we can infer that these variables mainly affect the thickness and quality of the ZIF-8 layer and not the membrane position. Thus we can presently exclude the above two possibilities as unlikely. Thirdly, the hydrophobic nature of the carbon fiber might prevent DMF from penetrating fully into the bore side of the carbon fiber. The two solvents (DMF and 1-octanol) keep the reactants separated in different phases everywhere except at the solvent interface. The initial film formed at the interface then acts as a barrier that restricts the contact of the zinc ions and linker except at the defects. The hydrophobic carbon fiber may slow down the wetting of the fiber pores with DMF precursor solution, so that the crystallization front/interface has to form inside the fiber. Brown et al. also studied five combinations of precursor solutions and locations, and showed that the positioning and order of introduction of the solvents can influence of the position of ZIFs layer.[9] To test the

possibility of solvent effects, the IMMP protocol was modified in order to try and relocate the interface to the inner surface of the support. The initial step of the IMMP procedure was altered to allow saturation of the support pores by introducing neat DMF through the bore side of the fiber for 10 min, while a 0.58 mol/L OHC-Im/DMF solution is simultaneously added to the shell as in the usual IMMP. Then, the bore side DMF stream was replaced with the usual $Zn^{2+}$/1-octanol solution and the rest of the procedure is continued in the usual manner (Experimental Section). Since the entire support has now been saturated with DMF before octanol is introduced, it is hypothesized that the DMF/octanol interface would relocate to the inner surface of the fiber. The cross-sectional SEM images of ZIF-90 membrane fabricated by the modified procedure (Figure 39a-b) clearly support the validity of my hypothesis. A continuous and well-adhered ZIF-90 membrane is formed on the inner surface of the fiber. The thickness of the membrane has been measured at 5 different locations along the axial direction, and Figure 40 shows that a ZIF-90 layer of thickness 3.1 ± 0.5 μm has been formed. EDX elemental maps of zinc also confirm the relocation of the ZIF-90 layer to the inner surface of the fiber (Figure 41). Thus, by a novel strategy involving the use of chemical inert supports as well as modifications to the IMMP protocol, I have overcome the limitations of solvent selection and fiber swelling that previously restricted the generalized application of IMMP. Additionally, the generality of the newly developed methods above has been demonstrated by also fabricating ZIF-8 membrane layer on the inner surface of carbon fibers (Figure 39c).[8]

[8] ZIF-8/carbon fiber membranes were fabricated by the Nair group member Chen Ma.

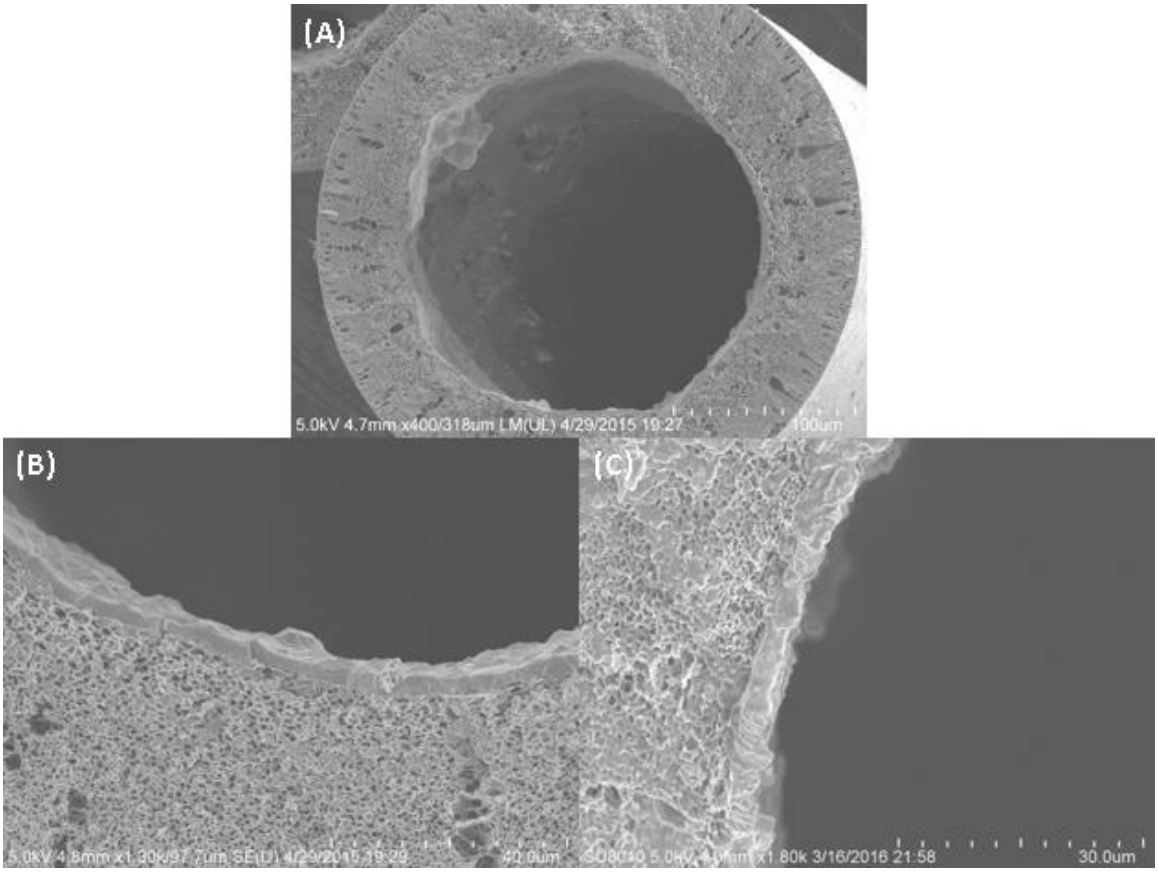


**Figure 39.** Cross sectional SEM images of (a), (b) ZIF-90 carbon hollow fiber membrane (c) ZIF-8 carbon hollow fiber membrane.

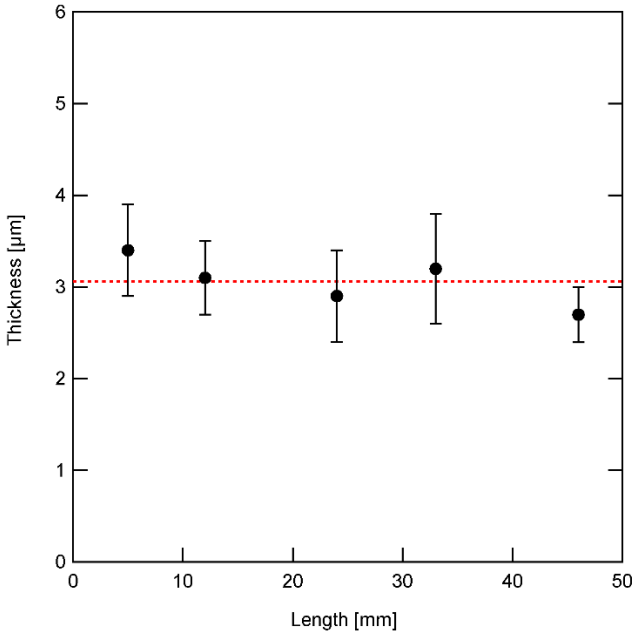


**Figure 40.** ZIF-90 layer thickness measured from SEM cross-sections obtained along the 5 cm length of membrane.

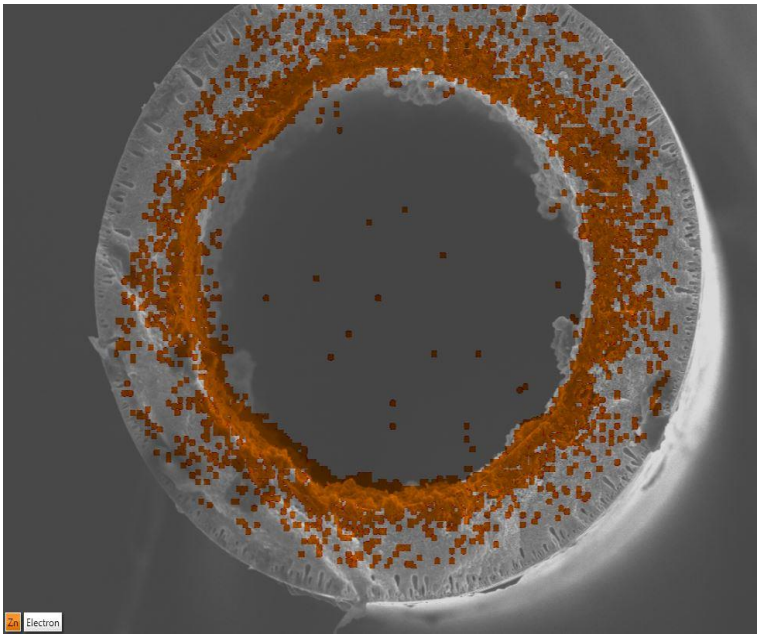


**Figure 41.** EDX elemental maps of zinc (orange) showing the localization of the ZIF-90 membrane inside the carbon fiber.

### 5.3.2. Single Component Permeability of ZIF-90 Membranes

Previously, I reported ZIF-8 membrane single-component permeabilities of different gases (at 25°C and transmembrane partial pressure differential of 2 bar) as a function of kinetic diameter.[68] Here I compare these results with those from the ZIF-90 membrane.(Figure 42) In general, both ZIF-8 and ZIF-90 membranes show molecular sieving properties and the molecular permeability decreases with increase in kinetic diameter of guest molecules. It is noted that the crystallographically derived pore sizes of ZIF-8 and ZIF-90 are nearly identical at 3.4 Å and 3.5 Å respectively. However, the actual permeability drop associated with molecular sieving was observed around the kinetic diameter of 4.2 Å (ZIF-8) and 5.0 Å (ZIF-90) respectively, indicating that both materials have flexible pores and the “rigid pore aperture” assumption is not valid for

either ZIF-8 or ZIF-90. Therefore, I designate 4.2 Å and 5.0 Å as the effective molecular sieving pore sizes of ZIF-8 and ZIF-90 respectively. Guest molecules that have smaller kinetic diameter than the effective pore size form the Group 1. ZIF-8 and ZIF-90 are not particularly size-selective for Group 1 molecules, which range from $H_2$ upto $C_3H_6$ (for ZIF-8) and *n*-$C_4H_{10}$ (for ZIF-90). Group 1 shows very similar permeability trends in both ZIF-8 and ZIF-90 including small anomalies from the general trend of decreasing permeability with increasing kinetic diameter. I explained in Chapter 3 that these small anomalies involving light hydrocarbons ($CH_4$, $C_2H_4$, and $C_2H_6$) in ZIF-8 is mainly due to the contribution of strong adsorption.[68] The same anomalies occurring in ZIF-90 can also be explained by adsorption properties. For example, ZIF-90 shows much stronger adsorption of $C_2H_4$ compared to $N_2$ (Henry constants of $C_2H_4$ and $N_2$ are 1.81 mmol/g·bar and 0.1 mmol/g·bar, respectively at 35 °C). It is also noted that the ZIF-90 permeability of *n*-$C_4H_{10}$ is higher than that of *n*-$C_3H_8$, and it can be explained by the ~6 times stronger henry constant of *n*-$C_4H_{10}$ at 35 °C (Figure 43). Group 2 includes molecules with kinetic diameters larger than the effective aperture size, and range from $C_3H_8$ to $SF_6$ for ZIF-8 and *i*-$C_4H_{10}$, to $SF_6$ for ZIF-90. The effect of size exclusion is seen in the form of low permeabilities of Group 2 molecules for both ZIF-8 (<2 Barrer) and ZIF-90 (<20 Barrer). These observed permeabilities are mostly comprised of transport through any defects remaining in the membrane. The expected permeability of *i*-$C_4H_{10}$ in ZIF-90 was calculated using the Maxwell-Stephan formulation with weak confinement assumption, and the diffusion and adsorption parameters were obtained from our previous work.[22] Based on the calculation, the theoretical *i*-$C_4H_{10}$ permeability was estimated as 0.08 Barrer which is much smaller than the experimental result of 35 Barrer, clearly indicating

the presence of significant defects unlike the IMMP ZIF-8 membrane. This difference may be explained by the degree of stability of solvent interfaces (DI-water/1-octanol versus DMF/1-octanol). We used the DI-water/1-octanol solvent pair for ZIF-8 membrane fabrication. These solvents are immiscible, leading to the creation of a sharp and stable interface (Figure 44). However, the DMF/1-octanol solvent pair for ZIF-90 membrane fabrication is somewhat miscible and lead to a relatively unstable/diffuse interface. Therefore, we can infer that this membrane is more vulnerable to the existence of irregularities on the surface of the support. Further work is needed to either improve the quality of carbon fiber supports further or investigate other possible immiscible solvent pairs for a more stable interface.

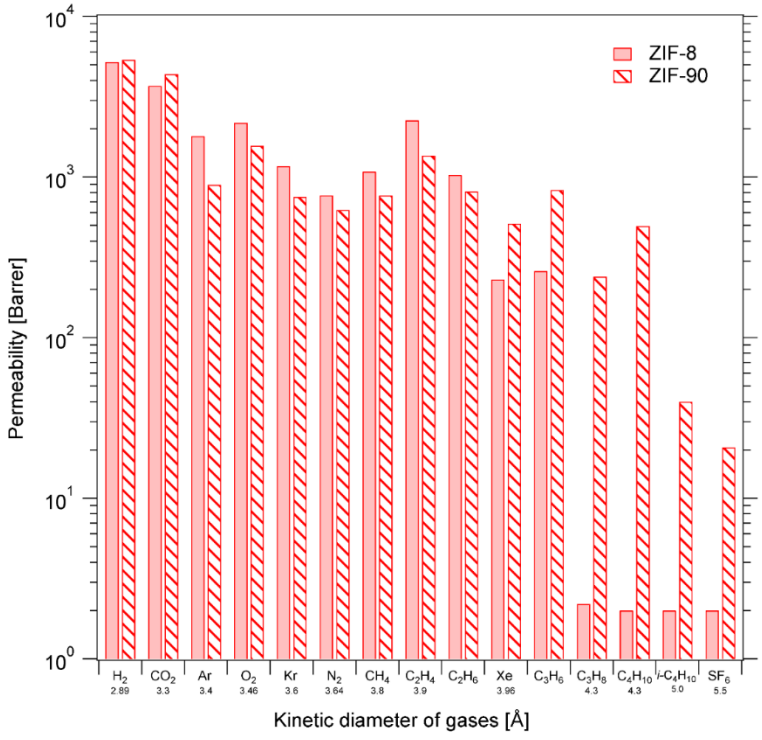


**Figure 42.** Single gas permeabilities of ZIF-90 carbon and ZIF-8 torlon hollow fiber membranes by the time-lag techniques at 25 °C

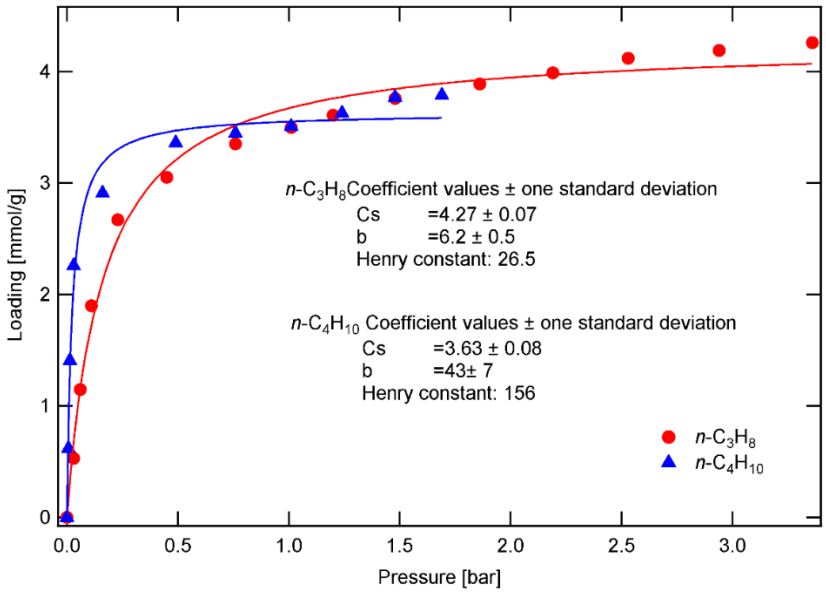


**Figure 43.** Adsorption isotherms at 35°C of *n*-$C_3H_8$ and *n*-$C_4H_{10}$, for materials with ZIF-90. The solid lines represent Langmuir model fits and parameters and henry constant also tabulated.

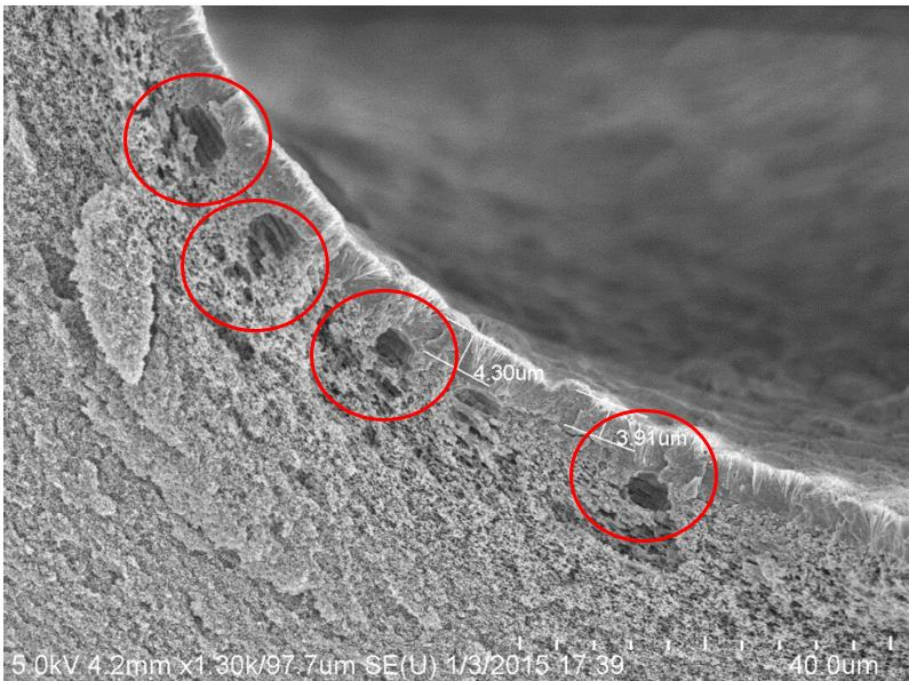


**Figure 44.** Cross-sectional image of ZIF-8 IMMP membrane using DI-water/1-octanol solvent pair. Red circle indicates possible crack location due to irregular PAI fiber surface.

### 5.3.3. Binary Gas Mixture Separation Performance of ZIF-90 Membranes

In my previous work, I demonstrated the possibility of butane isomer separation by ZIF-90 due to a diffusion selectivity up to 900.[22] To investigate the performance of ZIF-90 membranes, the equimolar binary mixture *n*-$C_4H_{10}$/*i*-$C_4H_{10}$ separation were characterized as a function of temperature with the Wicke-Kallenbach technique at a feed pressure of 1 bar. Molecular sieving effects are observed, with *n*-$C_4H_8$/*i*-$C_4H_8$ separation factors of 12 within the temperature range 25-120 °C. (Figure 45). Previously I reported binary equimolar $C_3H_6$/$C_3H_8$ separation by ZIF-8 membranes (Figure 31), and showed that the permeance of $C_3H_6$ decreases with increasing temperature since it is mainly dominated by adsorption. However, in the present case of ZIF-90 it is found that *n*-$C_4H_{10}$ permeance increased with temperautre indicating activated transport through the ZIF-90 pores. It is also noted that the present ZIF-90 membrane shows the *n*-$C_4H_{10}$/*i*-$C_4H_{10}$ separation factor of about 12, which is substantial but still much lower than that expected from diffusivity data. . The measured permeances of *n*-$C_4H_{10}$ and *i*-$C_4H_{10}$ are 60 GPU and 5 GPU respectively at RT, and these can be compared with expected permeances calculated using the Maxwell-Stefan formulation (Eq 7) with diffusion and adsorption parameters obtained from our previous work.[22] These expected permeances come out to be 44 GPU and 0.03 GPU respectively. Therefore, it appears that nearly all the observed *i*-$C_4H_{10}$ permeance is from defects in the ZIF-90 membranes. Optimization of the ZIF-90 IMMP on carbon fibers could focus on further reduction of defect permeance by using better quality (uniform inner surface) support, exploring possible solvents pair for stable interface, variating of growth conditions, or by post synthesis treatments.

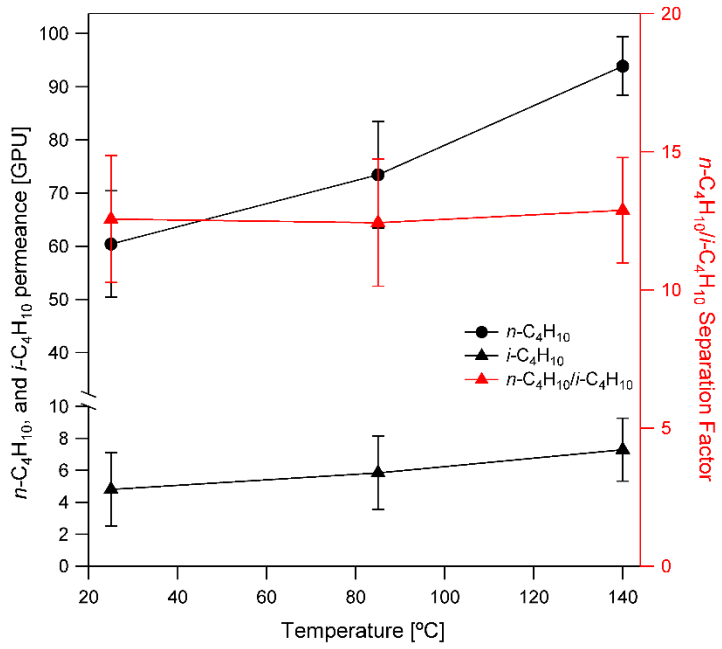


**Figure 45.** (a) Binary equimolar $n$-$C_4H_8$/$i$-$C_4H_8$ gas mixture separation properties of ZIF-90 carbon fiber membranes as a function of temperature at a feed pressure of 1 bar.

### 5.4. Conclusions

In this chapter, we demonstrated for the first time that ZIF-90 and ZIF-8 membranes can be grown on carbon hollow fiber supports. This development, aided by the fabrication of novel carbon hollow fiber supports as well as rational engineering of the IMMP techniques, shows the versatility of the IMMP methodology and also allows the possibility of a wider range of solvent selection. These membranes can also be applicable to liquid-phase separations such as furfural/water and ethanol/water, being investigated by other members of the Nair group using the above membranes. Additionally, the low cost and benign IMMP route, excellent chemical & mechanical strength of carbon fibers, and freedom from intermediate or post-synthesis steps, further promote the value of IMMP-based ZIF membrane fabricaton as a notable step toward realizing scalable fabrication of MOF membranes.

# CHAPTER 6.

# CONCLUSIONS AND FUTURE WORKS

## 6.1. Main Findings

In Chapter 2, I demonstrated that the effective pore size, and hydrophilicity of ZIFs can be continuously and drastically tuned using mixed-linker ZIFs containing two types of linkers, allowing their use as a more general molecular separation platform. This remarkable behavior was illustrated by adsorption and diffusion measurements of hydrocarbons, in mixed-linker ZIF-$8_x$-$90_{100-x}$ materials with a large range of crystal sizes (338 nm to 120 μm), using volumetric, gravimetric methods. NMR, powder FT-Raman, and micro-Raman spectroscopy unambiguously confirm the mixed-linker nature of individual ZIF crystals. Variation of the mixed-linker ratio (x) allows continuous control of n-butane, i-butane diffusivities over 2-3 orders of magnitude.

In previous work, Brown *et al* at Georgia Tech recently introduced a methodology for fabricating polycrystalline metal-organic framework (MOF) membranes - referred to as Interfacial Microfluidic Membrane Processing (IMMP) - which allows parallelizable fabrication of MOF membranes inside polymeric hollow fibers of microscopic diameter.[9] Such hollow fiber membranes, when bundled together into modules, are an attractive way to scale molecular sieving membranes. The understanding and engineering of fluidic processing techniques for MOF membrane fabrication is in its infancy. In Chapter 3, we developed a detailed mechanistic understanding of MOF (ZIF-8) membrane growth under microfluidic conditions in polyamide-imide hollow fibers without any intermediate steps (such as seeding or surface modification) or post-synthesis treatments. A key finding is that interfacial membrane formation in the hollow fiber occurs *via* initial formation of

two distinct layers and subsequent rearrangement into a single layer. We then used this understanding to show how non-isothermal processing allows fabrication of thinner (5 μm) ZIF-8 films for higher throughput, and furthermore how engineering the polymeric hollow fiber support microstructure allows control of defects in the ZIF-8 membranes.

In Chapter 4, we focus on further optimizing the performance of these engineered ZIF-8 membranes, with particular focus on propylene separation at higher pressures. We reported the control of the fiber microstructure as well as optimization of the IMMP conditions, which allow us to achieve a $C_3H_6/C_3H_8$ separation factor as high as 180 (at 1 bar and 25˚C) and which remains high (60) at 120˚C. Furthermore, high-pressure operation of these membranes was investigated. Detailed permeation measurements indicated excellent suppression of defects at higher pressures up to 9.5 bar, allowing a $C_3H_6/C_3H_8$ separation factor of 90 at 9.5 bar. The membranes also displayed a fourfold increase in flux at 9.5 bar compared to operation at 1 bar. The long-term stability of the ZIF-8 hollow fiber membranes was demonstrated by continuous operation over a month without loss of $C_3H_6$ permeance or selectivity.

Finally, in Chapter 5 I made progress towards a more generalized ZIF membrane fabrication platform by extending IMMP to macroporous carbon hollow fiber supports. Here I overcame several additional hurdles for practical MOF membrane fabrication, including address the problems of polymer hollow fiber swelling issues and solvent limitations. I showed the versatility of IMMP by modifying it for the successful fabrication of selective ZIF-90 and ZIF-8 membranes on the inner surface of carbon fibers. The ZIF-90 membrane shows a good $n$-$C_4H_8/i$-$C_4H_{10}$ separation factor of 12 indicating clear molecular sieving effects.

## 6.2. Future Work and Challenges

### 6.2.1. Extended ZIF Mixed-Linker Approach

In this thesis we clearly demonstrated tunable molecular sieving in ZIFs by controlling the pore size by a mixed-linker (hybrid) approach. We focused on the use of ZIF-8-90 hybrid materials for *n*-butane/*i*-butane gas pair separations. This idea can be extended to reduce the pore size starting from ZIF-8 material in order to separate other gas pairs of interest such as ethylene/ethane or Kr/Xe. For example, linker pairs such as 2-bromoimidazole/2-MeIM or 2-ethylimidazole/2-MeIM may allow control reduction of pore size and changes in pore shape Once these tunable properties are demonstrated on mixed-linker crystals, one can develop approaches to modify IMMP for the synthesis of mixed-linker ZIF membranes on polymeric or carbon hollow fibers. This would be another important step in generalizing the hybrid ZIF/IMMP platform for a range of gas separations.

### 6.2.2. Scale-up of IMMP

Light olefin (propylene and ethylene) production is the most energy-consuming and $CO_2$-emitting process in the chemical industry (~120 trillion BTU/yr and 40 million tons/yr $CO_2$ in the US alone) and has a US (global) market size of ~$50 (200) billion. Ethylene/ethane and propylene/propane separations are carried out by cryogenic or conventional distillation, which are highly capital- and energy-intensive. Membrane-based separation is a promising idea for efficient olefin separations, but currently available or proposed membranes are constrained by incrementally better performance

and/or high cost of scale-up. If successfully applied to propylene production, it is estimated that ZIF-8 hollow fiber membrane technology could save up to ~$15 billion/yr along with ~25 million tons/yr $CO_2$ emission savings worldwide.[10] The IMMP concept allows us to fabricate nanoporous, high-performance olefin separation membranes inside low-cost, macroporous polymeric hollow fiber supports at near-ambient liquid-phase conditions.[9,46,68] In future work, one could focus on engineering the flow-based *in situ* fabrication process in detail to create scaled-up modules containing up to 100 densely-packed fibers in a single module, with the packed fibers providing very high membrane surface area per unit module volume (1,000-10,000 $m^2/m^3$) that maintain low defect density and desirable performance (specifically, propylene permeance and selectivity in the pressure and temperature range of interest). This would be an important step forward in the scalable fabrication of IMMP-based membranes for future commercial applications. -grade (99.5+%) propylene.

### 6.2.3. Defect Control Strategies

Membrane defects such as pinholes, cracks, or grain boundaries can be formed for a number of reasons and should be controlled to improve the performance of ZIF membranes for gas separation.[136] Capillary stresses can be caused during post-synthesis drying or other finishing procedures, and different thermal expansion rates of the support and the MOF layer can cause thermal stresses that may lead to cracks or other defects and lower the performance of the membrane. Further study and optimization of these procedures might be very meaningful to improve the performance of ZIF membranes. Post-treatments of IMMP-fabricated ZIF membranes could also be examined. Fibers with

pinhole defects can be repaired by “caulking” the surface with a polymer. The objective of the treatment is to greatly decrease the permeances through pinholes and reduce their overall contribution to the membrane. selectivity.[137] Typically, a 5 wt. % PDMS/heptane solution is infiltrated through membrane defects and the treated membrane is then dried to evaporate the heptane and leave the PDMS inside the defect pores to block them. The optimization of IMMP to allow such post-treatments may be a worthwhile addition to the repertoire of techniques that can be developed under the IMMP platform for MOF membrane processing.

# APPENDIX A

# EXTERNAL AND SUPPORT MASS TRANSFER RESISTANCES

The total permeation resistance ($R_{\text{Total}}$) through the membrane is modeled as a result of three series resistances (Equations 22-23): membrane layer ($M_{\text{embranes}}$), support ($R_{\text{Torlon}}$), and external ($R_{\text{external}}$).[76] To quantify the contributions of the support+external mass transport resistances to the total resistance through the membrane, we obtained single-component gas permeation data through the bare hollow fiber at 25°C. For the most accurate estimate from a fiber that has been exposed to actual processing conditions, we performed IMMP on the bare Torlon® fiber with only the 2-mIm reactant and no metal source (to prevent ZIF-8 formation), and the PDMS end sealing procedure was also performed. Using the measured bare-fiber permeances along with the permeances from the ZIF-8 membrane, Equations 22-23 were used to back-calculate the value of $R_{\text{Torlon}}+R_{\text{external}}$ and therefore determine the corrected values of $R_{\text{membrane}}$ and $P_{\text{membrane}}$ (GPU) as shown in Table 11. External and support resistances lead to only a correction of 0.01-4% in the permeance measurements for the three gases, which is negligible.

$$R_{membrnae} = \frac{1}{P_{membrane}} \tag{22}$$

$$R_{Total} = R_{membrane} + R_{Torlon+external} \tag{23}$$

**Table 11.** Single gas permeance results before and after considering the effect of Torlon® fiber and external mass transfer resistances at 25 °C.

| Gas | Measured Permeance (GPU) | Corrected Permeance (GPU) | Error |
|---|---|---|---|
| **Propane** | 1.0 | 1.0 | 0.01 % |
| **Propylene** | 66.5 | 66.8 | 0.5 % |
| **Hydrogen** | 1537 | 1596 | 3.7 % |

# APPENDIX B

# QUANTIFICATION OF MEMBRANE PERMEATION PATHS

To quantify the contributions of the *d* and *b* pathways to the total permeation through the membrane using Equations 20-21, we obtained experimental data on single-component molar flow rates of 4 gases (propylene, propane, *n*-butane, and *i*-butane) through the membranes at 25°C and a pressure differential of 103 kPa before and after PDMS sealing (a total of 8 data points, Table 12).[9] This represents the LHS of Eq. (20) and (21). On the RHS, the permeabilities of the four gases through ZIF-8 are well known from the literature.[121] Using the overall membrane dimensions (diameter = 200 μm, length = 50 mm) and the known pressure differential, the term $\left(\frac{N_i}{\Delta P}\right)_z$ is thus known for all four gases. The factor $\theta = (50 - 2\times8)/50 = 0.68$, since Brown et al. find (from Figure 46) that the PDMS penetrates 8 mm into each end of the fiber.[9] The permeation selectivities in PDMS (α) of the gases relative to propylene are also well known from the literature[138,139]. In contrast to ZIF-8 which is highly hydrogen-selective over hydrocarbons, PDMS has a mild 'inverse' selectivity for hydrocarbons over hydrogen.

Thus, the three unknown parameters in Eq. (20) and (21) are:

$$\left(\frac{N_{C_3=}}{\Delta P}\right)_d, \left(\frac{N_{C_3=}}{\Delta P}\right)_b, \text{ and } \left(\frac{N_{C_3=}}{\Delta P}\right)_{b-PDMS}.$$

These parameters were fitted by nonlinear least squares to the experimental data, yielding the following best-fit values (all in $mol.s^{-1}.Pa^{-1}$) for the reference component (propylene):

[9] Thus measurement was done by Nair group member Andrew Brown.

$$\left(\frac{N_{C_3=}}{\Delta P}\right)_d = 6.1\times10^{-14},\ \left(\frac{N_{C_3=}}{\Delta P}\right)_b = 3.7\times10^{-14},\ \text{and}\ \left(\frac{N_{C_3=}}{\Delta P}\right)_{b-PDMS} = 1.0\times10^{-16}$$

These parameter values fit the experimental data with an overall error of 7.2%.

We then use the fully parametrized Eq. (20-21) to quantify the relative contributions of the three pathways to the total permeance, as shown in Table 13.

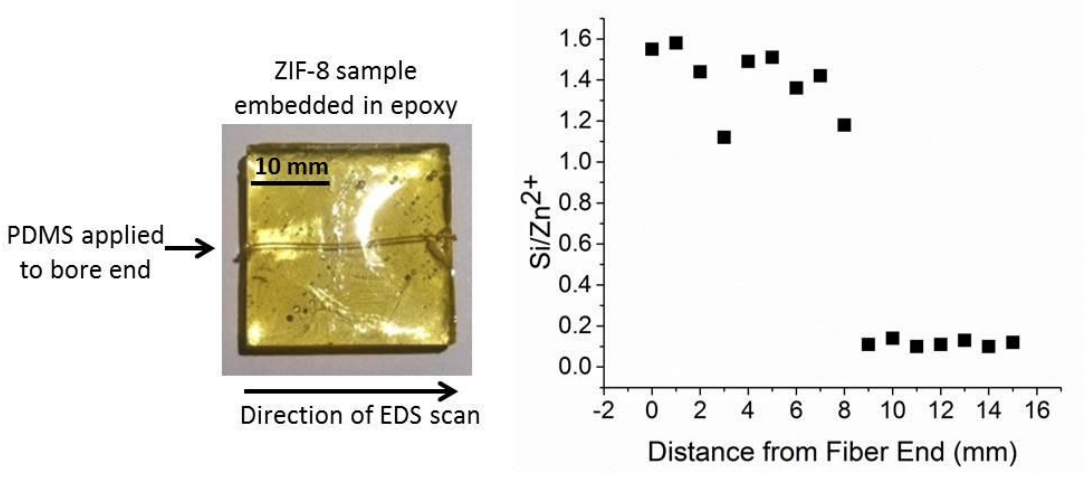


**Figure 46.** PDMS infiltration depth was measured by EDX mapping of ZIF-8 membranes along the fiber length. The sample was prepared by embedding the fiber horizontally in an 1″ x 1″ epoxy block followed by polishing with 1200 grit sandpaper till the axial cross-section of the fiber was exposed. (Left) Photograph of ZIF-8 sample embedded in epoxy. Starting from the point of PDMS application, EDX spectra were collected at 1 mm intervals. (Right) After a distance of 8 mm, the Si signal diminished to noise level.[9]

**Table 12.** Single-component gas permeation data for four gases measured at 25°C from a single-fiber membrane grown under Case 1 conditions.[9]

| Gas | Before Lumen Sealing | | PDMS-Sealed Lumen | |
|---|---|---|---|---|
| | ΔP (Pa) | N (mol .s$^{-1}$) | ΔP (Pa) | N(mol .s$^{-1}$) |
| $C_3H_6$ | 103000 | 4.3E-08 | 103000 | 2.5E-08 |
| $C_3H_8$ | 103000 | 9.5E-09 | 103000 | 2.7E-09 |
| $nC_4H_{10}$ | 103000 | 8.8E-09 | 103000 | 2.3E-09 |
| $iC_4H_{10}$ | 103000 | 8.4E-09 | 103000 | 2.1E-09 |

**Table 13.** Single-component gas permeances at 25°C, with relative contributions of *z*, *d*,

and *b* permeation paths, as calculated from Equations (20) and (21) after fitting to experimental data from Table 12. The permeance of $H_2$ was not included in the model fit, but was predicted from the equations using the fitted parameters and the $H_2$ permeances in ZIF-8 and PDMS. The permeance is always calculated using the total surface area of the as-made membrane, even though a fraction of the membrane area is not available for permeation after lumen sealing due to axial PDMS infiltration.[9]

| **Gas** | **Before Lumen Sealing** | | | | **PDMS-Sealed Lumen** | | | |
|---|---|---|---|---|---|---|---|---|
| | **Permeance (GPU)** | **%z** | **%d** | **%b** | **Permeance (GPU)** | **%z** | **%d** | **%b** |
| $H_2$ | 2542.3 | 98.3 | 0.7 | 1.0 | 1710.8 | 99.4 | 0.6 | 0.0 |
| $C_3H_6$ | 39.8 | 72.1 | 10.5 | 17.4 | 22.9 | 87.3 | 12.7 | 0.1 |
| $C_3H_8$ | 8.8 | 3.1 | 36.5 | 60.4 | 2.5 | 7.7 | 91.7 | 0.6 |
| $nC_4H_{10}$ | 8.1 | 0.1 | 37.6 | 62.3 | 2.1 | 0.4 | 98.6 | 1.0 |
| $iC_4H_{10}$ | 7.7 | 0.0 | 37.7 | 62.3 | 1.9 | 0.0 | 99.0 | 1.0 |

# APPENDIX C

# COPYRIGHT PERMISSION

**Chapter 2.** Adopted with permission from "Eum, K.; Jayachandrababu, K. C.; Rashidi, F.; Zhang, K.; Leisen, J.; Graham, S.; Lively, R. P.; Chance, R. R.; Sholl, D. S.; Jones, C. W.; Nair, S. Highly Tunable Molecular Sieving and Adsorption Properties of Mixed-Linker Zeolitic Imidazolate Frameworks. *Journal of the American Chemical Society* 2015, *137*, 4191-4197." Copyright 2015 American Chemical Society.

**Chapter 3, 4.** Adopted with permission from "Brown, A. J.; Brunelli, N. A.; Eum, K.; Rashidi, F.; Johnson, J. R.; Koros, W. J.; Jones, C. W.; Nair, S. Interfacial microfluidic processing of metal-organic framework hollow fiber membranes. *Science* 2014, *345*, 72-75., *137*, 4191-4197." Copyright 2014 The American Association for the Advancement of Science.

**Chapter 3, 4.** Adopted with permission from "Eum, K.; Rownaghi, A.; Choi, D.; Bhave, R. R.; Jones, C. W.; Nair, S. Fluidic Processing of High-Performance ZIF-8 Membranes on Polymeric Hollow Fibers: Mechanistic Insights and Microstructure Control. *Advanced Functional Materials* 2016, *advance online publication*." Copyright 2014 John Wiley and Sons.

**Figure 1.** Adopted with permission from "Robeson, L. M. The upper bound revisited. *Journal of Membrane Science* 2008, *320*, 390-400" Copyright 2008 Elsevier.

**Figure 2.** Adopted with permission from "Rowsell, J. L. C.; Yaghi, O. M. Metal–organic frameworks: a new class of porous materials. *Microporous and Mesoporous Materials* 2004, *73*, 3-14." Copyright 2004 Elsevier.

**Figure 3.** Adopted with permission from "Phan, A.; Doonan, C. J.; Uribe-Romo, F. J.; Knobler, C. B.; O'Keeffe, M.; Yaghi, O. M. Synthesis, Structure, and Carbon Dioxide Capture Properties of Zeolitic Imidazolate Frameworks. *Accounts of Chemical Research* 2009, *43*, 58-67." Copyright 2010 American Chemical Society.

**Figure 5.** Adopted with permission from "Bachman, J. E.; Smith, Z. P.; Li, T.; Xu, T.; Long, J. R. Enhanced ethylene separation and plasticization resistance in polymer membranes incorporating metal-organic framework nanocrystals. *Nature materials* 2016, *advance online publication*" Copyright 2016 Nature Publishing Group.

**Figure 5.** Adopted with permission from "Cacho-Bailo, F.; Catalán-Aguirre, S.; Etxeberría-Benavides, M.; Karvan, O.; Sebastian, V.; Téllez, C.; Coronas, J. Metal-organic framework membranes on the inner-side of a polymeric hollow fiber by microfluidic synthesis. *Journal of Membrane Science* 2015, *476*, 277-285" Copyright 2015 Elsevier.

**Figure 5.** Adopted with permission from "Hu, Y.; Wei, J.; Liang, Y.; Zhang, H.; Zhang,

X.; Shen, W.; Wang, H. Zeolitic Imidazolate Framework/Graphene Oxide Hybrid Nanosheets as Seeds for the Growth of Ultrathin Molecular Sieving Membranes. *Angew Chem Int Ed Engl* 2016, *55*, 2048-2052." Copyright 2016 Angewandte Chemie Internation Edition.

**Figure 5.** Adopted with permission from "Huang, K.; Li, Q.; Liu, G.; Shen, J.; Guan, K.; Jin, W. A ZIF-71 Hollow Fiber Membrane Fabricated by Contra-Diffusion. *ACS Applied Materials & Interfaces* 2015, *7*, 16157-16160." Copyright 2015 American Chemical Society.

**Figure 5.** Adopted with permission from "Kwon, H. T.; Jeong, H.-K.; Lee, A. S.; An, H. S.; Lee, J. S. Heteroepitaxially Grown Zeolitic Imidazolate Framework Membranes with Unprecedented Propylene/Propane Separation Performances. Journal of the American Chemical Society 2015, 137, 12304-12311." Copyright 2015 American Chemical Society.

**Figure 5.** Adopted with permission from "Mao, Y.; Li, J.; Cao, W.; Ying, Y.; Sun, L.; Peng, X. Pressure-assisted synthesis of HKUST-1 thin film on polymer hollow fiber at room temperature toward gas separation. *ACS Appl Mater Interfaces* 2014, *6*, 4473-4479." Copyright 2014 American Chemical Society.

**Figure 5.** Adopted with permission from "Rodenas, T.; Luz, I.; Prieto, G.; Seoane, B.; Miro, H.; Corma, A.; Kapteijn, F.; Llabres i Xamena, F. X.; Gascon, J. Metal-organic framework nanosheets in polymer composite materials for gas separation. *Nature materials* 2015, *14*, 48-55." Copyright 2014 Nature Publishing Group.

**Figure 5.** Adopted with permission from "Liu, Y.; Pan, J. H.; Wang, N.; Steinbach, F.; Liu, X.; Caro, J. Remarkably enhanced gas separation by partial self-conversion of a laminated membrane to metal-organic frameworks. *Angew Chem Int Ed Engl* 2015, *54*, 3028-3032" Copyright 2015 John Wiley and Sons.

**Figure 5.** Adopted with permission from "Kwon, H. T.; Jeong, H. K. In situ synthesis of thin zeolitic-imidazolate framework ZIF-8 membranes exhibiting exceptionally high propylene/propane separation. *J Am Chem Soc* 2013, *135*, 10763-10768." Copyright 2013 American Chemical Society.

# REFERENCES


(1) Shah, M.; McCarthy, M. C.; Sachdeva, S.; Lee, A. K.; Jeong, H.-K. Current Status of Metal–Organic Framework Membranes for Gas Separations: Promises and Challenges. *Industrial & Engineering Chemistry Research* **2011**, *51*, 2179-2199.

(2) Pan, Y.; Lai, Z. Sharp separation of C2/C3 hydrocarbon mixtures by zeolitic imidazolate framework-8 (ZIF-8) membranes synthesized in aqueous solutions. *Chemical Communications* **2011**, *47*, 10275-10277.

(3) Watanabe, T.; Keskin, S.; Nair, S.; Sholl, D. S. Computational identification of a metal organic framework for high selectivity membrane-based CO2/CH4 separations: Cu(hfipbb)(H2hfipbb)0.5. *Physical Chemistry Chemical Physics* **2009**, *11*, 11389-11394.

(4) Yao, J.; Wang, H. Zeolitic imidazolate framework composite membranes and thin films: synthesis and applications. *Chemical Society Reviews* **2014**, *43*, 4470-4493.

(5) Pimentel, B. R.; Parulkar, A.; Zhou, E.-k.; Brunelli, N. A.; Lively, R. P. Zeolitic Imidazolate Frameworks: Next-Generation Materials for Energy-Efficient Gas Separations. *ChemSusChem* **2014**, *7*, 3202-3240.

(6) Qiu, S.; Xue, M.; Zhu, G. Metal-organic framework membranes: from synthesis to separation application. *Chemical Society Reviews* **2014**, *43*, 6116-6140.

(7) Zhang, Y.; Feng, X.; Yuan, S.; Zhou, J.; Wang, B. Challenges and Recent Advances in MOF-Polymer Composite Membranes for Gas Separation. *Inorganic Chemistry Frontiers* **2016**.

(8) Eldridge, R. B. Olefin/paraffin separation technology: a review. *Industrial & Engineering Chemistry Research* **1993**, *32*, 2208-2212.

(9) Brown, A. J.; Brunelli, N. A.; Eum, K.; Rashidi, F.; Johnson, J. R.; Koros, W. J.; Jones, C. W.; Nair, S. Interfacial microfluidic processing of metal-organic framework hollow fiber membranes. *Science* **2014**, *345*, 72-75.

(10) *Materials for Separation Technologies: Energy and Emission Reduction Opportunities;* BCS, I., Oak Ridge National.: Energy Efficiency and Renewable Energy, 2005.

(11) Ismail, A. F.; Khulbe, K.; Matsuura, T.: *Gas Separation Membranes: Polymeric and Inorganic*; Springer International Publishing, 2015.

(12) Sanders, D. F.; Smith, Z. P.; Guo, R.; Robeson, L. M.; McGrath, J. E.; Paul, D. R.; Freeman, B. D. Energy-efficient polymeric gas separation membranes for a sustainable future: A review. *Polymer* **2013**, *54*, 4729-4761.

(13) McKelvey, S. A.; Clausi, D. T.; Koros, W. J. A guide to establishing hollow fiber macroscopic properties for membrane applications. *Journal of membrane science* **1997**, *124*, 223-232.

(14) Baker, R. W.: *Membrane Technology and Applications*; Wiley, 2004.

(15) Robeson, L. M. The upper bound revisited. *Journal of Membrane Science* **2008**, *320*, 390-400.

(16) Zhou, H.-C.; Long, J. R.; Yaghi, O. M. Introduction to metal–organic frameworks. *Chemical reviews* **2012**, *112*, 673-674.

(17) Denny, M. S., Jr.; Cohen, S. M. In Situ Modification of Metal-Organic Frameworks in Mixed-Matrix Membranes. *Angewandte Chemie-International Edition*

**2015**, *54*, 9029-9032.

(18) Shamsaei, E.; Low, Z.-X.; Lin, X.; Mayahi, A.; Liu, H.; Zhang, X.; Zhe Liu, J.; Wang, H. Rapid synthesis of ultrathin, defect-free ZIF-8 membranes via chemical vapour modification of a polymeric support. *Chemical Communications* **2015**, *51*, 11474-11477.

(19) Shekhah, O.; Liu, J.; Fischer, R. A.; Woll, C. MOF thin films: existing and future applications. *Chemical Society Reviews* **2011**, *40*, 1081-1106.

(20) Bux, H.; Feldhoff, A.; Cravillon, J.; Wiebcke, M.; Li, Y.-S.; Caro, J. Oriented Zeolitic Imidazolate Framework-8 Membrane with Sharp H2/C3H8 Molecular Sieve Separation. *Chemistry of Materials* **2011**, *23*, 2262-2269.

(21) Pan, Y.; Li, T.; Lestari, G.; Lai, Z. Effective separation of propylene/propane binary mixtures by ZIF-8 membranes. *Journal of Membrane Science* **2012**, *390–391*, 93-98.

(22) Eum, K.; Jayachandrababu, K. C.; Rashidi, F.; Zhang, K.; Leisen, J.; Graham, S.; Lively, R. P.; Chance, R. R.; Sholl, D. S.; Jones, C. W.; Nair, S. Highly Tunable Molecular Sieving and Adsorption Properties of Mixed-Linker Zeolitic Imidazolate Frameworks. *Journal of the American Chemical Society* **2015**, *137*, 4191-4197.

(23) Rowsell, J. L. C.; Yaghi, O. M. Metal–organic frameworks: a new class of porous materials. *Microporous and Mesoporous Materials* **2004**, *73*, 3-14.

(24) Phan, A.; Doonan, C. J.; Uribe-Romo, F. J.; Knobler, C. B.; O'Keeffe, M.; Yaghi, O. M. Synthesis, Structure, and Carbon Dioxide Capture Properties of Zeolitic Imidazolate Frameworks. *Accounts of Chemical Research* **2009**, *43*, 58-67.

(25) Venna, S. R.; Carreon, M. A. Metal organic framework membranes for carbon dioxide separation. *Chemical Engineering Science* **2015**, *124*, 3-19.

(26) Huang, A.; Dou, W.; Caro, J. Steam-Stable Zeolitic Imidazolate Framework ZIF-90 Membrane with Hydrogen Selectivity through Covalent Functionalization. *Journal of the American Chemical Society* **2010**, *132*, 15562-15564.

(27) Zhang, W.; Liu, Y.; Lu, G.; Wang, Y.; Li, S.; Cui, C.; Wu, J.; Xu, Z.; Tian, D.; Huang, W.; DuCheneu, J. S.; Wei, W. D.; Chen, H.; Yang, Y.; Huo, F. Mesoporous Metal–Organic Frameworks with Size-, Shape-, and Space-Distribution-Controlled Pore Structure. *Advanced Materials* **2015**, *27*, 2923-2929.

(28) Ben, T.; Lu, C.; Pei, C.; Xu, S.; Qiu, S. Polymer-Supported and Free-Standing Metal–Organic Framework Membrane. *Chemistry – A European Journal* **2012**, *18*, 10250-10253.

(29) Shah, M.; Kwon, H. T.; Tran, V.; Sachdeva, S.; Jeong, H.-K. One step in situ synthesis of supported zeolitic imidazolate framework ZIF-8 membranes: Role of sodium formate. *Microporous and Mesoporous Materials* **2013**, *165*, 63-69.

(30) Khaletskaya, K.; Turner, S.; Tu, M.; Wannapaiboon, S.; Schneemann, A.; Meyer, R.; Ludwig, A.; Van Tendeloo, G.; Fischer, R. A. Self-Directed Localization of ZIF-8 Thin Film Formation by Conversion of ZnO Nanolayers. *Advanced Functional Materials* **2014**, *24*, 4804-4811.

(31) Mao, Y.; Li, J.; Cao, W.; Ying, Y.; Sun, L.; Peng, X. Pressure-assisted synthesis of HKUST-1 thin film on polymer hollow fiber at room temperature toward gas separation. *ACS Appl Mater Interfaces* **2014**, *6*, 4473-4479.

(32) Li, W.; Yang, Z.; Zhang, G.; Fan, Z.; Meng, Q.; Shen, C.; Gao, C. Stiff

metal-organic framework-polyacrylonitrile hollow fiber composite membranes with high gas permeability. *Journal of Materials Chemistry A* **2014**, *2*, 2110-2118.

(33) Snyder, M. A.; Tsapatsis, M. Hierarchical Nanomanufacturing: From Shaped Zeolite Nanoparticles to High-Performance Separation Membranes. *Angewandte Chemie International Edition* **2007**, *46*, 7560-7573.

(34) Brown, A. J.; Johnson, J. R.; Lydon, M. E.; Koros, W. J.; Jones, C. W.; Nair, S. Continuous polycrystalline zeolitic imidazolate framework-90 membranes on polymeric hollow fibers. *Angew Chem Int Ed Engl* **2012**, *51*, 10615-10618.

(35) Peng, Y.; Li, Y.; Ban, Y.; Jin, H.; Jiao, W.; Liu, X.; Yang, W. Metal-organic framework nanosheets as building blocks for molecular sieving membranes. *Science* **2014**, *346*, 1356-1359.

(36) Hu, Y.; Wei, J.; Liang, Y.; Zhang, H.; Zhang, X.; Shen, W.; Wang, H. Zeolitic Imidazolate Framework/Graphene Oxide Hybrid Nanosheets as Seeds for the Growth of Ultrathin Molecular Sieving Membranes. *Angew Chem Int Ed Engl* **2016**, *55*, 2048-2052.

(37) Kwon, H. T.; Jeong, H.-K.; Lee, A. S.; An, H. S.; Lee, J. S. Heteroepitaxially Grown Zeolitic Imidazolate Framework Membranes with Unprecedented Propylene/Propane Separation Performances. *Journal of the American Chemical Society* **2015**, *137*, 12304-12311.

(38) Dong, X.; Huang, K.; Liu, S.; Ren, R.; Jin, W.; Lin, Y. S. Synthesis of zeolitic imidazolate framework-78 molecular-sieve membrane: defect formation and elimination. *Journal of Materials Chemistry* **2012**, *22*, 19222-19227.

(39) Li, L.; Yao, J.; Chen, R.; He, L.; Wang, K.; Wang, H. Infiltration of precursors into a porous alumina support for ZIF-8 membrane synthesis. *Microporous and Mesoporous Materials* **2013**, *168*, 15-18.

(40) Cacho-Bailo, F.; Catalán-Aguirre, S.; Etxeberría-Benavides, M.; Karvan, O.; Sebastian, V.; Téllez, C.; Coronas, J. Metal-organic framework membranes on the inner-side of a polymeric hollow fiber by microfluidic synthesis. *Journal of Membrane Science* **2015**, *476*, 277-285.

(41) Cacho-Bailo, F.; Caro, G.; Etxeberria-Benavides, M.; Karvan, O.; Tellez, C.; Coronas, J. High selectivity ZIF-93 hollow fiber membranes for gas separation. *Chemical Communications* **2015**, *51*, 11283-11285.

(42) Huang, K.; Li, Q.; Liu, G.; Shen, J.; Guan, K.; Jin, W. A ZIF-71 Hollow Fiber Membrane Fabricated by Contra-Diffusion. *ACS Applied Materials & Interfaces* **2015**, *7*, 16157-16160.

(43) Ameloot, R.; Vermoortele, F.; Vanhove, W.; Roeffaers, M. B. J.; Sels, B. F.; De Vos, D. E. Interfacial synthesis of hollow metal–organic framework capsules demonstrating selective permeability. *Nat Chem* **2011**, *3*, 382-387.

(44) Kwon, H. T.; Jeong, H. K. In situ synthesis of thin zeolitic-imidazolate framework ZIF-8 membranes exhibiting exceptionally high propylene/propane separation. *J Am Chem Soc* **2013**, *135*, 10763-10768.

(45) Campbell, J.; Davies, R. P.; Braddock, D. C.; Livingston, A. G. Improving the permeance of hybrid polymer/metal-organic framework (MOF) membranes for organic solvent nanofiltration (OSN) - development of MOF thin films via interfacial synthesis. *Journal of Materials Chemistry A* **2015**, *3*, 9668-9674.

(46) Eum, K.; Rownaghi, A.; Choi, D.; Bhave, R. R.; Jones, C. W.; Nair, S.

Fluidic Processing of High-Performance ZIF-8 Membranes on Polymeric Hollow Fibers: Mechanistic Insights and Microstructure Control. *Advanced Functional Materials* **2016**, *advance online publication*

(47) Bachman, J. E.; Smith, Z. P.; Li, T.; Xu, T.; Long, J. R. Enhanced ethylene separation and plasticization resistance in polymer membranes incorporating metal-organic framework nanocrystals. *Nature materials* **2016**, *advance online publication*.

(48) Liu, Y.; Pan, J. H.; Wang, N.; Steinbach, F.; Liu, X.; Caro, J. Remarkably enhanced gas separation by partial self-conversion of a laminated membrane to metal-organic frameworks. *Angew Chem Int Ed Engl* **2015**, *54*, 3028-3032.

(49) Rodenas, T.; Luz, I.; Prieto, G.; Seoane, B.; Miro, H.; Corma, A.; Kapteijn, F.; Llabres i Xamena, F. X.; Gascon, J. Metal-organic framework nanosheets in polymer composite materials for gas separation. *Nature materials* **2015**, *14*, 48-55.

(50) Zhang, C.; Koros, W. J. Zeolitic Imidazolate Framework-Enabled Membranes: Challenges and Opportunities. *The Journal of Physical Chemistry Letters* **2015**, *6*, 3841-3849.

(51) Zhang, Z.; Yao, Z.-Z.; Xiang, S.; Chen, B. Perspective of microporous metal–organic frameworks for CO2capture and separation. *Energy & Environmental Science* **2014**, *7*, 2868.

(52) Dong, G.; Li, H.; Chen, V. Challenges and opportunities for mixed-matrix membranes for gas separation. *Journal of Materials Chemistry A* **2013**, *1*, 4610-4630.

(53) Zhang, C.; Dai, Y.; Johnson, J. R.; Karvan, O.; Koros, W. J. High performance ZIF-8/6FDA-DAM mixed matrix membrane for propylene/propane separations. *Journal of Membrane Science* **2012**, *389*, 34-42.

(54) Song, Q.; Nataraj, S. K.; Roussenova, M. V.; Tan, J. C.; Hughes, D. J.; Li, W.; Bourgoin, P.; Alam, M. A.; Cheetham, A. K.; Al-Muhtaseb, S. A.; Sivaniah, E. Zeolitic imidazolate framework (ZIF-8) based polymer nanocomposite membranes for gas separation. *Energy & Environmental Science* **2012**, *5*, 8359-8369.

(55) Sánchez-Laínez, J.; Zornoza, B.; Mayoral, Á.; Berenguer-Murcia, Á.; Cazorla-Amorós, D.; Téllez, C.; Coronas, J. Beyond the H2/CO2upper bound: one-step crystallization and separation of nano-sized ZIF-11 by centrifugation and its application in mixed matrix membranes. *J. Mater. Chem. A* **2015**, *3*, 6549-6556.

(56) Zhang, R.; Ji, S.; Wang, N.; Wang, L.; Zhang, G.; Li, J. R. Coordination-driven in situ self-assembly strategy for the preparation of metal-organic framework hybrid membranes. *Angew Chem Int Ed Engl* **2014**, *53*, 9775-9779.

(57) Chng, M. L.; Xiao, Y.; Chung, T.-S.; Toriida, M.; Tamai, S. Enhanced propylene/propane separation by carbonaceous membrane derived from poly (aryl ether ketone)/2,6-bis(4-azidobenzylidene)-4-methyl-cyclohexanone interpenetrating network. *Carbon* **2009**, *47*, 1857-1866.

(58) Okamoto, K.-i.; Kawamura, S.; Yoshino, M.; Kita, H.; Hirayama, Y.; Tanihara, N.; Kusuki, Y. Olefin/Paraffin Separation through Carbonized Membranes Derived from an Asymmetric Polyimide Hollow Fiber Membrane. *Industrial & Engineering Chemistry Research* **1999**, *38*, 4424-4432.

(59) Hayashi, J.-i.; Mizuta, H.; Yamamoto, M.; Kusakabe, K.; Morooka, S.; Suh, S.-H. Separation of Ethane/Ethylene and Propane/Propylene Systems with a

Carbonized BPDA−pp‘ODA Polyimide Membrane. *Industrial & Engineering Chemistry Research* **1996**, *35*, 4176-4181.

(60) Giannakopoulos, I. G.; Nikolakis, V. Separation of Propylene/Propane Mixtures Using Faujasite-Type Zeolite Membranes. *Industrial & Engineering Chemistry Research* **2005**, *44*, 226-230.

(61) Burns, R. L.; Koros, W. J. Defining the challenges for C3H6/C3H8 separation using polymeric membranes. *Journal of Membrane Science* **2003**, *211*, 299-309.

(62) Kwon, H. T.; Jeong, H.-K. Highly propylene-selective supported zeolite-imidazolate framework (ZIF-8) membranes synthesized by rapid microwave-assisted seeding and secondary growth. *Chemical Communications* **2013**, *49*, 3854-3856.

(63) Liu, D.; Ma, X.; Xi, H.; Lin, Y. S. Gas transport properties and propylene/propane separation characteristics of ZIF-8 membranes. *Journal of Membrane Science* **2014**, *451*, 85-93.

(64) Hara, N.; Yoshimune, M.; Negishi, H.; Haraya, K.; Hara, S.; Yamaguchi, T. Diffusive separation of propylene/propane with ZIF-8 membranes. *Journal of Membrane Science* **2014**, *450*, 215-223.

(65) Pan, Y.; Liu, W.; Zhao, Y.; Wang, C.; Lai, Z. Improved ZIF-8 membrane: Effect of activation procedure and determination of diffusivities of light hydrocarbons. *Journal of Membrane Science* **2015**, *493*, 88-96.

(66) Kwon, H. T.; Jeong, H.-K. Improving propylene/propane separation performance of Zeolitic-Imidazolate framework ZIF-8 Membranes. *Chemical Engineering Science* **2015**, *124*, 20-26.

(67) Yu, J.; Pan, Y.; Wang, C.; Lai, Z. ZIF-8 membranes with improved reproducibility fabricated from sputter-coated ZnO/alumina supports. *Chemical Engineering Science* **2016**, *141*, 119-124.

(68) Eum, K.; Ma, C.; Rownagh, A.; Jones, C. W.; Nair, S. ZIF-8 Membranes via Interfacial Microfluidic Processing in Poly-meric Hollow Fibers: Efficient Propylene Separation at Elevated Pressures *Applied Materials & Interfaces* **2016**, *Submitted*.

(69) Cussler, E. L.: *Diffusion: Mass Transfer in Fluid Systems*; Cambridge University Press, 1997.

(70) Rousseau, R. W.: *Handbook of separation process technology*; J. Wiley, 1987.

(71) Krishna, R.; Baur, R. Modelling issues in zeolite based separation processes. *Separation and Purification Technology* **2003**, *33*, 213-254.

(72) Skoulidas, A. I.; Sholl, D. S. Transport Diffusivities of CH4, CF4, He, Ne, Ar, Xe, and SF6 in Silicalite from Atomistic Simulations. *The Journal of Physical Chemistry B* **2002**, *106*, 5058-5067.

(73) Thompson, J. A. EVALUATION AND APPLICATION OF NEW NANOPOROUS MATERIALS FOR ACID GAS SEPARATIONS. Dissertation, Georgia Institute of Technology, 2013.

(74) Crank, J.: *The mathematics of diffusion*; Oxford University Press Inc., 1975.

(75) Ruthven, D. M.; Loughlin, K. F. The effect of crystallite shape and size distribution on diffusion measurements in molecular sieves. *Chemical Engineering Science* **1971**, *26*, 577-584.

(76) Kärger, J.; Ruthven, D. M.: *Diffusion in zeolites and other microporous solids*; Wiley, 1992.

(77) Farha, O. K.; Özgür Yazaydın, A.; Eryazici, I.; Malliakas, C. D.; Hauser, B. G.; Kanatzidis, M. G.; Nguyen, S. T.; Snurr, R. Q.; Hupp, J. T. De novo synthesis of a metal–organic framework material featuring ultrahigh surface area and gas storage capacities. *Nat Chem* **2010**, *2*, 944-948.

(78) Demessence, A.; D'Alessandro, D. M.; Foo, M. L.; Long, J. R. Strong CO2 Binding in a Water-Stable, Triazolate-Bridged Metal−Organic Framework Functionalized with Ethylenediamine. *Journal of the American Chemical Society* **2009**, *131*, 8784-8786.

(79) Cohen, S. M. Postsynthetic Methods for the Functionalization of Metal–Organic Frameworks. *Chemical Reviews* **2011**, *112*, 970-1000.

(80) Pan, L.; Olson, D. H.; Ciemnolonski, L. R.; Heddy, R.; Li, J. Separation of Hydrocarbons with a Microporous Metal–Organic Framework. *Angewandte Chemie* **2006**, *118*, 632-635.

(81) Getman, R. B.; Bae, Y.-S.; Wilmer, C. E.; Snurr, R. Q. Review and analysis of molecular simulations of methane, hydrogen, and acetylene storage in metal–organic frameworks. *Chemical reviews* **2011**, *112*, 703-723.

(82) Pan, Y.; Lai, Z. Sharp separation of C2/C3 hydrocarbon mixtures by zeolitic imidazolate framework-8 (ZIF-8) membranes synthesized in aqueous solutions. *Chemical Communications* **2011**, *47*, 10275-10277.

(83) Phan, A.; Doonan, C. J.; Uribe-Romo, F. J.; Knobler, C. B.; O'Keeffe, M.; Yaghi, O. M. Synthesis, Structure, and Carbon Dioxide Capture Properties of Zeolitic Imidazolate Frameworks. *Accounts of Chemical Research* **2009**, *43*, 58-67.

(84) Banerjee, R.; Phan, A.; Wang, B.; Knobler, C. B.; Furukawa, H.; O'Keeffe, M.; Yaghi, O. M. High-Throughput Synthesis of Zeolitic Imidazolate Frameworks and Application to $CO_2$ Capture. *Science* **2008**, *319*, 939-943.

(85) Park, K. S.; Ni, Z.; Côté, A. P.; Choi, J. Y.; Huang, R.; Uribe-Romo, F. J.; Chae, H. K.; O'Keeffe, M.; Yaghi, O. M. Exceptional chemical and thermal stability of zeolitic imidazolate frameworks. *Proceedings of the National Academy of Sciences* **2006**, *103*, 10186-10191.

(86) Li, J.-R.; Kuppler, R. J.; Zhou, H.-C. Selective gas adsorption and separation in metal-organic frameworks. *Chemical Society Reviews* **2009**, *38*, 1477-1504.

(87) Li, J.-R.; Ma, Y.; McCarthy, M. C.; Sculley, J.; Yu, J.; Jeong, H.-K.; Balbuena, P. B.; Zhou, H.-C. Carbon dioxide capture-related gas adsorption and separation in metal-organic frameworks. *Coordination Chemistry Reviews* **2011**, *255*, 1791-1823.

(88) Thompson, J. A.; Blad, C. R.; Brunelli, N. A.; Lydon, M. E.; Lively, R. P.; Jones, C. W.; Nair, S. Hybrid Zeolitic Imidazolate Frameworks: Controlling Framework Porosity and Functionality by Mixed-Linker Synthesis. *Chemistry of Materials* **2012**, *24*, 1930-1936.

(89) Krishna, R. Diffusion in porous crystalline materials. *Chemical Society Reviews* **2012**, *41*, 3099-3118.

(90) Zhang, K.; Lively, R. P.; Zhang, C.; Chance, R. R.; Koros, W. J.; Sholl, D. S.; Nair, S. Exploring the Framework Hydrophobicity and Flexibility of ZIF-8: From Biofuel Recovery to Hydrocarbon Separations. *The Journal of Physical Chemistry*

*Letters* **2013**, *4*, 3618-3622.

(91) Zhang, C.; Lively, R. P.; Zhang, K.; Johnson, J. R.; Karvan, O.; Koros, W. J. Unexpected Molecular Sieving Properties of Zeolitic Imidazolate Framework-8. *Journal of Physical Chemistry Letters* **2012**, *3*, 2130-2134.

(92) Gee, J. A.; Chung, J.; Nair, S.; Sholl, D. S. Adsorption and Diffusion of Small Alcohols in Zeolitic Imidazolate Frameworks ZIF-8 and ZIF-90. *Journal of Physical Chemistry C* **2013**, *117*, 3169-3176.

(93) Zhang, K.; Lively, R. P.; Zhang, C.; Chance, R. R.; Koros, W. J.; Sholl, D. S.; Nair, S. Exploring the Framework Hydrophobicity and Flexibility of ZIF-8: From Biofuel Recovery to Hydrocarbon Separations. *Journal of Physical Chemistry Letters* **2013**.

(94) Zhang, K.; Lively, R. P.; Dose, M. E.; Brown, A. J.; Zhang, C.; Chung, J.; Nair, S.; Koros, W. J.; Chance, R. R. Alcohol and water adsorption in zeolitic imidazolate frameworks. *Chemical Communications* **2013**, *49*, 3245.

(95) Zhang, K.; Lively, R. P.; Zhang, C.; Koros, W. J.; Chance, R. R. Investigating the Intrinsic Ethanol/Water Separation Capability of ZIF-8: An Adsorption and Diffusion Study. *Journal of Physical Chemistry C* **2013**, *117*, 7214-7225.

(96) Thompson, J. A.; Brunelli, N. A.; Lively, R. P.; Johnson, J. R.; Jones, C. W.; Nair, S. Tunable CO2 Adsorbents by Mixed-Linker Synthesis and Postsynthetic Modification of Zeolitic Imidazolate Frameworks. *The Journal of Physical Chemistry C* **2013**, *117*, 8198-8207.

(97) Cravillon, J.; Schroder, C. A.; Bux, H.; Rothkirch, A.; Caro, J.; Wiebcke, M. Formate modulated solvothermal synthesis of ZIF-8 investigated using time-resolved in situ X-ray diffraction and scanning electron microscopy. *CrystEngComm* **2012**, *14*, 492-498.

(98) Zimmerman, C. M.; Singh, A.; Koros, W. J. Diffusion in gas separation membrane materials: A comparison and analysis of experimental characterization techniques. *Journal of Polymer Science Part B: Polymer Physics* **1998**, *36*, 1747-1755.

(99) Karger, J.; Ruthven, D. M.; Theodorou, D. N.: Diffusion in Nanoporous Materials. In *Diffusion in Nanoporous Materials*; 1 ed.; Wiley, 2012; Vol. 1.

(100) Cravillon, J.; Münzer, S.; Lohmeier, S.-J.; Feldhoff, A.; Huber, K.; Wiebcke, M. Rapid Room-Temperature Synthesis and Characterization of Nanocrystals of a Prototypical Zeolitic Imidazolate Framework. *Chemistry of Materials* **2009**, *21*, 1410-1412.

(101) Kong, X.; Deng, H.; Yan, F.; Kim, J.; Swisher, J. A.; Smith, B.; Yaghi, O. M.; Reimer, J. A. Mapping of Functional Groups in Metal-Organic Frameworks. *Science* **2013**, *341*, 882-885.

(102) Yang, D.; Currier, R. P.; Le, L. A.; Welch, C. F.; Tornga, S. C.; Martinez, R.; Morrison, M. *Enhanced Separation Efficiency in Olefin/Paraffin Distillation*2013.

(103) Li, J.-R.; Sculley, J.; Zhou, H.-C. Metal–organic frameworks for separations. *Chemical reviews* **2011**, *112*, 869-932.

(104) Qiu, S.; Xue, M.; Zhu, G. Metal-organic framework membranes: from synthesis to separation application. *Chemical Society Reviews* **2014**.

(105) Robeson, L. M. Correlation of separation factor versus permeability for polymeric membranes. *Journal of Membrane Science* **1991**, *62*, 165-185.

(106) Wang, X.; Xie, L.; Huang, K.-W.; Lai, Z. A rationally designed amino-

borane complex in a metal organic framework: a novel reusable hydrogen storage and size-selective reduction material. *Chemical Communications* **2015**, *51*, 7610-7613.

(107) Al-Maythalony, B. A.; Shekhah, O.; Swaidan, R.; Belmabkhout, Y.; Pinnau, I.; Eddaoudi, M. Quest for Anionic MOF Membranes: Continuous sod-ZMOF Membrane with CO2 Adsorption-Driven Selectivity. *Journal of the American Chemical Society* **2015**, *137*, 1754-1757.

(108) Li, Y.-S.; Bux, H.; Feldhoff, A.; Li, G.-L.; Yang, W.-S.; Caro, J. Controllable Synthesis of Metal–Organic Frameworks: From MOF Nanorods to Oriented MOF Membranes. *Advanced Materials* **2010**, *22*, 3322-3326.

(109) Chafin, R.; Lee, J. S.; Koros, W. J. Effects of casting and post casting annealing on xylene isomer transport properties of Torlon® 4000T films. *Polymer* **2010**, *51*, 3462-3471.

(110) Baker, R. W.: *Membrane Technology and Applications*; Wiley, 2012.

(111) Pan, Y.; Wang, B.; Lai, Z. Synthesis of ceramic hollow fiber supported zeolitic imidazolate framework-8 (ZIF-8) membranes with high hydrogen permeability. *Journal of Membrane Science* **2012**, *421–422*, 292-298.

(112) Zhang, X.; Liu, Y.; Kong, L.; Liu, H.; Qiu, J.; Han, W.; Weng, L.-T.; Yeung, K. L.; Zhu, W. A simple and scalable method for preparing low-defect ZIF-8 tubular membranes. *Journal of Materials Chemistry A* **2013**, *1*, 10635-10638.

(113) Lively, R. P.; Mysona, J. A.; Chance, R. R.; Koros, W. J. Formation of Defect-Free Latex Films on Porous Fiber Supports. *ACS Applied Materials & Interfaces* **2011**, *3*, 3568-3582.

(114) Rownaghi, A. A.; Rezaei, F.; Labreche, Y.; Brennan, P. J.; Johnson, J. R.; Li, F. S.; Koros, W. J. In situ Formation of a Monodispersed Spherical Mesoporous Nanosilica–Torlon Hollow-Fiber Composite for Carbon Dioxide Capture. *ChemSusChem* **2015**, *8*, 3439-3450.

(115) Sankar Nair, Andrew J. Brown, Nicholas A. Brunelli, Christopher W. Jones. Flow Professing and characterization of metal-organic framework (MOF) membranes in hollow fiber and tubular modules. US Patent US 20140336435A1, 11/13/2014.

(116) Gummalla, M.; Tsapatsis, M.; Watkins, J. J.; Vlachos, D. G. Multiscale hybrid modeling of film deposition within porous substrates. *AIChE Journal* **2004**, *50*, 684-695.

(117) Khare, H. S.; Burris, D. L. A quantitative method for measuring nanocomposite dispersion. *Polymer* **2010**, *51*, 719-729.

(118) Rasband, W. S.: *"ImageJ"*; U.S. National Institutes of Health, Bethesda Maryland, USA

(119) Korelskiy, D.; Grahn, M.; Mouzon, J.; Hedlund, J. Characterization of flow-through micropores in MFI membranes by permporometry. *Journal of Membrane Science* **2012**, *417–418*, 183-192.

(120) Calvo, J. I.; Hernández, A.; Prádanos, P.; Martınez, L.; Bowen, W. R. Pore Size Distributions in Microporous Membranes II. Bulk Characterization of Track-Etched Filters by Air Porometry and Mercury Porosimetry. *Journal of Colloid and Interface Science* **1995**, *176*, 467-478.

(121) Zhang, C.; Lively, R. P.; Zhang, K.; Johnson, J. R.; Karvan, O.; Koros, W. J. Unexpected Molecular Sieving Properties of Zeolitic Imidazolate Framework-8. *J Phys*

*Chem Lett* **2012**, *3*, 2130-2134.

(122) Huang, A.; Liu, Q.; Wang, N.; Zhu, Y.; Caro, J. Bicontinuous Zeolitic Imidazolate Framework ZIF-8@GO Membrane with Enhanced Hydrogen Selectivity. *Journal of the American Chemical Society* **2014**, *136*, 14686-14689.

(123) Duan, J.; Pan, Y.; Pacheco, F.; Litwiller, E.; Lai, Z.; Pinnau, I. High-performance polyamide thin-film-nanocomposite reverse osmosis membranes containing hydrophobic zeolitic imidazolate framework-8. *Journal of Membrane Science* **2015**, *476*, 303-310.

(124) Kong, L.; Zhang, X.; Liu, H.; Qiu, J. Synthesis of a highly stable ZIF-8 membrane on a macroporous ceramic tube by manual-rubbing ZnO deposition as a multifunctional layer. *Journal of Membrane Science* **2015**, *490*, 354-363.

(125) Huang, A.; Bux, H.; Steinbach, F.; Caro, J. Molecular-Sieve Membrane with Hydrogen Permselectivity: ZIF-22 in LTA Topology Prepared with 3-Aminopropyltriethoxysilane as Covalent Linker. *Angewandte Chemie* **2010**, *122*, 5078-5081.

(126) Hwang, J. R.; Sefton, M. V. The effects of polymer concentration and a pore-forming agent (PVP) on HEMA-MMA microcapsule structure and permeability. *Journal of Membrane Science* **1995**, *108*, 257-268.

(127) Rangnekar, N.; Mittal, N.; Elyassi, B.; Caro, J.; Tsapatsis, M. Zeolite membranes - a review and comparison with MOFs. *Chemical Society Reviews* **2015**, *44*, 7128-7154.

(128) Chmelik, C. Characteristic features of molecular transport in MOF ZIF-8 as revealed by IR microimaging. *Microporous and Mesoporous Materials* **2015**, *216*, 138-145.

(129) Aceituno Melgar, V. M.; Kwon, H. T.; Kim, J. Direct spraying approach for synthesis of ZIF-7 membranes by electrospray deposition. *Journal of Membrane Science* **2014**, *459*, 190-196.

(130) Gebel, G. Structural evolution of water swollen perfluorosulfonated ionomers from dry membrane to solution. *Polymer* **2000**, *41*, 5829-5838.

(131) Izák, P.; Hovorka, Š.; Bartovský, T.; Bartovská, L.; Crespo, J. G. Swelling of polymeric membranes in room temperature ionic liquids. *Journal of Membrane Science* **2007**, *296*, 131-138.

(132) Rashidi, F.; Blad, C. R.; Jones, C. W.; Nair, S. Synthesis, characterization, and tunable adsorption and diffusion properties of hybrid ZIF-7-90 frameworks. *AIChE Journal* **2016**, *62*, 525-537.

(133) Zhao, P.; Lampronti, G. I.; Lloyd, G. O.; Wharmby, M. T.; Facq, S.; Cheetham, A. K.; Redfern, S. A. T. Phase Transitions in Zeolitic Imidazolate Framework 7: The Importance of Framework Flexibility and Guest-Induced Instability. *Chemistry of Materials* **2014**, *26*, 1767-1769.

(134) Koh, D.-Y.; McCool, B. A.; Deckman, H. W.; Lively, R. P. Sub-Angstrom Molecular Differentiation of Organic Liquid by Carbon Molecular Sieve Membranes. *In Revision*.

(135) Koller, H. Diffusion in Nanoporous Materials. By Jörg Kärger, Douglas M. Ruthven and Doros N. Theodorou. *Angewandte Chemie International Edition* **2012**, *51*, 11939-11940.

(136) Choi, J.; Jeong, H.-K.; Snyder, M. A.; Stoeger, J. A.; Masel, R. I.;

Tsapatsis, M. Grain Boundary Defect Elimination in a Zeolite Membrane by Rapid Thermal Processing. *Science* **2009**, *325*, 590-593.

(137) Husain, S. Mixed matrix dual layer hollow fiber membranes for natural gas separation. Georgia Institute of Technology, 2006.

(138) Pinnau, I.; He, Z. Pure- and mixed-gas permeation properties of polydimethylsiloxane for hydrocarbon/methane and hydrocarbon/hydrogen separation. *Journal of Membrane Science* **2004**, *244*, 227-233.

(139) Shi, Y.; Burns, C. M.; Feng, X. Poly(dimethyl siloxane) thin film composite membranes for propylene separation from nitrogen. *Journal of Membrane Science* **2006**, *282*, 115-123.

# VITA

**Kiwon Eum**

Kiwon Eum was born in Seoul, South Korea. He attended private schools in Seoul, South Korea, received a B.A. in Chemical & Biological Engineering from Korea University in 2009. M.S was also received from same school before coming to Georgia Tech to pursue a doctorate in Chemical & Biomolecular Engineering. When he is not working on his research, Kiwon Eum enjoys traveling with his wife, Lina.